The essential problem of radar-estimated refractivity – quantifying its biases and errors

Ya-Chien Feng

Department of Atmospheric and Oceanic Sciences
McGill University
Montreal, Quebec, Canada
August 2017

A thesis submitted to McGill University in partial fulfillment of the requirements for the degree of Doctor of Philosophy

Abstract

Refractivity fields estimated from weather radars provide high resolution information on near-surface thermodynamic conditions that are critical for understanding and forecasting storms. However, quantitative applications of the radar-estimated refractivity fields, such as data assimilation and operational radar network implementation, have been hindered by the lack of quantitative knowledge of data quality. This thesis addresses the essential challenge of the refractivity estimation, namely the problem of the noisy phase measurements of ground targets, by understanding and quantifying their causes and resulting effect on refractivity estimation.

The uncertainties of refractivity introduced by a variety of processes causing changes in the measured phase of ground targets were examined: biases associated with the combination of the changes in vertical gradient of refractivity and the height differences between targets and the radar; biases related to the antenna phase pattern; and other uncertainties in the processing algorithm. For each, methods were proposed to either correct the biases, such as by deriving the vertical gradient of refractivity using returned power from multiple elevation angles, or to estimate the random errors, such as by using information in polarization and elevation. It is shown that once biases are corrected, random errors in derived refractivity are smaller than 1 N-unit in regions of good ground target coverage. The acquired knowledge on the fundamental data quality problems of radar-estimated refractivity will set the stage for future quantitative applications and improvements to the original technique.

Résumé

Les champs de réfractivité estimés à partir des radars météorologiques fournissent de l'information à haute résolution sur les conditions thermodynamiques près de la surface, information qui est essentielle pour comprendre et prévoir les orages. Cependant, l'utilisation de ces champs de réfractivité dans des applications quantitatives, tels que l'assimilation des données et l'utilisation en milieu opérationnel, est entravée par le manque de connaissances quantitatives sur la qualité des données. Cette thèse s'attaque au défi majeur de l'estimation de la réfractivité : le problème des bruits de mesures des phases des cibles terrestres. On adresse ce problème en tentant de comprendre et caractériser les causes de ces bruits de mesures et l'effet qu'ils ont sur l'estimation de la réfractivité.

Les incertitudes des mesures de réfractivité introduites par des différents processus causant des bruits de mesure dans la phase des cibles terrestres ont été examinées : les biais associés aux changements du gradient vertical de la réfractivité combinés avec les différences d'hauteur entre les cibles terrestre et le radar ; les biais liés au motif de phase de l'antenne ; et d'autres incertitudes de l'algorithme de traitement. Pour chaque type d'incertitude, des méthodes ont été proposées soit pour corriger les biais, par exemple en dérivant le gradient vertical de la réfractivité en utilisant la puissance captée à plusieurs angles d'élévation, soit pour estimer les erreurs aléatoires, par exemple en utilisant des informations sur la polarisation et l'élévation. Les résultats démontrent qu'une fois les biais corrigés, les erreurs aléatoires des mesures de réfractivité dérivées sont inférieures à 1 N-unité dans les régions avec une bonne couverture d'écho au sol. Les connaissances acquises durant cette thèse sur le problème fondamental de la qualité des données de réfractivité estimée par le radar serviront comme point de départ pour des futures appli-

cations quantitatives et pour l'amélioration de la technique initiale.

Contributions of Authors

Chapters 2 and 3 are in the form of published articles, and Chapter 4 is in preparation for submission to the Journal of Atmospheric and Oceanic Technology. I developed the methods, performed the analysis and wrote the manuscripts. Prof. Frédéric Fabry provided supervision of the works and edited the manuscripts. In Chapter 2, Dr. Tammy M. Weckwerth collected the NCAR S-POL radar data and revised the manuscript.

Statement of Originality

- The data quality issues of the radar-estimated refractivity are quantified in two fronts.

  - The refractivity bias associated with the changes in the vertical gradient of refractivity coupled with the height difference between the ground targets and the radar is analytically estimated. Based on the analysis, a new method is proposed to correct this bias and obtain an accurate two-dimensional refractivity field at a given height above the terrain. The height representativeness of the data is thus clarified.

  - The errors of refractivity resulting from the uncertainties of the phase measurements and the data processing are quantitatively estimated.

- A novel method is developed to estimate the near surface refractivity profile by using the power returned of ground targets at multiple elevations. This method shows promising result when compared with in-situ observations.

- The random uncertainty of phase measurements is quantitatively characterized by newly defined correlations of time series of phase between successive elevations or between polarizations. This correlation also provides a robust way to select ground target in the data processing of radar-estimated refractivity method.

- The phase pattern of parabolic antenna is presented for the first time to the radar meteorology community. Its impacts on the radar data quality, such as wind measurements, ground target mitigation, and refractivity estimations, are explored.

Acknowledgements

I would like to express my sincere gratitude to my supervisor, Prof. Frédéric Fabry, for his genuine enlightenment of the scientific thinking. Particularly, he once told me, "*If you don't dream, you don't do science.*" I appreciate very much his open-minded and abundant patience that let my naive questions flow during discussions and have lots of fun in those dreams. I also thank Prof. Isztar Zawadzki for his intuitive fundamental scientific challenges and honest critical comments, that made me grow a lot.

Many thanks go to the J.S. Marshall Radar Observatory. They assisted numerous special experiments and provided the essential data for this thesis. My heartfelt gratitude goes to Drs. Tammy M. Weckwerth and Tai-Chi Chen, who firstly planted the seed of radar refractivity in me and encouraged me all the way. I also thank Profs. Luc Fillion, Daniel Kirshbaum and Peter Yau for their suggestions in group meeting and discussions.

I would like to express my appreciation to the radar group : Madalina Surcel, Jonathan Vogel, Aitor Atencia, Bernat Puigdomènech Tresserras, Andres Perez, and Konstantinos Menelaou for their insightful opinions and moral support in the office. I particularly thank Madalina and Jonathan for translating the French abstract and reviewing the drafts. I also thank Kao-Shen Chung, Ting-Chi Wu, Dominik Jacques, and Weiguang Chang for their time explaining data assimilation and processing of model data. Special thanks to Michael Havas for his strong IT support and magically rescuing the computers.

Last but not least, I am deeply grateful to my dearest family, particularly my parents Jia-Shen and Chuan, for their unconditional strong support and loves.

Contents

List of Tables

List of Figures

Chapter 1

Introduction

Moisture observations in the lower atmosphere are considered important for improving our knowledge and forecasts of convective storms (Weckwerth et al., 1999; Weckwerth, 2000; Pielke, 2001; Sherwood et al., 2010). The timing and the location of convection initiation is sensitive to the variability of moisture and temperature at the surface and in the boundary layer, particularly along storm-produced gust fronts, cold pools, and the boundary convergence zone (Zawadzki et al., 1981; Wilson et al., 1998; Weckwerth and Parsons, 2006; Wilson and Roberts, 2006; Weckwerth et al., 2014; Madaus and Hakim, 2016). From numerical model simulations, a moisture variability of 1 g kg^{-1} in the boundary layer affects initiation and intensity of convection (Crook, 1996). However, the deficit in moisture observations is one of the limitations of precipitation forecasting (Emanuel et al., 1995; Dabberdt and Schlatter, 1996). Accurate high spatial-temporal resolution moisture observations in the lower atmosphere are thus needed for the advanced high-resolution storm-scale numerical weather prediction (NWP) models with a rapid update cycle data assimilation to update the correct atmospheric states and to improve the accuracy of short-term quantitative precipitation forecasting (Hanley et al., 2011; Done et al., 2012; Sun et al., 2013; Jacques et al., 2017).

Most operational moisture observations nowadays provide data at single locations (e.g. surface stations, aircraft) and in profiles (e.g. soundings, radiometers, space-based GPS receivers). The research community has been focused on improving the data resolution and quality of the boundary layer moisture profiles, using instruments such as the water vapor differential absorption lidar (DIAL), atmospheric emitted radiance interferometers (AERI) etc. (Carbone et al., 2012; Wulfmeyer et al., 2015; Späth et al., 2016). Nevertheless, high-resolution observations of the horizontal moisture distribution in the lower atmosphere are still scarce. A rare yet promising approach to assess the horizontal structure of humidity within the surface layer is the estimation of refractivity fields by ground-based weather radars (Fabry et al., 1997).

1.1 Radar-estimated refractivity and meteorology

The refractive index of air, n, determines both the speed and the trajectory of propagation of electromagnetic waves. Near the surface, n is approximately 1.0003 and its variation is in the fourth decimal places or less. For convenience, the scientific community defines a quantity called refractivity, $N = (n-1)\times 10^6$, to easily show the variation. N is determined by pressure P (hPa), temperature T (K), and vapor pressure e (hPa), and that dependence makes it meteorologically interesting to measure. At microwave frequencies, the empirical approximation of refractivity is (Smith and Weintraub, 1953):

$$N \simeq 77.6\frac{P}{T} + 373000\frac{e}{T^2}. \tag{1.1}$$

As shown in Fig. 1.1, the value of refractivity changes with various conditions of temperature and moisture. The range of refractivity values expands with increasing temperature. Thus, in a warm environment, refractivity is particularly sensitive to the moisture change. For example, changes of 1°C in temperature or 0.2 hPa in vapor pressure (e.g., 0.2°C in dew point temperature at 18°C) result in 1 N-unit of refractivity change. The cause of the horizontal spatial variability in N fields is mainly dominated by the the variation of moisture. Qualitatively, the spatial distribution of N is a proxy for a near-surface moisture map. Quantitatively, moisture can be recovered with an error in the dewpoint temperature of the order of 0.25°C given an average pressure and temperature over the radar coverage (Fabry and Creese, 1999).

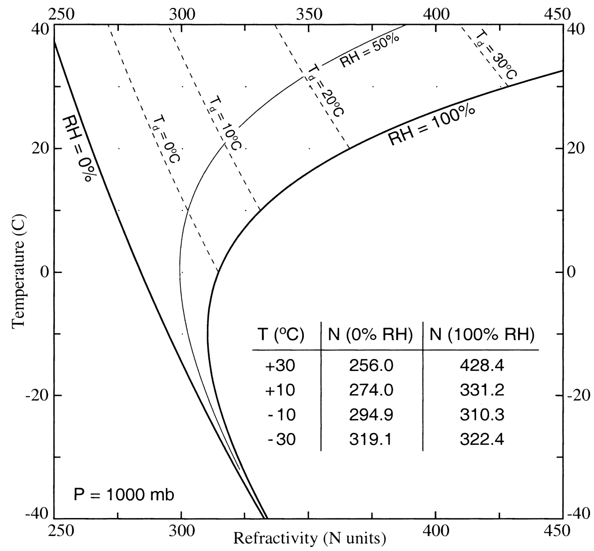

Figure 1.1 – Value of refractivity for given temperature and moisture when the pressure is 1000 hPa (Fabry et al., 1997).

Fabry et al. (1997) proposed a technique to measure the two-dimensional refractivity fields of near-surface air by using weather radars and ground targets. Refractivity changes the speed of the radar wave and the time t_{travel} that waves travel back and forth between the radar and the fixed ground target at range r. They used the the radar-measured phase ϕ of a stationary point-like target at the ground to monitor the changes in t_{travel}, corresponding to the temporal variation of N. The phase measurement of the point target can be presented as:

$$\phi(r) = 2\pi f t_{travel} = \frac{4\pi f}{10^6 c} \int_0^r [N(r', t) + 10^6] dr', \tag{1.2}$$

where f is the radar frequency and c is the speed of light in vacuum. The observed phase easily exceeds 2π with increasing distances, but the phase is only recorded within $\pm\pi$ and is thus aliased. Furthermore, uncertainties in the range r of the order of a few centimeters is sufficient to change the phase by more than π. To mitigate the problems of phase aliasing and of the uncertainty on target distance, the phase difference $\Delta\phi$ between a scan at time t and one at a reference time t_{ref} is used to derive the path-averaged refractivity change using:

$$\Delta\phi = \phi_t - \phi_{t_{ref}} = \frac{4\pi f}{10^6 c} \int_0^r \left[N(r', t) - N(r', t_{ref})\right] dr'. \tag{1.3}$$

The reference phase $\phi_{t_{ref}}$ is determined when the reference refractivity field is nearly horizontally uniform at a calibration stage. Then, the refractivity value, in real time, can be obtained by adding the averaged refractivity change derived from $\Delta\phi$ to the known reference refractivity field. Small-scale variation of refractivity between neighboring targets along the same azimuth can be estimated from the radial gradient of phase difference, $\Delta\phi/\Delta r$. High temporal (5-10 minutes) and spatial (4 by 4 km in horizontal after smoothing) resolution N data can be obtained depending on the radar scanning strategy and ground target distribution. The coverage of the N field is usually within a 40 to 60 km radius of the radar depending on the target density and radio wave propagation conditions.

Previous studies have demonstrated the potential utility of N maps for studying near-surface moisture variation associated with a variety of weather phenomena, such as convection initiation, evolution and characteristics of the boundary layer (Weckwerth et al., 2005; Fabry, 2006; Buban et al., 2007; Koch et al., 2008; Roberts et al., 2008; Bodine et al., 2010; Wakimoto and Murphey, 2010). Significant horizontal refractivity gradients with finer structures have been observed associated with different kinds of boundaries, such as storm outflows, dry lines and many more. The range up to which refractivity data can be collected is limited; to go beyond, use of a radar network is suggested. A network technique has been developed for merging multiple radars to extend the coverage of refractivity observation (Hao et al., 2006; Roberts et al., 2008; Fritz and Chandrasekar, 2009). In addition, the radar-estimated refractivity technique has been applied to the operational radar networks in France and United Kingdom (Nicol et al., 2014; Besson et al., 2016).

Thanks to the refractivity measurements by radar, we gain insight on the finer thermodynamic variability and boundary detection in the lower boundary layer. Since radar refractivity presents the near-surface thermodynamic environments, attempts have been made to assimilate refractivity into NWP models in order to improve the short-term forecasting (Montmerle et al., 2002; Sun, 2005; Gasperoni et al., 2013; Seko et al., 2017).

These preliminary results showed that the quantity and distribution of low-level moisture modified based on radar N lead to better quantitative precipitation forecasting. The WMO (2015) has also encouraged more research on the impact of assimilating refractivity for real cases to show the scientific values of this data in operational high-resolution NWP models. But, an obstacle towards that goal is that the quantitative knowledge of observational data error structure remains unknown and requires further exploration for proper usage in data assimilation.

1.2 The problem of data quality of radar-estimated refractivity

When comparing refractivity measured by the radar and other instruments in the boundary layer, trends are consistent and show high correlations (Fabry, 2004; Weckwerth et al., 2005). However, there are some temporal (diurnal) discrepancies, particularly in the warm season (Bodine et al., 2011). The representative height of the data and the vertical gradient of the refractivity (dN/dh) were first thought to explain the difference in the comparisons (Fabry, 2004). During the daytime with a well mixed boundary layer, the refractivity through the surface layer is more uniform and its gradient in height dN/dh is closer to zero. Hence, the radar-estimated refractivity was shown to represent N from the surface to about 200 m based on comparisons with other sensors (Weckwerth et al., 2005). On the contrary, in the nighttime with a stable nocturnal boundary layer, the difference of refractivity between radar estimation and surface data becomes greater. This increasing difference can be qualitatively explained by the largely negative value of dN/dh near surface, which is constructively contributed from the presence of the temperature inversion and the water vapor pressure gradient. Even though the variation of dN/dh can partially explain the temporal difference of data comparisons, *the representative height of the radar-estimated refractivity still needs to be quantitatively determined*. In addition, some local discrepancy in refractivity comparison still requires further investigation as well.

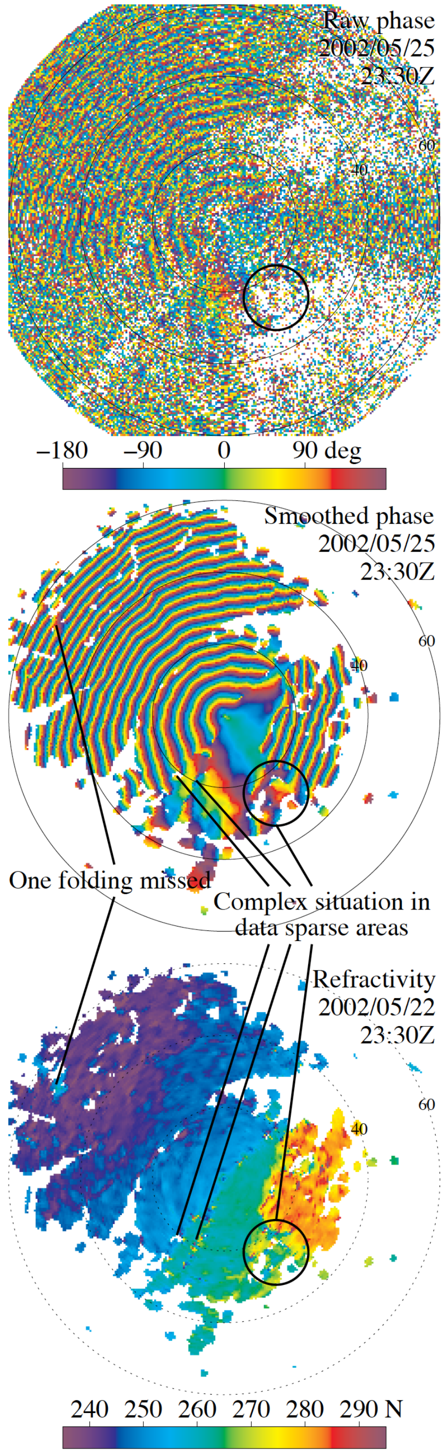

Figure 1.2 – Example of data processing from phase measurements to refractivity field. Top: $\Delta\phi$ field, observed raw phase field after subtracting the reference phase. Middle: $\Delta\phi$ field after a 4 by 4 km smoothing. Bottom: refractivity field obtained from the smoothed $\Delta\phi$ field (Fabry and Pettet, 2002).

To explore the essential problem of the data quality of the radar-estimated refractivity, we must reconsider the nature of the measurement taken, the theoretical background behind the approach, and its implementation. Since the estimation of local N is a result of the radial gradient of phase difference, the quality of the N field critically depends on the information provided by phase measurement. However, the observed $\Delta\phi$ field is noisy (Fig. 1.2, up), and makes it challenging to estimate the N field. Dealing with the noisy $\Delta\phi$ field requires additional sophisticated data processing, such as areal smoothing (Fig. 1.2, middle), and also introduces some abnormal local uncertainties in N (Fig. 1.2, bottom). In addition, the noisiness of $\Delta\phi$ is time dependent, and particularly noisier for short-wavelength radars and at far range.

The phase measurement of a given ground target is the sum of phases due to refractivity changes along the beam path and of other sources of phase variability. Understanding the noise in $\Delta\phi$ introduced by the several sources of uncertainty is important to advance the knowledge on the characteristics of the uncertainties of the N field. Possible sources leading to noisy $\Delta\phi$ and poorer quality of refractivity estimates are discussed below and fall into three categories: ground target quality, radio wave propagation conditions, and radar hardware.

Ground targets

The phase returned from ideal ground targets provide representative information for refractivity variations. Not all returns from ground targets are suitable for refractivity estimation. The ideal ground targets must be stationary and point-like, such as communication towers, power poles etc. On the contrary, phase returns from vegetation swaying with the wind, water bodies, vehicles, extended buildings containing other information much more than the refractivity change might contaminate the refractivity estimation. The quality of a ground target for radar-estimated refractivity purposes can be affected by a variety of processes:

- Target movements: Judicious selection of fixed ground targets is essential; otherwise, moving targets will result in uncertainties in $\Delta\phi$. A radial displacement of half a

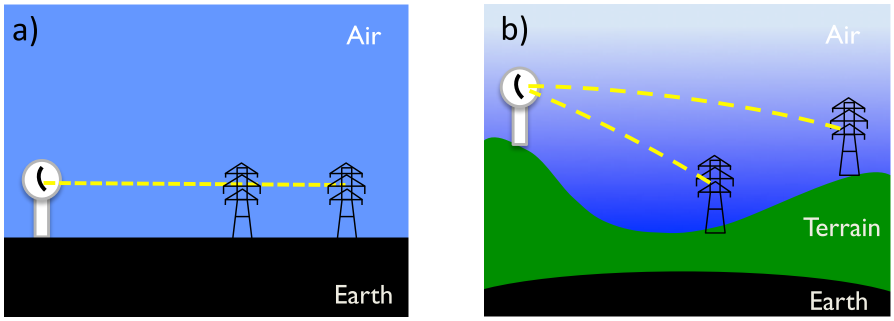

Figure 1.3 – Conceptual illustrations of refractivity estimations between the radar and reliable ground targets (e.g. power towers). (a) A simplified assumption made in Fabry et al. (1997): ground targets and the radar are aligned at a flat ground without considering the Earth curvature and dN/dh. (b) In real case, ground targets at various height above the terrain are not aligned with the radar. The radar beam path is not straight as (a) while considering dN/dh.

wavelength, i.e., 5 cm for S-band radars, leads to a 2π phase variation. Good fixed targets are power poles, communication towers, buildings and others, whose position relative to the ground does not vary with time. In addition, returned phases from sidelobes or contamination by strong neighboring targets should be excluded in order to obtain real gradients of phase variation (Nicol and Illingworth, 2012). In summary, any unreliable target must be intelligently identified and eliminated.

- Variability in target height: The technique of refractivity estimation as originally developed makes simple assumptions: targets are on a flat Earth and all aligned with the height of radar antenna (Fabry et al., 1997), see Fig. 1.3a. However, real targets are at various heights. The variability of target height differences combined with the change in dN/dh (Fig. 1.3b) introduces noisy $\Delta\phi$ and significant bias in N (Fabry, 2004). The previous assumptions were made because both of the heights of targets and the refractivity profile (dN/dh) were unknown. In addition, these unknown factors combined with the Earth's curvature makes the beam path more complicated (Park and Fabry, 2010). Besides, the representative heights of targets must be acquired to improve the utility of refractivity estimation, such as comparison with other instruments and data assimilation.

- Uncertainty in target location: Ground targets can be located anywhere within the range gates. The measured phase from unknown location of targets might not well represent the phase at the known range as the center of range gates and result in uncertainties of refractivity estimation. Additional phase differences also occur due to the uneven target spacing (distance) associated with the changes in the transmitted frequency. This kind of phase noisiness is proportional to the magnitude of refractivity variation. Decreasing the pulse width has been suggested to help better locate the ground targets and avoid the mixing of the signal between close targets (Nicol et al., 2013; Besson and Parent du Châtelet, 2013).

Radar wave propagation conditions

The phase measurements not only record the changes in horizontal N, but also other sources of propagation conditions along the radar beam path.

- Variations in the vertical profile of refractivity (dN/dh): Evolving dN/dh causes systematic refractivity biases as it affects the beam trajectory (Fig. 1.4a), the associated target range (Figs. 1.4b and c), and the refractivity field sampled between selected targets of different heights. Park and Fabry (2010) developed a theoretical simulator to explore the observed noisy phase difference ($\Delta\phi$) by considering the temporal change in dN/dh and the different target heights. The noisy phase difference caused by this term is an important but unsolved problem of the radar-estimated refractivity technique. One possible solution to eliminate the biases due to these effects is to obtain the phase reference fields $\phi_{t_{ref}}$ in all kinds of dN/dh situations. Fabry and Pettet (2002) used two reference phase fields at different dN/dh to reduce the noisy phase difference and the bias of refractivity estimation. But, in reality, it is not practical to obtain reference phases for a wide range of dN/dh. On the other hand, although dN/dh can be estimated by using the ground echo coverage at low elevations (Park and Fabry, 2011), the exact heights of the targets are unknown. Hence, the problem of noisy phase differences and biased refractivity remains unsolved.

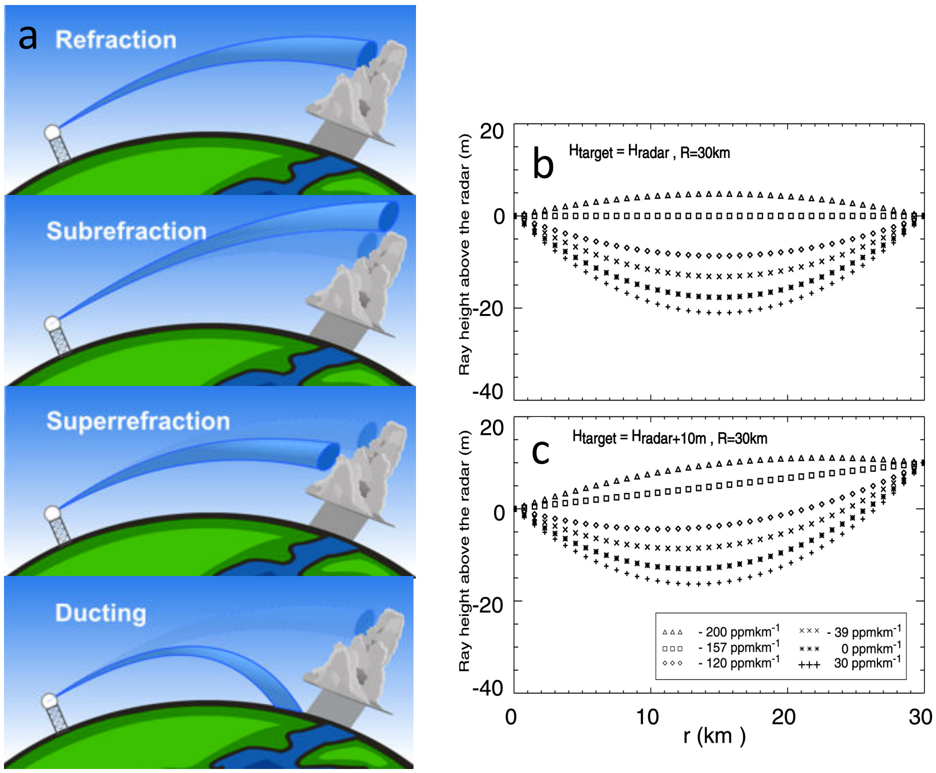

Figure 1.4 – (a) Radar beam propagation under different conditions of vertical gradient of refractivty (dN/dh): normal refraction ($dN/dh = -40\ km^{-1}$), subrefraction ($dN/dh > -40\ km^{-1}$), superrefraction ($dN/dh < -40\ km^{-1}$), and ducting ($dN/dh < -157\ km^{-1}$). The figures are adapted from `http://www.srh.noaa.gov/jetstream/doppler/beam_max.html`. (b) The radar beam path toward a given ground target located 30 km away and at the same height as the radar under various propagation conditions. During very negative dN/dh, the radar beam path propagates toward the ground, and thus a higher antenna elevation is required to reach the target, and vise versa. (c) Same as (b), but the height of the target is 10m higher than the radar (Park and Fabry, 2010).

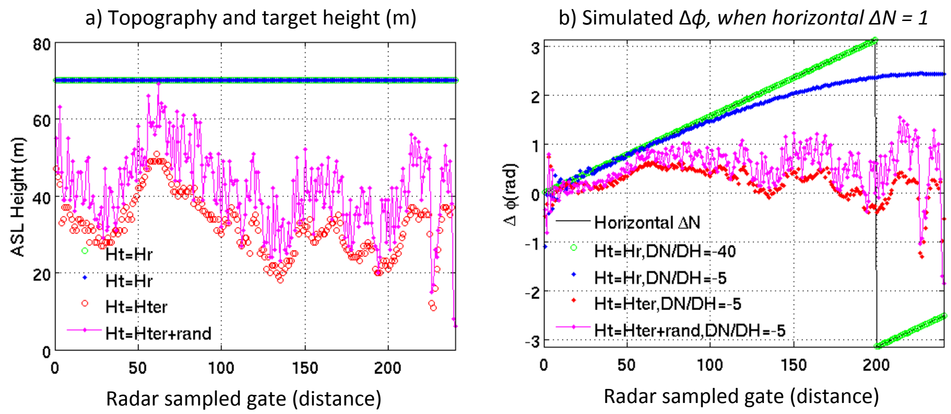

Figure 1.5 – Radial phase variation with a variety of target heights (H_T) when temporal N change is equal to 1 N-unit homogeneously. a) Ground targets of different heights as a function of distance away from the radar. The length of each sampled gate is 125 m. The green and blue lines show that H_T along the radial distance equals the height of radar. The red circles present H_T on the varying terrain, whereas the magenta line indicates random heights above the terrain. b) Corresponding $\Delta\phi$ with the target height. Note that the green line as the reference shows the radial variation of $\Delta\phi$ while no dN/dh change and good height alignment. Other lines in different colors represent $\Delta\phi$ at varying Ht as shown in a) and with changes in dN/dh.

Based on Park and Fabry (2010), the noise in phase differences of targets at different heights is simulated (Fig. 1.5). Given a constant temporal N change equal to 1, $\Delta\phi$ is expected to increase linearly with range (black line). If dN/dh does not change and target height is aligned with radar height, the radial $\Delta\phi$ (green dot) is identical to what would be expected from the specified change in N. However, when dN/dh changes but target heights are similar, there is an increasing discrepancy associated with the change in the radar beam trajectory caused by changes in propagation conditions. Furthermore, for targets at terrain height (red line in Fig. 1.5a) and at random representative heights above the terrain (magenta line in Fig. 1.5a), the corresponding $\Delta\phi$ (red and magenta lines in Fig. 1.5b) show both increasing noisiness and biases. The bias is introduced here through the significant change of $\Delta\phi/\Delta r$.

- Precipitation: Precipitation along the beam path introduces propagation delay and causes a refractivity bias. When the average rainfall rate along the beam path is 13mm hr^{-1}, the refractivity bias is 1 N-unit. If the rainfall rate is known, the refractivity bias caused by the precipitation can be estimated and corrected (Bodine et al., 2011).

Radar hardware

For radars with a non-coherent transmitter such as those based on magnetrons, the transmitted frequency might drift and the local oscillator frequency may or may not change as a result. The phase difference can change abruptly causing biases in the derived refractivity field. This bias can be corrected for if the changes in the local oscillator frequency are known (Parent du Chatelet et al., 2012; Nicol et al., 2013).

In summary, understanding the quality of the phase characteristics of ground targets is the first step in learning the uncertainties of radar-derived refractivity. Methods for estimating biases caused by the radar hardware have mostly been developed. *Yet, data quality problems of phase measurements related to propagation conditions and the properties of targets still remain challenging to quantify and improve.*

1.3 Structure of the thesis

This thesis aims to quantitatively characterize the uncertainties of phase measurements and the resulting refractivity estimation. Knowledge on the data quality is key for future quantitative applications, e.g. data assimilation, radar network implementation, instrument synergy, etc. Understanding the limitation of the current refractivity estimation technique is also needed in order to lead future improvements on the method. This thesis thus examines the unresolved issues on the data quality of phase measurements and their impacts on radar-estimated refractivity in three aspects, including the radar hardware, radar wave propagation, and ground targets.

In Chapter 2, the theoretical underpinning of the refractivity estimation by radar is rederived in the context of a spherical Earth and of radar and targets at different altitudes given varying dN/dh conditions. This was motivated by observations of the difference of N

between estimates derived by radar and data collected by other instruments that reveal the unclear height representativeness of radar-estimated N under evolving dN/dH conditions. In addition, the temporal changes in dN/dh and the varying heights of ground targets introduce noisiness to the phase measurements that affect the quality of N estimation. The resulting uncertainties on N estimation is quantified and discussed.

In Chapter 3, the phase characteristics of a point-like ground target as a function of azimuth and elevation are explored as a prerequisite for properly interpreting and using the phase information of targets at multiple elevation angles. This analysis revealed the effect of a radar hardware characteristic understudied in radar meteorology, the phase pattern of radar antennas. The impacts on the data quality of radar-derived measurements in general and on estimated N in particular caused by the antenna phase pattern are investigated and quantified for the first time.

In Chapter 4, the random uncertainty of phase from each individual ground target and its impact on N estimation are examined and estimated. Particular attention was focused both on establishing the causes of noisiness in phase measurements as well as on trying to devise methods to establish their magnitude.

A summary of the work performed on establishing data quality and some unexplored avenues for new applications of radar refractivity measurements are presented in Chapter 5.

Note that in accordance with thesis regulations of McGill University, I chose to write the research section of this thesis from a collection of scholarly manuscripts I am the lead author of. Individual manuscripts being self-contained, some overlap and repetition between chapters is unavoidable.

Chapter 2

Improving radar refractivity retrieval by considering the change in the refractivity profile and the varying altitudes of ground targets

Occasional refractivity biases associated with the diurnal variation of the vertical gradient of refractivity negatively affect quantitative applications. In parallel, the height representativness of refractivity remains a challenge when comparing estimations with other instruments. To tackle these problems, this chapter investigates the information provided by phase measurements through considering the variation of refractivity profiles and height differences between ground targets and the radar, as opposed to the simplified assumptions made in Fabry et al. (1997), and their impact on the biases of refractivity estimation.

The chapter was based on this published paper: Feng, Y., F. Fabry, and T.M. Weckwerth, 2016: Improving Radar Refractivity Retrieval by Considering the Change in the Refractivity Profile and the Varying Altitudes of Ground Targets. J. Atmos. Oceanic Technol., 33, 989–1004, doi: 10.1175/JTECH-D-15-0224.1.

Improving radar refractivity retrieval by considering the change in the refractivity profile and the varying altitudes of ground targets

Ya-Chien Feng[1], Frédéric Fabry[1], and Tammy M. Weckwerth[2]

[1]Department of Atmospheric and Oceanic Sciences, McGill University, Montreal, Quebec, Canada

[2]Earth Observing Laboratory, University Corporation for Atmospheric Research, Boulder, Colorado, United States

Abstract

Accurate radar refractivity retrievals are critical for quantitative applications, such as assimilating refractivity into numerical models or studying boundary layer and convection processes. However, the technique as originally developed makes some simplistic assumptions about the heights of ground targets (H_T) and the vertical gradient of refractivity (dN/dh). In reality, the field of target phases used for refractivity retrieval is noisy due to varying terrain and introduces estimation biases. To obtain a refractivity map at a constant height above terrain, a 2-D horizontal refractivity field at the radar height must be computed and corrected for altitude using an average dN/dh. This is achieved by theoretically clarifying the interpretation of the measured phase considering the varying H_T and the temporal change of dN/dh. Evolving dN/dh causes systematic refractivity biases as it affects the beam trajectory, the associated target range, and the refractivity field sampled between selected targets of different heights. To determine H_T and dN/dh changes, a two-fold approach is proposed: first, H_T can be reasonably inferred based on terrain height; then, a new method of dN/dh estimation is devised by using the property of the returned powers of a point-like target at successive antenna elevations. The dN/dh obtained shows skill based on in-situ tower observation. As a result, the data quality

of the retrieved refractivity may be improved with the newly added information of dN/dh and H_T.

2.1 Introduction and Motivation

High-resolution near-surface moisture is crucial to pursue knowledge of convective and boundary layer processes (Weckwerth et al., 1999; Weckwerth, 2000; Sherwood et al., 2010). From numerical model simulations and data analysis, convection initiation and quantitative precipitation forecasting are shown to be sensitive to accurate measurements of moisture and temperature variability at the surface and in the boundary layer (e.g., Zawadzki et al., 1981; Crook, 1996; Weckwerth et al., 1999). However, moisture observations at high temporal and spatial resolution in the lower boundary layer are not readily available. The lack of information on moisture is one of the main limitations of mesoscale short-term forecasting (Emanuel et al., 1995; Dabberdt and Schlatter, 1996; Fabry and Sun, 2010; Hanley et al., 2011).

Fabry et al. (1997) proposed a method to measure the refractivity (N) of near-surface air by using weather radars and fixed ground targets. This approach provides insight on small-scale low-level horizontal humidity variations through the retrieved refractivity map by radars and it may partially fill the observational data gap in the lower boundary layer. Refractivity, $N = (n - 1) \times 10^6$, is used for convenience to show the variation of n. Refractivity is a function of pressure P (hPa), temperature T (K), and water vapor pressure e (hPa). At microwave frequencies, the empirical approximation of refractivity is (Smith and Weintraub, 1953):

$$N \simeq 77.6\frac{P}{T} + 373000\frac{e}{T^2}. \tag{2.1}$$

Refractivity is more sensitive to moisture variation; for example, changes of 1 °C in temperature or 0.2 hPa in vapor pressure (e.g., 0.2 °C in dew point temperature at 18 °C) result in 1 unit of refractivity change. Fabry (2006) further noted that the variation of water vapor is the main source of the spatial variability of refractivity in summer-like conditions.

Comparisons between refractivity measured by the radar and other instruments in the boundary layer show high correlations in time and space (Fabry et al., 1997; Weckwerth et al., 2005; Bodine et al., 2011). Since high temporal (about 5 to 10 minutes) and spatial (4 km by 4 km in the horizontal after smoothing) resolution refractivity retrievals have been obtained, many studies have demonstrated the potential utility of refractivity maps for studying near-surface moisture variation associated with a variety of weather phenomena, such as convection initiation, convection evolution and characteristics of the boundary layer (Weckwerth et al., 2005; Fabry, 2006; Buban et al., 2007; Chen et al., 2007; Roberts et al., 2008; Koch et al., 2008; Besson et al., 2012; Nicol et al., 2014). Refractivity maps not only provide small-scale moisture variability particularly in those areas without a dense mesonet, but also show boundaries prior to the fine line of traditional reflectivity (Weckwerth et al., 2005; Heinselman et al., 2009; Wakimoto and Murphey, 2010; Bodine et al., 2011). However, the coverage range of refractivity data is about 40-60 km, dictated by the topography and radio wave propagation. The range up to which refractivity data can be collected is limited; to go beyond, a radar network is needed. Thus, a networked technique has been developed for merging multiple X-band radars to extend the coverage of refractivity observations (Hao et al., 2006; Fritz and Chandrasekar, 2009).

Montmerle et al. (2002) and Sun (2005) assimilated radar refractivity information to adjust the quantity and distribution of low-level moisture. The newly added information not only modified the low-level humidity field but also changed the spatial variability of moisture, which enhanced the intensity of the storm leading to better quantitative precipitation forecasting. As a result, the research community has been preparing to assimilate the composite refractivity data from operational radar networks to numerical models in order to improve short-term forecasting skill (Besson et al., 2012; Caumont et al., 2013; Gasperoni et al., 2013; Nicol et al., 2013; Nicol and Illingworth, 2012; Nicol et al., 2014).

For such quantitative applications, the accuracy of the refractivity retrieval is important and thus it is critical to gain more knowledge about the biases and the representativeness of the retrieval. Though the quality of the retrieval has been discussed from different aspects and improved in the last decade (Fabry, 2004; Park and Fabry, 2010; Besson et al., 2012; Parent du Chatelet et al., 2012; Caumont et al., 2013; Nicol et al., 2013; Nicol and Illingworth, 2012), the unsolved problem associated with the vertical gradient of refractivity (dN/dh) and uneven target heights (H_T) remains challenging. A consequence of these issues is the difficulties of assigning a height to the retrieved refractivity fields and the prominent diurnal periodicity of the refractivity difference between in-situ observations and the radar estimations (Fabry, 2004; Weckwerth et al., 2005; Bodine et al., 2011). The net result is that the refractivity retrieval is representative of conditions over different heights; for example, it can represent the lower 250 m of the boundary layer when the convective boundary layer is well mixed in summer daytime conditions, but a much shallower layer in the nighttime (Weckwerth et al., 2005).

The goal of this research is to rethink refractivity retrieval to obtain a more accurate near-surface 2-D horizontal refractivity map at a given representative height and additional information on dN/dh. In section two, the assumptions in the original method are revisited and the refractivity biases associated with the H_T and dN/dh are clarified and quantified. Then, a new method for estimating the representative H_T and dN/dh by using echo strength variations of ground targets is introduced in section three. The estimated dN/dh from the radar and targets is compared with in-situ observation in section four. In the last section, the improvements and limits of the retrieval method are summarized by applying the newly obtained information.

2.2 Phase difference and refractivity

2.2.1 The basis of radar refractivity retrieval

The concept of radar refractivity retrieval is based on the varying time, t_{travel}, that electromagnetic waves travel back and forth between the radar and a ground target. The time is affected by the refractive index along its propagating path and can be expressed as:

$$t_{travel} = 2r\frac{n}{c}, \tag{2.2}$$

where r is the one-way beam path range from the radar to the target and c is the speed of light in vacuum. Fabry et al. (1997) used the phase of a fixed ground target as a proxy for the time. Given a stable radar transmitter frequency (f), the radar-measured phase (ϕ) of a stationary point ground target depends on the time taken by a radar pulse for a two-way path:

$$\phi(r) = 2\pi f t_{travel} = \frac{4\pi f}{10^6 c} \int_0^r [N(r', t) + 10^6] dr'. \tag{2.3}$$

The observed phase largely exceeds 2π while the phase measurement is aliased within $\pm\pi$. To mitigate somewhat this problem of phase aliasing, the phase difference ($\Delta\phi$) of a stationary ground target between a scan at time t and at a reference time t_{ref} can provide the information of the path-averaged refractivity variation:

$$\Delta\phi = \phi_t - \phi_{t_{ref}} = \frac{4\pi f}{10^6 c} \int_0^r [N(r', t) - N(r', t_{ref})]\, dr'. \tag{2.4}$$

The reference phase ($\phi_{t_{ref}}$) is determined while the reference refractivity field ($N_{t_{ref}}$) is assumed to be nearly horizontally uniform with a known refractivity at t_{ref}, which is usually during or after stratiform rain in windy and cool conditions. Based on Eq. (2.4), the average change of refractivity along the beam path, $\overline{\Delta N} = \overline{N(t)} - \overline{N(t_{ref})}$, can be derived from the radial gradient of phase difference, $d\Delta\phi/dr$. From these measurements, small-scale variations of refractivity among the reliable fixed ground targets can be estimated from the slope of phase difference between the neighboring target pairs. For example, the local refractivity variation between targets T_1 and T_2 on the same azimuth is proportional to the gradient of the phase difference between these targets, $(\Delta\phi_{T_2} - \Delta\phi_{T_1})/(r_{T_2} - r_{T_1})$. Consequently, the refractivity value can be obtained by adding the refractivity change field to the known reference refractivity field.

2.2.2 Revisiting the assumptions and unsolved problems

The accuracy of retrieved refractivity critically depends on the quality of the phase differences of reliable ground targets. Phase differences caused by reasons other than the real atmospheric refractivity variations lead to noisiness in $\Delta\phi$ fields and bias the refractivity retrievals. Therefore, quantifying the noise in $\Delta\phi$ introduced by different sources of uncertainties will enable improvements to the current retrieval algorithm. Possible sources leading to poorer refractivity estimates are discussed in many works and fall in the following three categories: 1) target uncertainty in its stability, height, and location (Fabry et al., 1997; Fabry, 2004; Besson et al., 2012; Nicol and Illingworth, 2012; Nicol et al., 2013); 2) propagation conditions associated with dN/dh and height difference between the radar and ground targets (Fabry, 2004; Park and Fabry, 2010; Bodine et al., 2011); and 3) drifts in the transmitter frequency (Parent du Chatelet et al., 2012; Nicol et al., 2013). Here, the focus is on the most basic unsolved part: the effects of atmospheric propagation conditions and the height differences between the radar and the targets.

The simplistic assumptions that were originally made by Fabry et al. (1997) to obtain a 2-D refractivity field are as follows: 1) the heights of selected targets and the radar antenna height are identical ($H_T = H_R$); 2) the Earth's curvature is neglected; or alternatively, dN/dh is -157 km^{-1} everywhere; 3) the reference refractivity map is uniform and constant. Yet, these conditions are generally not realistic: real targets are at various heights, such as on hilly terrain or in an urban area, while dN/dh evolves diurnally and changes significantly with weather conditions, affecting the propagation of radar beam path and r. Consequetly, r cannot be considered constant.

As a result, since targets are at different heights under varying dN/dh conditions, the field of measured phase difference between nearby pairs of targets is noisy. A noisy phase difference field makes dealiasing and the estimation of small-area radial gradients of $\Delta\phi$ more difficult, lowering the quality of the refractivity retrieval, particularly for short-wavelength radars and for targets at far ranges. To limit this problem, in post-processing, the noisy phase differences are generally smoothed by either a pyramidal weighting function over a 4-km by 4-km area or a least squares fit (Fabry, 2004; Hao et al., 2006; Nicol et al., 2013). The smoothing process washes out the unrealistic sudden local refractivity change due to the noisy $\Delta\phi$ problem. Caumont et al. (2013) also suggested a new weighting parameter for extracting meaningful signal and smoothing the noisiness of retrieved refractivity change. Nonetheless, the smoothing process reduces the spatial resolution of the data and does not fully resolve the incorrect physical biases introduced by dN/dh and target height variability.

2.2.3 Reinterpretation of the measured $\Delta\phi$

The observed phase is affected by the horizontal and vertical variation of refractivity along the radar beam path from the radar to the ground target. Park and Fabry (2010) developed a simulator to explore the observed noisy phase difference by considering the temporal change of vertical variation of refractivity and the height difference between targets and the radar. The temporal phase difference of a point target at time t and t_{ref} is expressed as:

$$\begin{aligned}\Delta\phi = \frac{4\pi f}{10^6 c}\Bigg\{ & \underbrace{\overline{N(t)}r - \overline{N(t_{ref})}r_{ref}}_{\text{(i)}} + \underbrace{(H_T - H_R)\left[\frac{dN}{dh}\frac{r}{2} - (\frac{dN}{dh})_{ref}\frac{r_{ref}}{2}\right]}_{\text{(ii)}} \\ & - \underbrace{\left[\frac{dN}{dh}\left(\frac{1 + (a+H_R)\frac{1}{10^6}(\frac{dN}{dh})}{12(a+H_R)}\right)r^3 - (\frac{dN}{dh})_{ref}\left(\frac{1 + (a+H_R)\frac{1}{10^6}(\frac{dN}{dh})_{ref}}{12(a+H_R)}\right)r^3_{ref}\right]}_{\text{(iii)}}\Bigg\},\end{aligned} \tag{2.5}$$

with a being the radius of the Earth, and H_T and H_R being the representative heights of the target and the radar above sea level, respectively. The phase change in time of a ground target records the information of: (i) the change of refractivity in the horizontal at the radar height, (ii) the change of refractivity with height associated with the height difference between the radar and the target, and (iii) the ray curvature relative to the curvature of the Earth. This equation theoretically describes the causes of measured $\Delta\phi$, assuming a single homogenous dN/dh at a particular time. It illustrates that phase varies not only as a result of refractivity change along the path, but also because the path range (r) to the target changes when dN/dh varies. If dN/dh varies along beam path, there is no simple analytic formulation for $\Delta\phi$, and the contribution of the changing trajectory to $\Delta\phi$ must be determined by iterations.

Furthermore, the path range is affected by the atmospheric propagation condition and the location of the target, and can be expressed as (Park and Fabry, 2010):

$$r = \left|\frac{dn}{dh}\right|^{-1}\cos^{-1}\left[1 - \frac{C(\frac{dn}{dh})^2}{2}\right], \text{with} \tag{2.6}$$

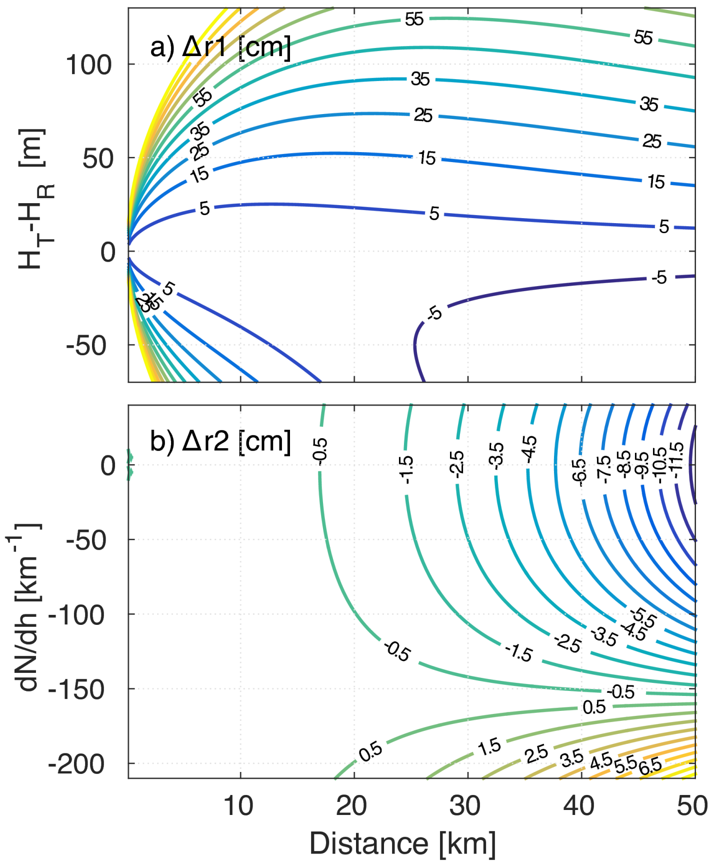

Figure 2.1 – Additional contributions to target ranges caused by target heights H_T and propagation conditions dN/dh (km^{-1}). (a) Range variation Δr_1 in cm as a function of the arc distance D of ground targets and the height difference between the ground target and the radar ($H_T - H_R$). (b) Range change Δr_2 (cm) caused by dN/dh changes with respect to $dN/dh_{ref} = -157\ \mathrm{km}^{-1}$.

$$C = (a + H_R)^2 + (a + H_T)^2 - 2(a + H_R)(a + H_T)\cos\left(\frac{D}{(a + H_R)}\right),$$

where D is the arc distance to the target at the radar height parallel to the sea-level surface. Recall that dn/dh equals to $10^{-6}dN/dh$. Path range hence varies with dN/dh and also depends on the varying height and distance of targets, making (2.5) more complicated than (2.4) that was used previously.

To further clarify the causes of $\Delta\phi$ in (2.5), we separate r into three terms: the arc distance (D) to the target at the radar height, the range variation Δr_1 resulting from the height difference between H_T and H_R given $dN/dh = -157\ \mathrm{km}^{-1}$, and the range variation Δr_2 related to the change in the path given a change in dN/dh as well as independent of

H_T:

$$r = D + \Delta r_1 \left[D, H_T - H_R, \left(\frac{dN}{dh} \right)_{-157} \right] + \Delta r_2 \left[D, \frac{dN}{dh} - \left(\frac{dN}{dh} \right)_{-157} \right]. \tag{2.7}$$

Consequently, the range variation can be separated into effects of differing target heights and of varying $\Delta(dN/dh)$. Figure 2.1 demonstrates that Δr_1 is of the order of tens of centimeters, and Δr_2 is typically a few centimeters, both sufficient to change target phase considerably.

The phase difference equation (2.5) can be revised by substituting r from (2.7) and by neglecting small terms of phase differences using a scale analysis under extreme conditions ($|\Delta\phi| < 1°$ at radar frequencies up to X-band given D up to 50 km, $\Delta(dN/dh)$ up to 200 km^{-1}, and $H_T - H_R$ up to 100 m):

$$\Delta\phi = \frac{4\pi f}{10^6 c} \times \left\{ \underbrace{D[\overline{N(t)} - \overline{N(t_{ref})}]}_{\text{(i) horizontal } \overline{\Delta N} \text{ at } H_R} + \underbrace{\overline{N(t_{ref})}(\Delta r_2 - \Delta r_{2ref})}_{\text{(ii) bias: propagation effect (range)}} + \underbrace{\frac{D(H_T - H_R)}{2} \left[\frac{dN}{dh} - (\frac{dN}{dh})_{ref} \right]}_{\text{(iii) bias: target height effect}} \right.$$
$$\left. \underbrace{- D^3 \left\{ \frac{dN}{dh} \left[\frac{1 + (a + H_R)\frac{1}{10^6}(\frac{dN}{dh})}{12(a + H_R)} \right] - (\frac{dN}{dh})_{ref} \left[\frac{1 + (a + H_R)\frac{1}{10^6}(\frac{dN}{dh})_{ref}}{12(a + H_R)} \right] \right\}}_{\text{(iv) bias: propagation effect (changing beam curvature)}} \right\}. \tag{2.8}$$

Using (2.8), the various contributions to the phase change $\Delta\phi$ can be discussed and analyzed in greater detailed.

The average change of the horizontal refractivity at the radar height ($\overline{\Delta N}_{H_R}$), term (i) in (2.8), is the original term from Fabry et al. (1997). The radial gradient of $\Delta\phi$ of this term is used to obtain a refractivity map at the radar height. In addition, (2.8) clarifies the misleading concept of the (i) term in (2.5), because it represents not only the $\overline{\Delta N}_{H_R}$ but also the range variation Δr_2 due to the propagation effect, term (ii) in (2.8). The result of the scale analysis also shows that the effect of range variations associated with H_T (Δr_1) can be neglected, because Δr_1 does not change with dN/dh, and $\Delta\phi$ caused

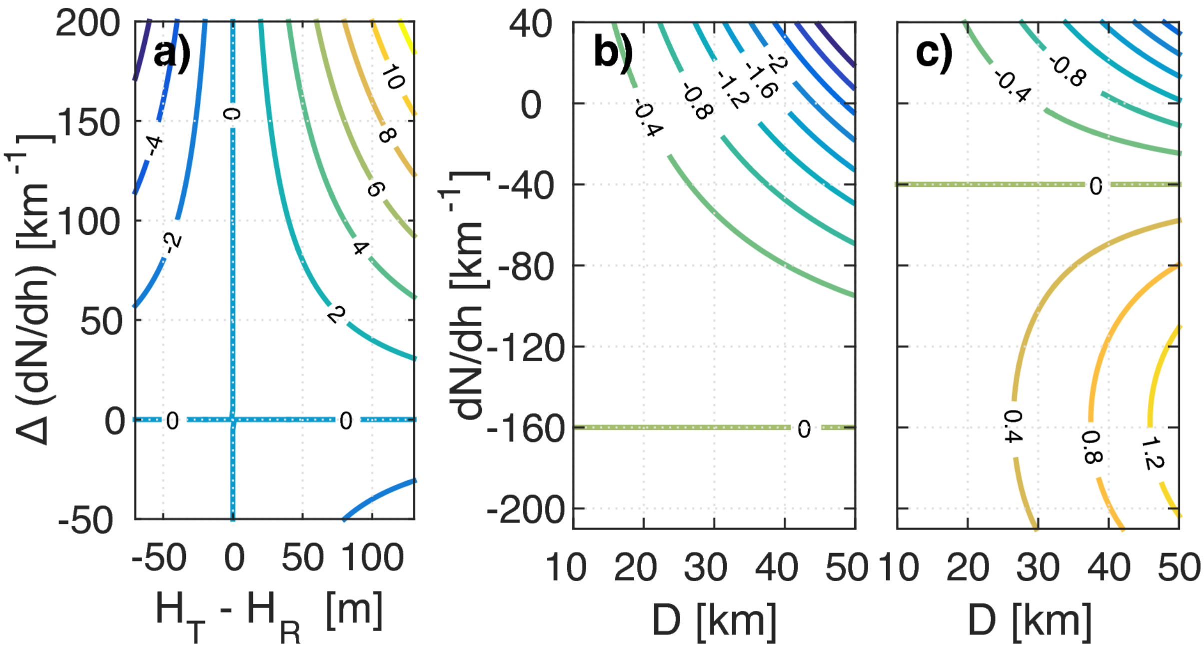

Figure 2.2 – (a) Average refractivity bias $\overline{N_{bias}}$ along the beam path due to target height effects as a function of the height difference between the radar and the target, as well as of the atmospheric vertical refractivity profile difference $\Delta(dN/dh) = dN/dh - (dN/dh)_{ref}$. This $\overline{N_{bias}}$ is calculated based on term (iii) in (2.8). (b) $\overline{N_{bias}}$ related to the change of the beam trajectory defined as terms (ii) and (iv) in (2.8) as a function of the distance to the ground target and dN/dh conditions. Note that this bias also depends on the dN/dh_{ref}, set here as -157 km^{-1}. (c) $\overline{N_{bias}}$ caused by the same effect as (b), but with $dN/dh_{ref} = -40$ km^{-1}.

by $\Delta r_1[N(t) - N(t_{ref})]$ is smaller than 1°. Furthermore, other $\Delta\phi$ terms in (2.8) caused by the effects of variable target heights and the vertical gradient of refractivity result in biases of average refractivity along beam path, $\overline{N_{bias}}$, in the original refractivity retrieval. $\overline{N_{bias}}$ can be expressed by $(10^6 c/4\pi) \times (\Delta\phi/D)$. If H_T and dN/dh can be retrieved using a yet unspecified method, those terms can be accounted for and removed, resulting in a ΔN field that is only related to the horizontal variation of refractivity at H_R.

The temporal variation of the vertical refractivity profile is a source of bias for $\overline{\Delta N}_{H_R}$. Figure 2.2a shows the magnitude of the refractivity bias as a function of the vertical refractivity profile for targets at different heights from H_R, which is calculated from term (iii) in (2.8). For example, when $\Delta(dN/dh)$ changes by 150 km^{-1}, the resulting $\overline{N_{bias}}$ is

2 N-units for a radar and a target 25 m apart in altitude. The term 'N-unit' expresses the fact that the change or bias applies to N, not to another unit-less quantity. Moreover, the observed phase is affected by both the beam path range variation (Δr_2) and the varying propagation conditions the radar ray experiences along these changing paths, i.e., terms (ii) and (iv) in (2.8). $\overline{N_{bias}}$ due to these propagation effects is a function of dN/dh, dN/dh_{ref}, and the distance to the targets. Figures 2.2b and c show how $\overline{N_{bias}}$ changes with propagation conditions for dN/dh_{ref} of -157 and -40 km^{-1}, respectively. For geometry purposes, $dN/dh_{ref} = -157$ km^{-1} is used to help clarify the many contributions to range, Δr_2 then corresponding to the path length added by propagation; from the meteorological point of view, $dN/dh_{ref} = -40$ km^{-1} represents the normal refraction when near surface is under well-mixed conditions and is the dN/dh_{ref} usually used in the retrieval technique. The magnitudes of $\overline{N_{bias}}$ in different dN/dh_{ref} conditions are similar and are all proportional to the variation of dN/dh and target distance, but are relatively smaller than the $\overline{N_{bias}}$ caused by the height effect discussed previously. For instance in Fig. 2.2b, when $\Delta(dN/dh)$ changes from -160 to -40 km^{-1}, $\overline{N_{bias}}$ of the target 25 km away from the radar is about -0.4 N-units.

2.2.4 Noisy $\Delta\phi$ and local N biases

All of the discussion until now focused on biases in N averaged between the radar and a target. Finer resolution of refractivity change is gained from the phase difference between neighboring targets along the same azimuth. However, the targets at different heights or on varying terrain introduce noisiness in $\Delta\phi$ and biases in the refractivity estimated from these $\Delta\phi$. The temporally averaged refractivity change between a target pair, T_2 and T_1, derived from the phase difference gradient between targets is such that,

$$\Delta N_{T_2-T_1} = \frac{\Delta\phi_{T_2} - \Delta\phi_{T_1}}{\frac{4\pi f}{10^6 c}\Delta D} = \underbrace{\Delta\overline{N(t)}_{T_2-T_1}}_{\text{(i) horizontal } \Delta N \text{ at } H_R} + \underbrace{\frac{1}{2}(\Delta\frac{dN}{dh})\left(\frac{H_{T_1}+H_{T_2}}{2} - H_R\right)}_{\text{(ii) } \Delta H \text{ and } \Delta\ dN/dh}$$
$$+ \underbrace{\frac{1}{2}(\Delta\frac{dN}{dh})(\frac{D_{T_1}+\Delta D/2}{\Delta D})(H_{T_2}-H_{T_1})}_{\text{(iii) bias: target height effect}} + \underbrace{\frac{1}{\Delta D}\overline{N(t_{ref})}[(\Delta r_{2T_2} - \Delta r_{2refT_2}) - (\Delta r_{2T_1} - \Delta r_{2refT_1})]}_{\text{(iv) bias: propagation effect (range)}}$$
$$\underbrace{-(D_{T_2}^2 + D_{T_1}D_{T_2} + D_{T_1}^2)\left\{\frac{dN}{dh}\left[\frac{1+(a+H_R)\frac{1}{10^6}(\frac{dN}{dh})}{12(a+H_R)}\right] - (\frac{dN}{dh})_{ref}\left[\frac{1+(a+H_R)\frac{1}{10^6}(\frac{dN}{dh})_{ref}}{12(a+H_R)}\right]\right\}}_{\text{(v): bias: propagation effect (changing beam curvature)}}, \tag{2.9}$$

where ΔD is the arc distance between the target pair $(D_{T_2} - D_{T_1})$ at the radar height. This key equation clarifies the goal and the problems of the refractivity retrieval method in more detail and will be used to improve the original refractivity retrieval.

N at a given height above terrain

In order to quantitatively interpret and apply the refractivity retrieval, one generally wants to estimate the refractivity field at a given height above the terrain. The temporal change of refractivity between targets combines the 2-D refractivity change at the radar height and the change of vertical refractivity difference between the radar and the average height of targets, which are the (i) and (ii) terms of (2.9). However, there are some more residual terms of $\Delta\phi$ that introduce biases in the refractivity. These systematic biases are associated with the evolving dN/dh and the height difference between target pairs. Two aspects of biases are discussed and quantified: the effects of the difference of target heights and the beam trajectory. Both of these biases are proportional to $\Delta(dN/dh)$ and to the distance of targets from the radar.

Local N bias due to target height

The measured $\Delta\phi$ field is biased by the variability of heights of neighboring ground targets. Even with small height differences and small dN/dh changes, the local N bias of

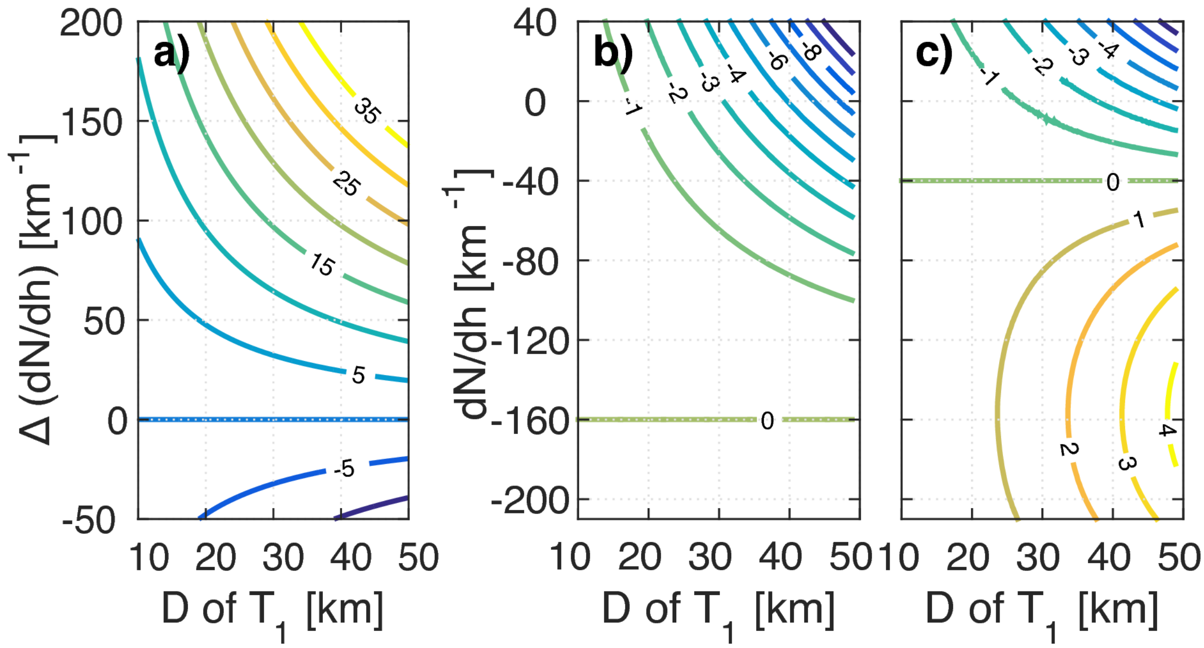

Figure 2.3 – (a) Local refractivity bias due to the effect of the height difference between a pair of neighboring ground targets (T_1 and T_2) 10 m apart in height and 1 km apart in distance. This bias is calculated from term (iii) in (2.9) as a function of distance of T_1 and $\Delta(dN/dh)$. (b) Local N bias associated with the beam propagation effect which causes path length variations and beam curvature changes, i.e., terms (iv) and (v) in (2.9). Note this local N bias is calculated when $dN/dh_{ref} = -157\ km^{-1}$. (c) Same as (b), but with $dN/dh_{ref} = -40$ km^{-1}.

refractivity is significant. According to term (iii) in (2.9), the magnitude of the bias due to the target's height effect can reach tens of N-units (Fig. 2.3a). For targets at around 20 km in range and given $\Delta(dN/dh) = 100$ km^{-1}, a typical summertime diurnal variation of $\Delta(dN/dh)$, an extra $\Delta\phi = 72°$ is measured at S-band for targets that are separated by $\Delta H = 10$ m and $\Delta D = 1$ km. The extra $\Delta\phi$ consequently causes a 10 N-units bias locally. This large bias reflects how strongly height differences between targets affect the local N bias (noisy $\Delta\phi$) when dN/dh changes. This is a serious concern because it is common to have targets or terrain of varying heights along any given azimuth.

Local N bias due to the propagation effect

The evolving propagation condition (dN/dh) affects the path length variation and the changing beam curvature relative to the Earth's curvature, as terms (iv) and (v) shown in (2.9), respectively. Hence, this local N bias depends on Δr_2 and dN/dh_{ref}. Figures 2.3b and c show the similar relationship of local N bias associated with different dN/dh_{ref}, -157 and -40 km^{-1}, respectively. Figure 2.3b shows that this local refractivity bias is of the order of -1 N-unit in the case of two targets 1 km apart at 20 km with $\Delta(dN/dh) =$ 150 km^{-1}. The local N bias among nearby target pairs is higher compared with the previously-discussed averaged bias along the beam path (Fig. 2.2b). This is because the amplification introduced by the computation of range derivatives of $\Delta\phi$ results in larger ΔN bias.

Consequences

The biases discussed above show how the data quality of retrieved refractivity is strongly affected by the diurnal evolving dN/dh. On the other hand, the temporal phase difference, say $\Delta\phi = \phi_{t+30min} - \phi_t$, is less noisy due to a smaller $\Delta(dN/dh)$ within a short time than the phase differences computed over several days. A 2-D ΔN map derived from $\Delta\phi$ in a short time period is useful to track the moving boundary of the thermodynamic variations. For quantitative applications, however, the N field is easier to interpret and directly related to Eq. (2.1). Thus, the problem of noisy $\Delta\phi$ observed when large change in dN/dh occurs cannot be entirely avoided.

In addition, the result of N estimation is very sensitive to the size of the smoothing window or of the $\Delta\phi$ regression computation to obtain the slope of ΔN. A small smoothing window with a limited number of targets causes larger uncertainty due to fewer constraints. If a small window containing noisy $\Delta\phi$ is selected, the ΔN computed will have a radial wavy pattern and the resulting bias of ΔN easily becomes larger. On the contrary, if the smoothing window is too large, the small spatial structure of N is smoothed out. The bias of ΔN is roughly proportional to $(\Delta D)^{-3/2}$ for two reasons; first, considering in the radial direction, the bias of ΔN is proportional to $(\Delta D)^{-1}$ shown in (2.9); second,

ΔN field is smoothed in azimuth, with the number of azimuths being proportional to ΔD, and the sampling bias of ΔN is proportional to $(\Delta D)^{-1/2}$. The smoothing window should be determined considering the variability of $\Delta\phi$, which is related to the variability of target heights, small-scale horizontal variation of N, azimuth alignments of targets and the number of targets available. The setup of the smoothing window and the representative spatial resolution of N estimates is a problem that deserves a more thorough study than can be done here.

Previous work uses smoothing to reduce the noisy $\Delta\phi$ between neighboring targets in order to obtain a reasonable refractivity field, only mitigating part of the problem. The goal of obtaining a refractivity map at a given known height requires accounting for biases due to propagation conditions and target heights. However, the lack of knowledge about dN/dh and H_T makes this problem challenging. Therefore, in the following section, an assessment of $\Delta(dN/dh)$ and H_T will be made by using the other radar measurements - power variations with elevation.

2.3 Extracting dN/dh information from returned power

2.3.1 Concept of a point-like target

Using the returned power (P) of a point target at multiple low antenna scanning elevations (θ) takes advantage of the radar antenna beam pattern. The linear antenna gain function can be approximated by a Gaussian shape (Probert-Jones, 1962). When the radar scans across a point target, the relative returned power at each antenna elevation, $P(\theta)$, with respect to the maximum power return (P_o) at the representative elevation (θ_o) should mimic the radar beam pattern such that:

$$\frac{P(\theta)}{P_o} = exp\left[\frac{-(\theta-\theta_o)^2}{2\sigma^2}\right]. \tag{2.10}$$

The standard deviation (σ) of the Gaussian distribution is related to the 6-dB antenna beamwidth equal to $2\sigma\sqrt{2ln4}$. The elevation θ_o is the one that results in the center of the main beam traveling from the radar to the given ground target. The received power changes at a rate that depends on the relative angle off the center of the main beam ($\theta - \theta_o$). Figure 2.4a illustrates that the observed reflectivity from a target at successive scanning elevations can be fitted with the known radar beam pattern. The θ_o associated with the target's position is consequently identified as the maximum returned power, which occurs at 0.14° for the target considered in Fig. 2.4a.

A point target can be identified by fitting the received powers at successive antenna elevations $P(\theta)$ with the radar beam pattern. This process is identical but reversed from past studies that used point targets to determine antenna properties (e.g., Rinehart and Tuttle, 1981; Rinehart and Frush, 1983). However, direct interpretation of returned power is complicated due to the unknown size, number, position, etc. of ground target(s) within a resolved volume. Thus, targets with $P(\theta)$ similar to the antenna pattern only indicate their 'point-like' behavior, as opposed to more complex patterns that would be expected from extended targets.

A simpler method is further proposed to effectively investigate the point-like property of targets based on the parabolic shape of $P(\theta)$ on a logarithmic scale. The first order derivative of the logarithmic $P(\theta)$ function within the main beam is linear with a constant slope determined by the antenna beam width (Fig. 2.4b). The power difference between two elevation angles decreases linearly with averaged antenna elevations. Meanwhile, this linear fitting method can be used to determine the elevation θ_o where the power difference is zero. Note that 1) the linear approximation is valid only in the main lobe, and 2) any deviation from the expected slope in the main beam indicates that targets are either point targets with saturated power or they are not point-like targets.

2.3.2 Using echo power at multiple elevations

How can the power measurements of point-like targets be applied to retrieve further information for improving refractivity retrieval? The representative elevation θ_o links the observed power and the behavior of the beam path from the radar to the target under a particular atmospheric propagation condition. It is a function of the location of the

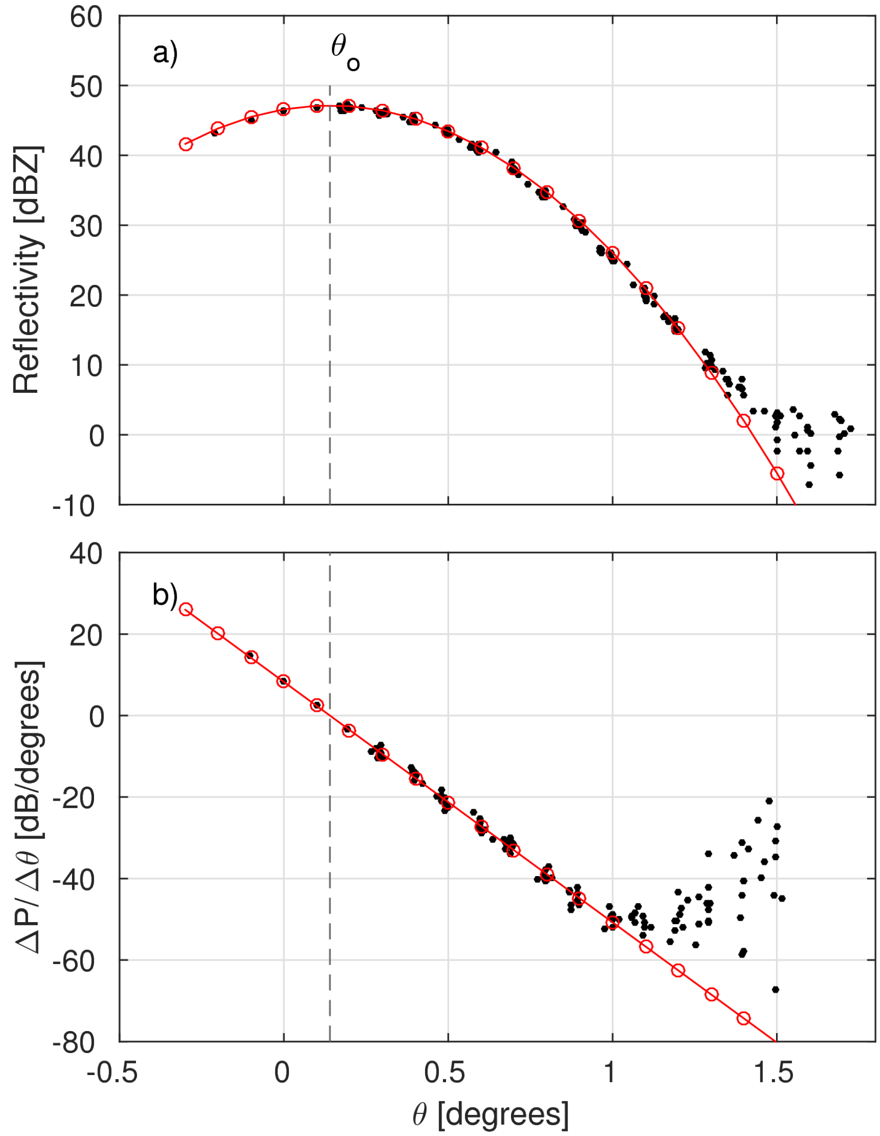

Figure 2.4 – (a) Power pattern of a selected ground target as a function of antenna elevation. The target is located at the 240° azimuth and the 228^{th} gate. Black dots show the reflectivity measured at multiple antenna elevations. These measurements are fitted with a Gaussian function of the width of the antenna beam (red line with circles). The noisy reflectivity near $\theta = 1.5°$ is due to the null of the antenna. This particular example was chosen because it is a rare case where the center of the main beam is observed; for most targets, only one side of the main lobe is observed. (b) First order derivative of the reflectivity pattern in (a) with respect to elevation θ showing the linearity of $\Delta P/\Delta\theta$ with θ. The red line illustrates the results of a linear regression through the data assuming a slope derived from the Gaussian antenna beam pattern as in (a).

targets (D, H_T) and the vertical gradient of refractivity (dN/dh):

$$\theta_o(D, H_T, \frac{dN}{dh}) = \tan^{-1}\left\{\frac{1}{\sin(\frac{D}{a_e})} \times \left[\cos\left(\frac{D}{a_e}\right) - \frac{a_e}{H_T + a_e - H_R}\right]\right\}, \tag{2.11}$$

where $a_e = a/[1 + \frac{a}{10^6}(\frac{dN}{dh})]$ is the effective Earth's radius associated with a given dN/dh.

Figure 2.5a shows the varying θ_o of targets at different D and H_T under a series of dN/dh conditions. For a given point-like target, θ_o decreases with increasing dN/dh. At closer range, θ_o is more sensitive to differences in H_T, changes in θ_o caused by varying dN/dh being small compared to those associated with varying heights. But at further ranges, θ_o is more sensitive to changes in dN/dh. Furthermore, the variation of θ_o at given $\Delta(dN/dh)$ depends only on D, but not on H_T. Hence, Fig. 2.5b shows the change of θ_o as a function of $\Delta(dN/dh)$ and D and illustrates that θ_o changes more at greater distances. Although θ_o provides constraints on H_T and dN/dh, it is still an underdetermined problem. Are there any glimmers of hope to estimate these two variables or at least one of them?

Estimating H_T

Based on the concept of the radar beam height equation in Doviak and Zrnic (1993), the power-weighted height of a point target can be estimated as:

$$H_T = a_e\left[\frac{\cos(\theta_o)}{\cos(\theta_o + \frac{D}{a_e})} - 1\right]. \tag{2.12}$$

H_T can be obtained with known D and observed θ_o, but dN/dh and a_e are still unknown. The dN/dh is more predictable in a well-mixed lower boundary layer during the afternoon, and it is expected to be between -40 and -20 km^{-1}. For example, by using (2.12), if targets are located at 20 and 40 km from the radar respectively, a 10 km^{-1} uncertainty of dN/dh would lead to a 2 m and 8 m error in H_T and a 0.01° observation bias in θ_o causes a 3.5 m and 7 m error in H_T. Thus, the estimation of H_T will have higher uncertainty at farther distances. A very accurate θ_o to a hundredth of a degree is required

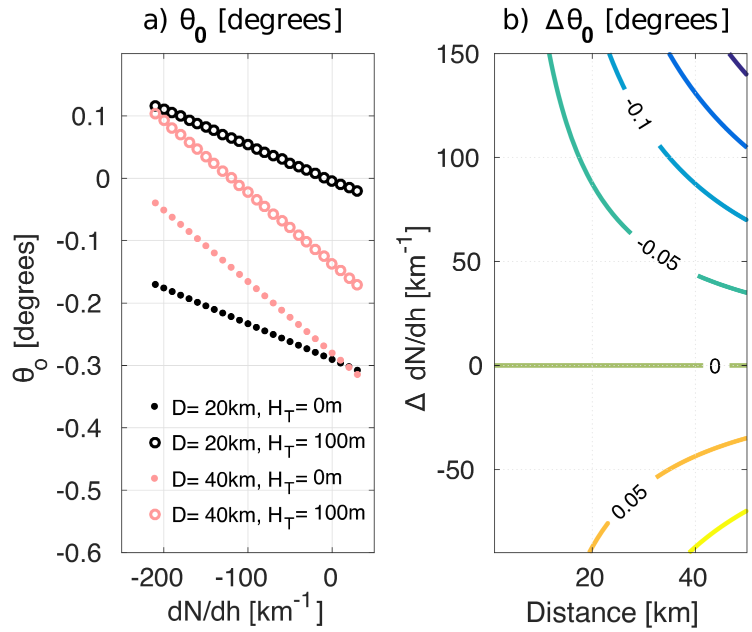

Figure 2.5 – (a) Representative elevation θ_o (in degrees) of ground targets at different distance D and height H_T as a function of dN/dh conditions. At closer ranges, θ_o is more sensitive to differences in target heights; at further ranges, it decreases more with changes in dN/dh. (b) Variation of the representative elevation $\Delta\theta_o$ as a function of D and $\Delta(dN/dh)$.

for height estimation. In reality, there are only a few targets for which this method can be used because the returned powers of most targets at lower elevations and close range are saturated, leading to wrong θ_o estimates.

Estimating dN/dh

If H_T can be determined well enough, dN/dh may be obtained from the temporal variation of θ_o of selected targets based on (2.11). Although H_T is unknown, it can be estimated with reasonable accuracy by using terrain height and adding an estimated average height above the terrain. In rural areas, most of the ground targets are usually at few meters above the terrain. Experience suggests that the mean and the standard deviation of target heights above the terrain is about 10 m (Park and Fabry, 2010) and maybe twice that in urban areas away from downtown cores. Therefore, terrain provides useful information to approximate the relative H_T variation among ground targets. Moreover, a sensitivity test of uncertainty of H_T and θ_o on dN/dh estimation is examined based on (2.11) and (2.12).

A 10 m uncertainty on H_T causes a dN/dh estimation error of 12.5 km^{-1} at 40 km but a 50.6 km^{-1} error at 20 km in range. A 0.01 degree uncertainty in θ_o results in 17.5 and 8.7 km^{-1} error in dN/dh estimation for a target at 20 and 40 km, respectively. High accuracy of observed θ_o is still required. Targets at far ranges remaining well within the main lobe of the antenna under all propagation conditions are hence optimal for estimating dN/dh because more variation of θ_o occurs at far range than at close range for the same $\Delta(dN/dh)$ (Fig. 2.5a).

Normalized dN/dh from $P(\theta_2) - P(\theta_1)$:

For operational radars, it is not practical to execute many low elevation scans to obtain θ_o for dN/dh estimation. Hence, an alternative algorithm using only two low elevations is developed. The θ_o of a point-like ground target in the main lobe can be estimated from the observed power difference in dB at two elevations, $\Delta P = P(\theta_2) - P(\theta_1)$ given $\theta_2 > \theta_1$, as:

$$\theta_o = \frac{2\sigma^2 ln10^{\frac{\Delta P}{10}} + {\theta_2}^2 - {\theta_1}^2}{2(\theta_2 - \theta_1)}. \tag{2.13}$$

For a given point-like target, θ_o decreases linearly with increasing dN/dh (Fig. 2.5a). Based on the linearity of the first order derivative of $P(\theta)$, ΔP changes linearly with θ_o as well as dN/dh. Thus, ΔP can be used to retrieve dN/dh quantitatively.

Nevertheless, ΔP is not identical for different ground targets even under a given dN/dh as it also depends on H_T and D. An assumption of spatially constant dN/dh is made. For each target, the two extreme opposite ΔP are selected as references, $\Delta P_{dN/dh_{max}}$ and $\Delta P_{dN/dh_{min}}$ occurring at the maximum and the minimum dN/dh during a time period of few days. Thus, the relative dN/dh change among targets during that time period can be normalized as:

$$\frac{\frac{dN}{dh} - \frac{dN}{dh}_{max}}{\frac{dN}{dh}_{min} - \frac{dN}{dh}_{max}} = \frac{\Delta P - \Delta P_{dN/dh_{max}}}{\Delta P_{dN/dh_{min}} - \Delta P_{dN/dh_{max}}}. \tag{2.14}$$

The normalized dN/dh can be estimated by the power difference between the two lowest elevations of surveillance scans for operational radars. Consequently, by combining with the two different dN/dh values obtained from the calibration scans, the dN/dh value in real time can be readily available. Given that (2.9) uses true dN/dh, the temporal qualitative variation of normalized dN/dh derived from (2.14) still provides valuable information as a quick quality check index of retrieved refractivity associated with dN/dh.

2.4 Validation of dN/dh retrievals

2.4.1 Data

The new method of dN/dh estimation is applied to the National Center for Atmospheric Research (NCAR) S-band radar (S-Pol) in Colorado, United States. The estimated dN/dh by the radar is compared with the in-situ observation from the Boulder Atmospheric Observatory (BAO) tower close to the S-Pol radar (Fig. 2.6). The center of the antenna of the S-Pol radar is about 12 m above the ground and the antenna beamwidth is 0.92°. Two special scanning strategies were conducted in this experiment. The first was to obtain the properties of ground targets and to select suitable point-like targets. Successive low elevation scans from $-0.2°$ to 2° in 0.1° intervals were collected on a clear windy afternoon from 1907 to 2242 UTC on 27 January 2015. The second stage aimed to capture the signal of diurnal dN/dh variation lasting for a few clear days from 2137 UTC on 20 March to 1427 UTC on 23 March 2015. Scans at the following six elevations were collected: 0°, 0.4°, 0.6°, 0.8°, 1.0°, and 1.2°.

Ground targets are first distinguished from weather or other signals using the following criteria: The average returned power at 0.3° and 0.6° elevations during the first experiment are higher than 25 dBZ, and the standard deviation of the power at each elevation over the four hours of the first data experiment is less than 1.5 dB to ensure the stability of power returns; average clutter phase alignment (CPA, Hubbert et al., 2009) is higher than 0.85 and its standard deviation is smaller than 0.03. High CPA implies that phase and power are consistent within the resolved volume. In addition, the point-like nature of the target is checked by fitting a line through the first order derivative of $P(\theta)$ within the

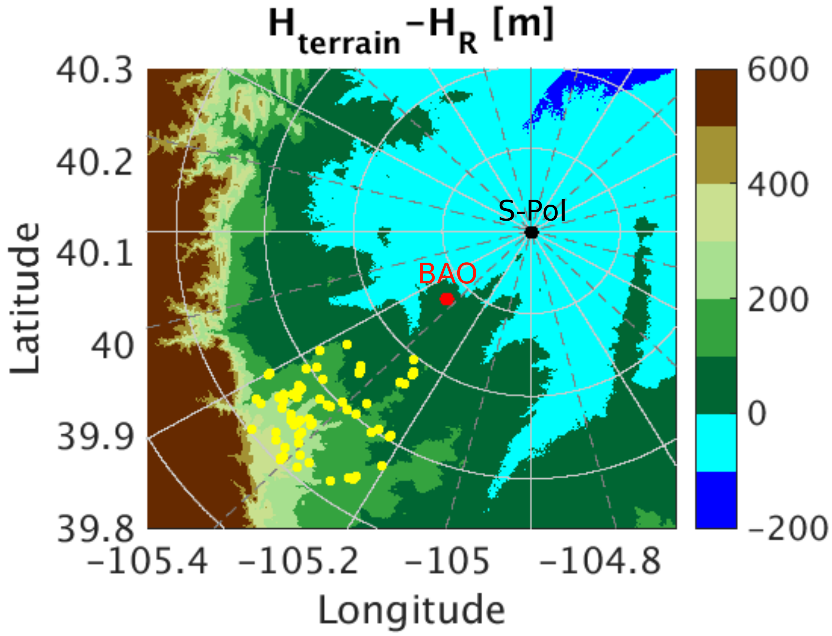

Figure 2.6 – Map of height difference (m) between the terrain and the S-Pol radar (located in the center of the range rings). The gray lines show the azimuth angles at 30° intervals relative to the S-Pol radar, and the rings are in 10 km range interval away from the radar. The BAO tower is shown as a red dot at 229.5° in azimuth and 12.56 km away from the radar. The yellow dots are the selected ground targets for dN/dh estimation.

main beam and comparing it with the slope expected from the antenna beam pattern: The slope associated with the S-Pol radar antenna is -56.9 ($dB/degree^2$), and the slope of the targets should be within the range $-56.9\pm$ 3 ($dB/degree^2$) to be declared point-like. The number of ground targets in the selected area (210° to 240° in azimuth, 20 to 40 km) meeting the criteria of having stable power returns is 315, 75 of those further meeting the point-like target criteria. The final selected point-like targets are generally at elevations less than 300 m above the radar (Fig. 2.6).

The BAO tower collects near-surface atmospheric basic variables; temperature, relative humidity and wind every minute at 10, 100, and 300 meters height above the ground. Only surface pressure is measured, and the pressure at other elevations is derived from the hydrostatic equation. The refractivity value at each level is calculated based on (2.1). The vertical profile of refractivity between different heights is obtained as an in-situ observation for comparison. The BAO tower is maintained by the Physical Sciences Division of National Oceanic and Atmospheric Administration (NOAA). Data were downloaded from http://www.esrl.noaa.gov/psd/technology/bao/.

2.4.2 dN/dh estimation from selected targets

An example of a selected point-like target illustrates how to use echo powers to estimate dN/dh (Figs. 2.7 and 2.8). Figure 2.7 shows the variation of $P(\theta)$ and first derivative of $P(\theta)$ for nearly three days in the second experiment. As dN/dh becomes more negative, the patterns of $P(\theta)$ and θ_o shift to a higher elevation. This occurs because the beam path at a given antenna elevation θ bends more toward the ground under super-refraction conditions; thus, it requires a beam with a higher θ_o than under normal propagation conditions to reach the target. The time series of $P(\theta)$, ΔP, and θ_o (Figs. 2.8 a-c) show similar diurnal variations; decreasing in the day but increasing during the night. A sudden drop of θ_o in the nighttime (28-35th hour) occurs due to a frontal passage (Fig. 2.8c). Finally, ΔP can be normalized between 0 and 1 corresponding to the minimum and maximum of dN/dh during this time period (Fig. 2.8d). The observed returned reflectivity, ΔP and θ_o are all negatively correlated with dN/dh. The relative dN/dh physically represents the near-surface mixing conditions, relatively higher dN/dh occuring during daytime due to well-mixed boundary layer. In addition, this normalized dN/dh helps quickly integrate the $\Delta(dN/dh)$ from many selected targets at different heights and distance even though their ΔP and θ_o are different.

An ensemble of ground targets is used to estimate an average dN/dh. Finding more than one point-like target increases confidence in the dN/dh estimation, because it might reduce the uncertainties in guessing of H_T and biasing estimated θ_o. Figure 2.9a illustrates the similar diurnal trend of θ_o among selected targets. The different magnitudes of θ_o are due to the different distances and heights of individual ground targets. Based on the linear relationship between θ_o and dN/dh, the average observed θ_o from an ensemble of targets, $\overline{\theta_{oTargets}}$, is able to represent the average dN/dh. Then, $\overline{\theta_o}(dN/dh)_{guess}$, the average θ_o from the selected targets under a wide range of dN/dh conditions, is calculated based on (2.11). The target heights here are approximated as the terrain height plus an assumed

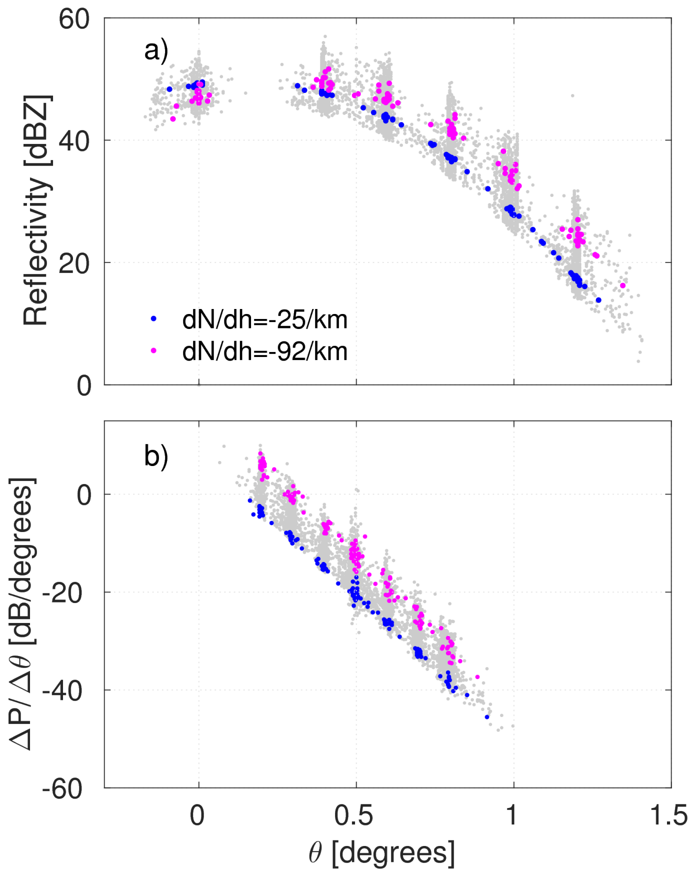

Figure 2.7 – Returned power variation of the selected target of Fig. 2.4 for three days. (a) Reflectivity observed at multiple radar elevations under a variety of conditions (gray dots). The colored dots highlight two specific dN/dh conditions; one in normal condition ($dN/dh = -25$ km^{-1}, in blue), one in super-refraction condition ($dN/dh = -92$ km^{-1}, in magenta). (b) First order derivative of power versus antenna elevation. Colored dots are as in (a).

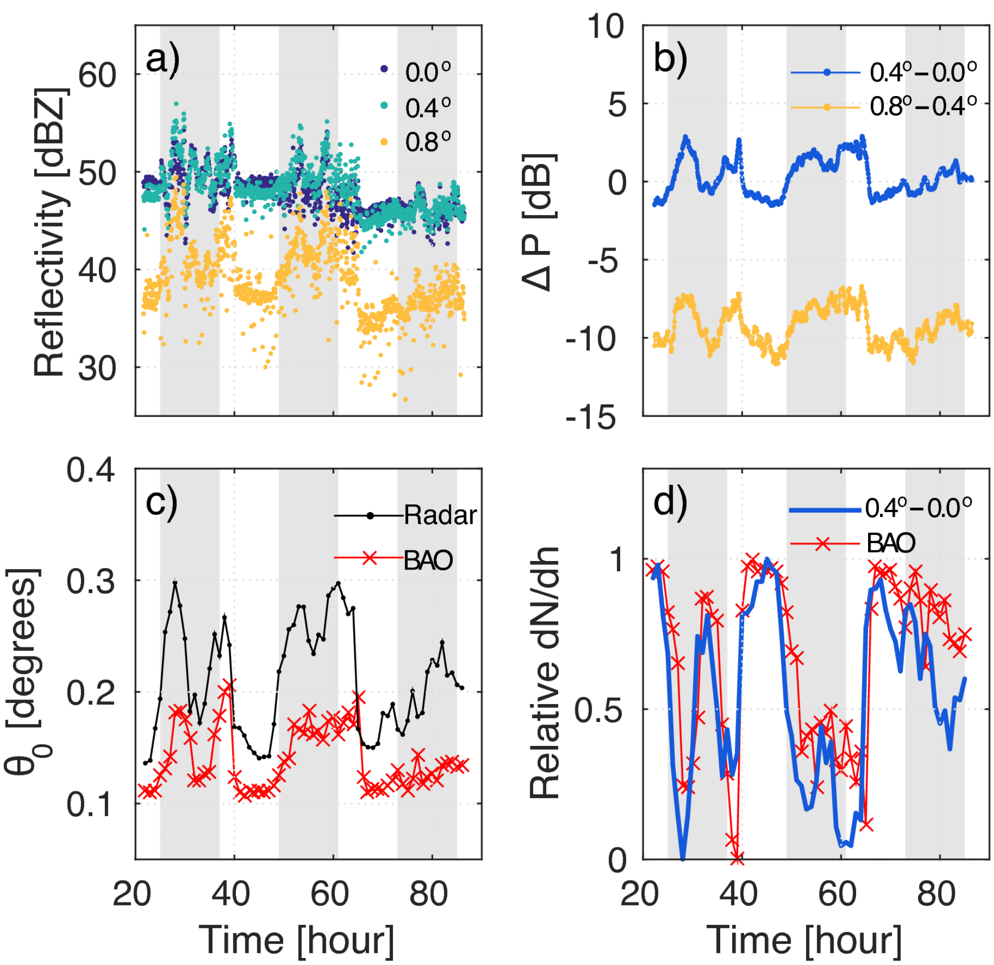

Figure 2.8 – Illustrations of how dN/dh is retrieved for the target selected in Fig. 2.4. (a) Temporal series of power returned in dBZ from the target for the radar antenna elevation angles at 0°, 0.4° and 0.8°. The gray shading indicates the night time after sunset until the next sunrise. (b) Power difference ΔP between two elevations in time smoothed using a one-hour running average. The blue line shows $\Delta P_1 = P_{0.4^o} - P_{0.0^o}$ and the yellow line is $\Delta P_2 = P_{0.8^o} - P_{0.4^o}$.(c) Representative target-center elevation θ_o obtained from the radar and the BAO tower based on Eqs. (2.13) and (2.11), respectively. (d) Normalized dN/dh in this experiment period ranging between one (the maximum dN/dh) and zero (the minimum dN/dh). The blue line is derived from ΔP_1, while the red line shows the normalized dN/dh between 10- and 100-m derived using data from the BAO tower.

target height of 10 m above the surface, i.e., $H_{Tguess} = H_{terrain} + 10$ m. The estimated dN/dh from the radar and targets, dN/dh_{Radar}, is determined from the minimum absolute difference between $\overline{\theta_o}_{Targets}$ and $\overline{\theta_o}(dN/dh)_{guess}$. Note that a mean bias in target heights of 5 m in this case will lead to a relatively small dN/dh estimation bias of 5 to 10 km^{-1}.

2.4.3 Radar - tower comparison of dN/dh

The estimated dN/dh_{Radar} is consistent with the dN/dh measurement between 10 and 100 m of the BAO tower (Fig. 2.9b), although there is a difference of dN/dh in magnitude between these two datasets. The correlation coefficient between the estimated and observed dN/dh is above 0.8 (Fig. 2.10). Moreover, there is a correlation coefficient greater than 0.9 between dN/dh from the BAO tower and relative dN/dh derived from ΔP for any combination of antenna elevation angles within the antenna main beam.

The discrepancy of dN/dh estimation between the radar estimation and the BAO tower requires further discussions. The first point to consider is the data quality of measured power of targets. The power of a ground target at a given elevation usually fluctuates (Fig. 2.8a), which produces noisier ΔP and more uncertainties in θ_o. Fluctuations in returned power of ground targets occur due to a variety of causes from scintillation to slight changes in target shape. Then, the atmosphere is not horizontally homogeneous. Furthermore, some radars might have a position pointing bias and the accuracy of the reading of the antenna elevations needs to be considered. Though the difference in elevation might be small, it can lead to a large difference in the power considering the parabolic shape of the antenna pattern and it may lower the accuracy of θ_o estimations to which dN/dh estimations are sensitive. Here, the average difference θ_o between the radar estimation and the known dN/dh from the BAO tower is calculated to estimate the bias in antenna elevation reporting. This calculation suggests a pointing bias of approximated 0.03° that can be used to obtain a new corrected dN/dh (light blue line in Fig. 2.9b) that better matches observations, particularly in the day time with well-mixing boundary layer (i.e. dN/dh closer to 0). But overall, the diurnal trend still dominates and can be retrieved despite all other sources of power fluctuations.

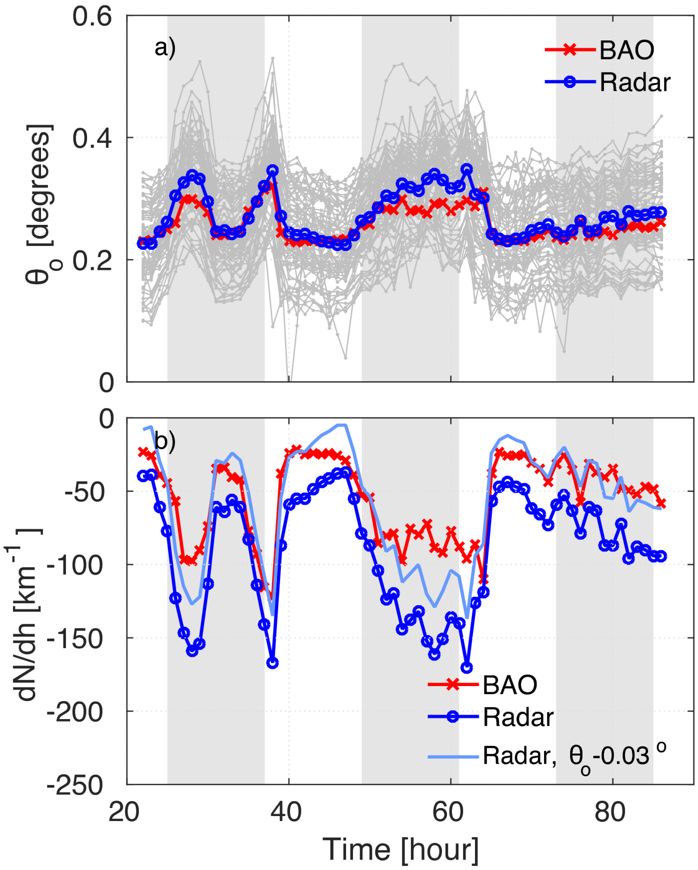

Figure 2.9 – (a) Time series of θ_o from the selected point-like targets shown in gray lines. The blue line with circles is the hourly average θ_o among ground targets. The red line with crosses is the average θ_o calculated based on the dN/dh from the BAO tower as well as D and H_T of selected targets. The gray shaded periods represent the night time as mentioned in Fig. 2.8. (b) Time evolution of dN/dh of the BAO tower (red line) and of the radar estimation (blue line with circles). The light blue line shows the corrected radar estimation dN/dh considering a 0.03° pointing angle correction of the antenna.

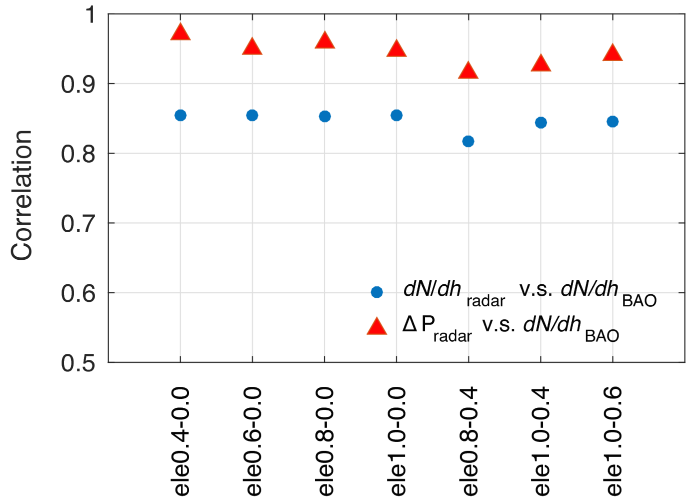

Figure 2.10 – Correlation coefficients between the time series of dN/dh estimated from the BAO tower and derived from power differences at given antenna elevations of S-Pol (blue dots). Red triangles show the correlation between the relative dN/dh of S-Pol and of the BAO tower.

In addition, differences in measurement representativeness might explain the discrepancies in dN/dh. The BAO tower is a single point observation, but the estimation from ground targets is the averaged result of a nearby area. Furthermore, the representative heights are different: the dN/dh from the BAO tower is the refractivity difference between 10 and 100 m above the ground but the dN/dh radar estimates are much closer to the ground (i.e. both the heights of the radar and ideal point-like ground targets used here are about 10 m height above the ground). In particular, the large nighttime negative dN/dh might appear earlier and be stronger in layers close to the ground than in the higher tower observations, due to the gradual buildup of the inversion. Furthermore, dN/dh has more variability at night as previously shown by in-situ observation or radar estimations (Fig. 2.9).

Finally, the power of a given pixel is not only affected by the beam propagation condition (dN/dh) but also by some partial beam blockage by ground obstacles in front of the targets and the complexity (number, combination) of the ground targets within the resolved volume. In addition, interference between different elements of a complex target could be mainly destructive under some dN/dh conditions, leading to an unexpectedly decreasing returned power during super refraction or ducting conditions.

In summary, power measurements at successive low elevations can be used to qualitatively describe the diurnal dN/dh variation which is key to improving refractivity retrieval based on (2.9). Moreover, the promising result of dN/dh estimation might be applied to operational radars and provide real-time information on near-surface beam propagation conditions, which affects the data quality of quantitative precipitation estimation, ground clutter elimination, and other applications.

2.5 Concluding remarks

Variable target heights and changing dN/dh affect and bias refractivity retrievals obtained by radar: first, targets are at different heights, and their information is harder to combine; then, propagation changes, as a result of which the trajectory of the radar beam to the target changes, along with refractivity sampled along the way. To mitigate these issues, we must seek to retrieve a map of refractivity at a constant height above terrain. Achieving this requires first obtaining a 2-D refractivity map at the height of the radar and combining it with an altitude correction that depends on target heights and dN/dh. Enabling this vision forced us to rethink about the information that can be obtained by radar for each target.

Using a theoretical reanalysis of the equation of the returned phase of a target, the representativeness of the measured phase and of the retrieved refractivity are clarified, and the systematic refractivity biases are quantified and shown to be related to the effect of H_T and of the changing trajectory with changes in dN/dh. Temporal biases of N over the whole domain may arise as a result of the evolving dN/dh associated with the near-surface layer mixing conditions; biases of refractivity over very short path lengths occur due to the variability of heights of ground targets. Taking these biases and errors into account can also help reduce the noisiness of phase measurements and also help mitigate the $\Delta\phi$ unfolding problem. Despite these improvements, some noise in the $\Delta\phi$ field remains due to unknown target heights and the intrinsic complexity of ground targets. As a result, it is still necessary to smooth or do regression on the corrected $\Delta\phi$ field with a reasonable window in order to estimate the gradient of $\Delta\phi$ and the small scale refractivity variations.

A practical method to estimate dN/dh and H_T is then proposed. It is based on the concept that the power returned by a point-target at successive antenna elevations can be described by the antenna beam pattern. Since both the power and phase of a stationary target record the evolving atmospheric conditions that the radar beam travels through, the difference in returned power at two given elevations and the elevation of peak power of selected point-like targets evolve linearly with dN/dh. An ensemble of point-like targets is used to estimate an average dN/dh, which shows promising and consistent trends when compared with the in-situ observation of the BAO tower. dN/dh information might be obtained from numerical weather model output or in-situ tower observation. However, there are often quantitative differences in dN/dh between model output and in-situ data that might be related to uncertainties in boundary layer processes in model simulations. In-situ tower observations are helpful, but they are not readily available for most radar sites. Hence, the new method of dN/dh estimation is encouraged to be applied to operational radars. Furthermore, a theoretical method to estimate the power-weighted height of the target is developed, but there are some practical problems in obtaining the H_T of all ground targets. Although the height of most targets remains unknown and challenging to obtain, terrain can be used as a useful proxy to describe the height difference between targets. In addition, the assigned height above the terrain should be set reasonably and consider the practical conditions of target heights; here, 10 m above the terrain is used for rural areas.

Using this new theoretical basis, the magnitude of systematic biases in refractivity retrievals can be reduced by including the effects of terrain and target height. To make this possible, a new step-by-step processing to retrieve N based on these results should be as follows: 1) determine H_T based on the terrain; 2) measure N_{ref} and $(dN/dh)_{ref}$ in known N and dN/dh conditions; 3) in real time, use echo power at different elevations to determine dN/dh; and, 4) use (2.9) to retrieve N at a desired altitude.

Acknowledgement

The authors thank Dr. Mike Dixon for helping to collect special scans with the NCAR S-Pol radar. We also used in-situ BAO observation provided by the NOAA/OAR/ESRL PSD, Boulder, Colorado, USA, from their Web site at http://www.esrl.noaa.gov/psd/technology/bao/ and thank NOAA for its generosity. We also thank Dr. Isztar Zawadzki for many fruitful discussions and Mr. Jonathan Vogel for English correction. This work was made possible thanks to the support from the Natural Science and Engineering Research Council of Canada (NSERC). The National Center for Atmospheric Research is sponsored by the National Science Foundation.

Chapter 3

The imperfect phase pattern of real parabolic radar antenna and data quality

In the previous chapter, power returned from point-like targets at multiple antenna scanning elevations are applied to estimate the vertical refractivity profile based on the antenna power pattern. In the process, we found the phase differences between multiple elevation angles to have unexpected behavior. This pushed us to study the phase pattern of parabolic radar antenna by analyzing the phase measurements from point-like targets using high-resolution elevation scans. In this chapter, the phase pattern of our radar antenna is characterized and its impacts on radar data quality are investigated.

The manuscript that constitutes this chapter was published as Feng, Y. and F. Fabry, 2016: The Imperfect Phase Pattern of Real Parabolic Radar Antenna and Data Quality. J. Atmos. Oceanic Technol., 33, 2655–2661, doi: 10.1175/JTECH-D-16-0143.1.

The imperfect phase pattern of real parabolic radar antenna and data quality

Ya-Chien Feng and Frédéric Fabry

Department of Atmospheric and Oceanic Sciences, McGill University, Montreal, Quebec, Canada

Abstract

Though antennas have well-known power patterns that are commonly used to understand the quality of measurements, they also have phase patterns that are difficult to obtain and seldom discussed in the radar meteorological community. This study presents the characteristics of the antenna phase pattern of the McGill S-band radar. Phase variations in azimuth and elevation with respect to the main beam axis are obtained using high-resolution scans of an isolated ground target and of an emission source. The two-way phase pattern is relatively constant within the radar main beam, but changes rapidly at the power minimum between the main beam and the first sidelobe. The effects of this phase pattern on ground and weather targets were evaluated and found to be much more pronounced for point than for distributed targets. Nevertheless, proper knowledge of the phase pattern of the radar antenna would enhance our abilities to better select ground targets for radar refractivity retrieval and to estimate the quality of radar data.

3.1 Introduction

Radar antennas play an important role in the quality of radar measurements, and characterizing them is hence required. Generally, the classic power pattern of the radar antenna is readily available for most radars and has been used to evaluate data quality. Antenna differential phase patterns have been measured and simulated particularly for analyzing the quality of dual-polarization measurements (Chandrasekar and Keeler, 1993; Mudukutore et al., 1995; Hubbert et al., 2010a; Moisseev et al., 2010; Myagkov et al., 2015). However, absolute antenna phase patterns of operating weather radars are seldom discussed because there are challenges to directly measure it in the far field and there is no obvious motivation to do so.

To understand why antennas have phase and power patterns requires reflecting on how antenna function in principle. The energy source from the feed horn illuminates a parabolic reflector that focuses the energy into a narrow conical beam because of the constructive and destructive interference of the reflecting waves. The geometry of parabolic antenna as a reflector makes waves as plane waves within the main lobe in the far field from the radar, where the phase surfaces are theoretically constant at given range from the center of the reflector; then, there is a pronounced one-way π phase shift between the main beam and the first sidelobe as contributions to the beam pattern from the sides of the rotating antenna become in phase and dominate those from the center of the antenna. In real physical antennas though, phases shift differently than for perfect antennas.

This exploration of the absolute antenna phase pattern originally began as part of an effort to measure the phase returned from fixed ground targets that are used for retrieving the near surface refractivity of air. Temporal phase variations of a stationary ground target occur as a result of changes in the refractivity along the radar beam path (Fabry et al., 1997). One problem of this technique is the aliasing of temporal phase change resulting in biases of refractivity estimations. To overcome this problem, Besson and Parent du Châtelet (2013) suggested to collect returned phases at more than one elevation in order to increase the temporal resolution and mitigate the phase aliasing problem. But, we were uncertain whether the phase measured from a target (less than) one degree away from the beam center is the same as that measured at the center of the beam. In other words, information on the antenna phase pattern is required to describe the phase added by the antenna to targets located away from the antenna axis. This need prompted us to study the rarely investigated absolute phase pattern of weather radar antenna.

Measuring the antenna phase pattern in the far field is challenging as it requires an external emission source of superb phase stability. Thus, the far field radiation pattern is usually obtained by the Fourier transform of the aperture field distribution. In the absence of detailed information on the aperture field distribution, we were forced to measure the phase pattern of our radar indirectly.

3.2 The phase pattern of the McGill parabolic radar antenna

3.2.1 Revealed by scanning a point-like target

The antenna power pattern can be obtained by multiple ways; one of them involves scanning a point-like ground target (Rinehart and Tuttle, 1981), such as an isolated stationary tower whose echo does not scintillate and has a relatively small angular extent compared with the main lobe. When the antenna points directly at the ground target, the peak return power is observed. Away from the antenna center axis, received power decreases in the main lobe of the antenna as a function of azimuth and elevation following a generally Gaussian function in linear units: the result is a convolution of a point target with the original antenna gain pattern. The same process can be used to study the antenna phase pattern.

In this experiment, the McGill S-band radar scanned an isolated communication tower and collected high resolution pulse-by-pulse in-phase (I) and quadrature (Q) data of successive plan position indictors (PPIs) scans at elevation angles from 0.3° to 2° with 0.1° interval from 2015 to 2105 UTC on January 25 2012. The characteristics of the McGill radar are shown in Table 3.1. This selected isolated communication tower is located at

27.5 km and the top of the tower is about 10 m below the radar antenna level. The vertical angular extent of this target is about 0.04°, approximately 5 % of the 0.8° antenna beamwidth at horizontal polarization. Since isolated ground targets are relatively small compared with the radar beamwidth and the range resolution, they can be treated as point-like targets.

Frequency	2.88 GHz
Transmitted power	300 kW
Pulse length	125 m
Pulse repetition frequency	1200 s^{-1}
Dynamic range of the receiver	90 dB
Antenna beamwidth	0.8 °
Antenna diameter	9.1 m
Antenna focal length	3.8 m
Antenna to rotating axis distance	1.65 m
Antenna rotation speed	6 r.p.m.

Table 3.1 – Characteristics of the McGill radar.

The power returned from a ground target as a function of antenna pointing angle generally follows the square of the one-way antenna power pattern because the same antenna is used on both transmission and reception and reciprocity applies. Figure 3.1 illustrates the high resolution two-way power pattern scanning the ground target, which is at 113.58° azimuth and −0.13° elevation.

The signal to noise ratio (SNR) of the maximum power return is about 83.5 dB and the power around the main beam axis shows the saturation of the receiver due to the strong return of the ground target. When the antenna points away from the target, the returned power gradually decreases. On our radar antenna, the sidelobes are asymmetric both in azimuth and elevation; there are clear power minima between the main lobe and the first sidelobe above and on the right-hand side. However, only the lower portion of the antenna pattern is obtained due to the limitation of our 1967-vintage radar antenna system that is incapable of pointing at low elevations.

The two-way phase pattern from a ground target is related to the power pattern and is also asymmetric in azimuth (Fig. 3.1). Note that the phase shown here is relative to the

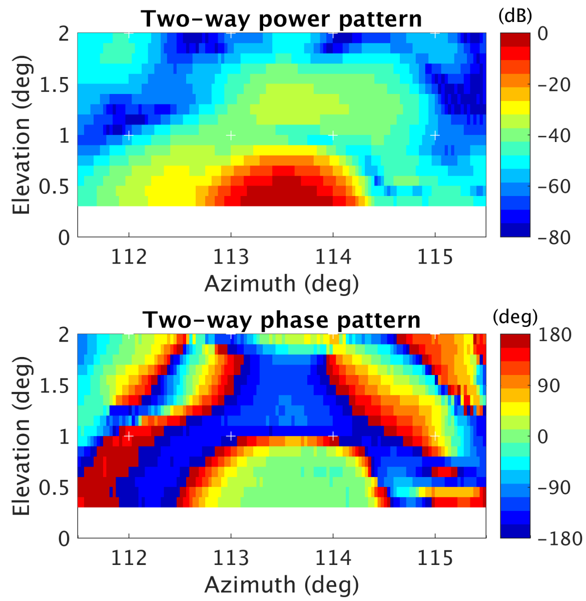

Figure 3.1 – The two-way patterns of the relative power (top, in dB normalized to its peak power at 0.3° elevation) and the relative phase (bottom, in degrees with respect to the phase of the peak power) of the parabolic antenna revealed from a communication tower. The signal to noise ratio (SNR) of the maximum power here is 83.5 dB. The tower is located at 113.58° in azimuth and -0.13° in elevation.

phase measurements of the peak echo power at the lowest 0.3° elevation, i.e. $\phi_{rel(azi,ele)} = \phi_{(azi,ele)} - \phi_{(azi:maxPower,ele:maxPower)}$, in order to display phase variation with respect to the beam axis and compare with other phase patterns. The phase remains nearly constant close to the center of the main beam, but changes gradually with the gradient of power away from the center of the beam axis, with the most rapid change occurring at the null. On our antenna, the two-way phase differences between the main lobe and the first sidelobe vary at different directions; they are about 210°, 310° and 260° on the left side, the right side and above the main beam, respectively. The phase of the first sidelobe varies quickly in azimuth instead of being nearly constant like for the main lobe. We further examined the phase patterns from other ground targets with unsaturated power and they showed consistent phase variation patterns as here.

3.2.2 Confirmed by receiving signals from a distant microwave source

To confirm measurements from ground targets, we conducted another antenna pattern measurement experiment using a microwave emission source in the far field. The details of this measurement process are discussed in the Appendix. Though the process of obtaining a phase pattern proved more difficult than we hoped, the results confirm that the two-way antenna phase patterns obtained from the corrected emission point source (Fig. 3.2) and from the communication tower (Fig. 3.1) are qualitatively similar; the two-way phases are both constant near the axis of the main beam, change gradually with the power gradient as the antenna points away from the beam center, and particularly shows the notable change at the power minimum between the mainlobe and the first sidelobe. The phase differences are about 270° between the main lobe and the first sidelobe on the right side and above, but are smaller on the left side (Fig. 3.2). The two-dimensional spatial correlation of these power patterns is above 0.9. The size of the ground target is larger than the point emission source, and the width of the power pattern of the main beam from the ground target is a little bit broader than that of the emission source. Even though there might be some concerns of using a possibly complicated ground target to obtain the antenna power and phase patterns, we gained confidence that isolated towers can be treated as point-like targets because the power and phase patterns obtained by the two approaches proved similar enough. The setups of these two experiments are not as ideal as measurements for a formal antenna test range; nevertheless, we still observed the qualitative characteristics of the phase pattern of the radar antenna.

The measured phase pattern revealed from these experiments are slightly different from the theoretical phase pattern of the parabolic antenna mentioned in Section 3.1. The observed two-way phase pattern shows gradual variation along with the power gradient on the edge of the main beam near the null, which is in contrast to the theoretical sharp phase change. The two-way phase difference between the main lobe and the first sidelobe is less than the expected 360°. These anomalies in phase and in power patterns might be explained by the imperfect geometry of antennas: the inaccurate positioning of the phase

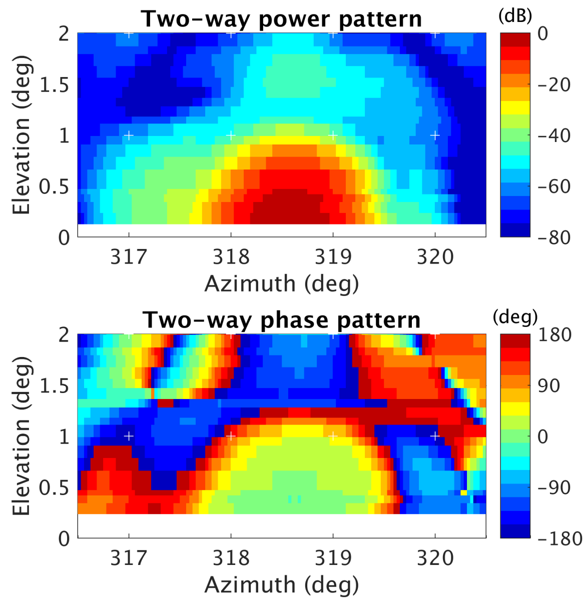

Figure 3.2 – Patterns of two-way relative power (top, in dB) and relative corrected phase (bottom, in degrees) of the antenna deduced from the emission source at 318.5° in azimuth. The relative power and phase patterns are with respect to the maximum power at the lowest scanning elevation, 0.3°.

center of the feed horn and the focal point of the parabolic reflector, the presence of struts, and irregularities in the shape of the reflector (Doviak and Zrnic, 1993; Mudukutore et al., 1995). Some small fluctuations of measured phase within the main beam may also be due to atmospheric scintillation.

3.3 Antenna phase pattern and data quality

Based on the characteristics of the observed antenna phase pattern, we investigated its impact on radar data quality.

3.3.1 Radar refractivity retrieval

The quality of the phase change of reliable fixed ground targets is key to retrieve accurate refractivity of the air. The profiles of power and phase show the clear signature of the variation of the antenna pattern in elevation (Fig. 3.3). Changes in the phase returned

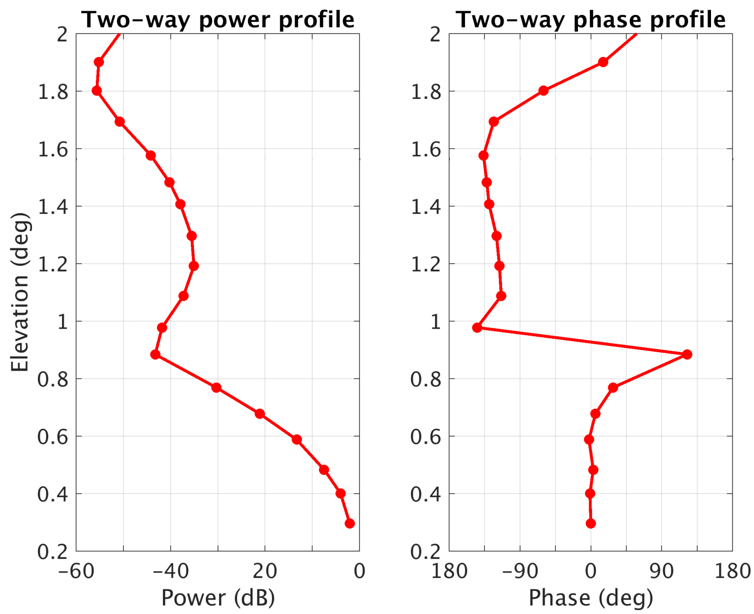

Figure 3.3 – Profiles of two-way power and phase calculated from 1° azimuth average centered on the azimuth of the ground target at 113.58° in Fig. 3.1. Thirty-two pulses are averaged for each beam.

from ground targets located close to the main beam axis are primarily caused by air refractivity change, and are not significantly affected by the antenna phase pattern, even when the electromagnetic wave propagation condition alters diurnally. If the observed ground targets are located close to an antenna null, i.e., with higher scanning elevations or for close-range targets, the phase added by the antenna changes significantly with wave propagation conditions, introducing biases in refractivity retrievals.

To properly use the phase at multiple elevations to increase the temporal resolution of radar refractivity retrieval as suggested by Besson and Parent du Châtelet (2013), we must be aware that the phase changes significantly with the antenna power gradient. Figure 3.4 presents a daily average phase difference between 0.3° and 0.5° elevations, illustrating the systematic bias of phase change for radar refractivity retrieval due to the antenna phase pattern. The phase differences in the areas of ground clutters (higher relative power values under a condition of clear weather, Fig. 3.4a) are mostly close to zero at far ranges since targets are illuminated in the main lobe. The greater value of the phase at higher elevation than at the lower elevation implies that the target is located near the bottom edge of the

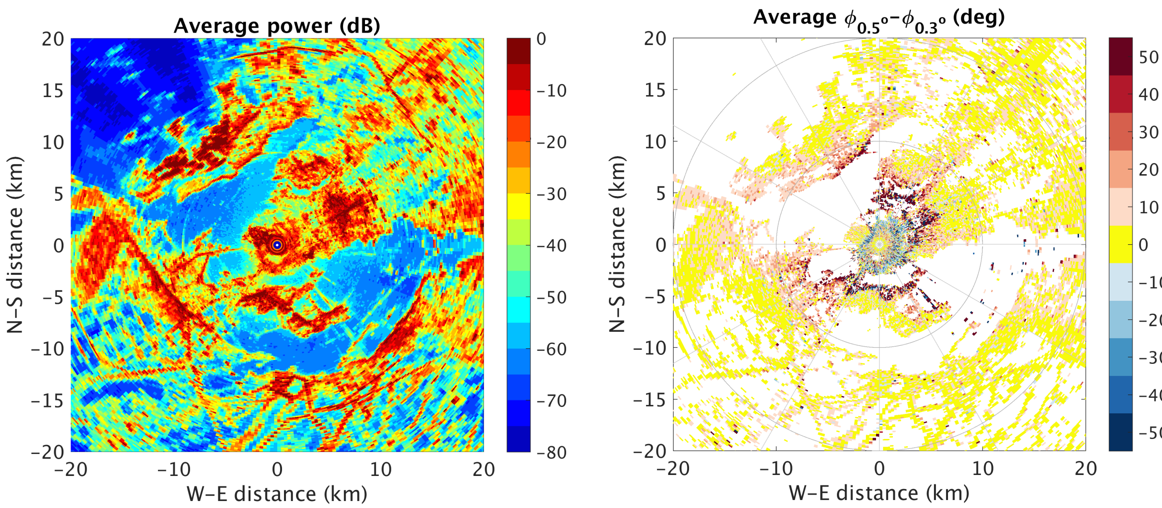

Figure 3.4 – (Left panel) Daily average two-way relative power at 0.3° elevation PPI on July 21 2012 under a clear weather condition, highlighting the location and strength of ground echo targets. The McGill radar is at the center of the figure. Ground clutters are shown in reddish colors. (Right panel) The daily average phase difference between 0.3° and 0.5° elevation scans for echoes with an average relative power greater than -40 dB. Rings of negative phase difference (2-3 km range) and positive phase difference (5-10 km range) can be observed; these occur because targets at these ranges are close to the antenna null, where a small difference of 0.2° in elevation leads to a large difference in the phase added by the antenna.

main lobe. A ring of negative values shown within 5 km radius of the radar coverage results from targets far below the main beam axis, probably in the first sidelobe. For most surveillance weather radars, the difference between the first two scanning elevation angles is usually more than the 0.2° shown here. Therefore, the phase pattern of parabolic antenna must be taken into account when combining multiple elevation angels to increase the temporal resolution of refractivity retrievals.

3.3.2 Ground clutter mitigation and radial velocity biases

The phase returned from point-like targets located in regions illuminated away from the antenna beam center changes notably in azimuth (Figs. 3.5 a,b). Thus, the width of Doppler velocity spectrum broadens with increasing azimuth and elevation away from the center of the main beam, and for the McGill antenna the Doppler spectrum becomes asymmetric with a non-zero mean velocity (Figs. 3.5 c-e). The velocity of the adjacent

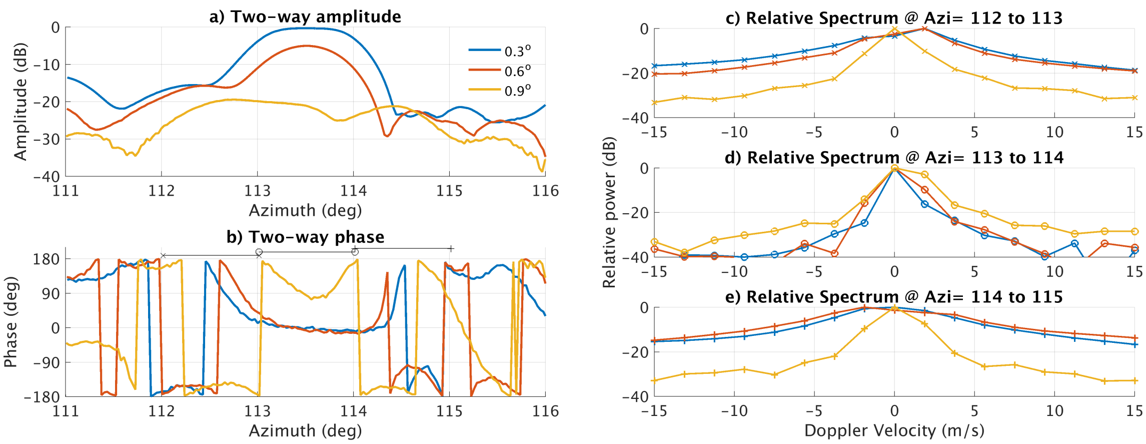

Figure 3.5 – Amplitude (a) and phase (b) of the echo from a dominant ground target as a function of azimuth at three elevations, 0.3°, 0.6°, and 0.9°. Note the receiver saturation at 0.3° scan. The relative Doppler spectrum (in dB) calculated from given 1° azimuth intervals (shown by different markers in (b)) are displayed in (c) to (e). All relative Doppler spectrum are normalized to their maximum power to ease comparisons.

beam 1° azimuth away from the stationary target is about 1 m s^{-1} for the McGill S-band radar. Note that the magnitude of the radial velocity bias on the edge of targets caused by the antenna phase pattern is larger than the effect of the antenna rotation speed (Rinehart, 1991): for the McGill radar, the bias of radial velocity at the adjacent beam 1° from the target axis introduced by the antenna rotation effect (given 6 revolutions per minute and a 5.45 m distance between the axis of rotation and the feed horn) is about 0.06 m s^{-1}. The change of the Doppler spectrum and the radial velocity at these adjacent beams with respect to a stationary ground target (the center of the main beam axis) can be explained by the varying phase added by the antenna phase pattern.

The characteristics of the antenna phase pattern revealed from a point-like ground target might be helpful to improve clutter filtering techniques, that generally assume a symmetric fixed-shaped (Gaussian width) clutter spectrum. Some new sophisticated method might be developed based on the antenna phase pattern, particularly for ground targets close to the edge of the main beam or near the null with non-zero velocities. For example, since the spectrum of the clutter is wider when scanned by the edge of the beam, it suggests that clutter filtering at higher elevation should use broader filters than at very low elevation. Besides, the complicated returned signal from multiple targets within a sampled volume or from adjacent beams can be also examined by integrating the individual power and phase patterns of targets at given positions. Dual-polarization data affected by ground targets (Friedrich et al., 2009) can be further quantitatively studied.

We also investigated the effects of the antenna phase pattern on the radial velocity estimation of a cloud/precipitation system and can make some general comments. The 2-D convolution results of the antenna pattern and a stationary cloud/precipitation system with a simple Gaussian shaped power pattern in azimuth are examined. The observed bias of radial velocity is less than 1 m s^{-1} for typical cloud and precipitation system that are larger than the beam width of the antenna, but it is stronger at the edges of ground targets or small convective cells at far range whose azimuthal width is of the order of a beam width. Thus, unless there are strong reflectivity gradients where the large phase shifts associated with the main beam edges might dominate the measured velocity, the antenna phase pattern does not introduce a significant bias in the radial velocity measurement.

3.4 Summary

This paper presents the measurement of the phase pattern of parabolic radar antennas and evaluates its impact on the radar data quality that is seldom discussed in the meteorological radar community. The phase patterns obtained by two observation approaches, active scanning of an isolated fixed communication tower and passive reception of a point emission source, both lead to a consistent pattern of phase within the main beam and large changes as we approach antenna nulls. In high reflectivity gradients typical of a clutter environments, the antenna pattern adds some artifacts on the radar data measurements and hence should be considered in ground target selection for radar refractivity retrieval and other measurement techniques for data quality issues that are specifically dependent on target phases.

Acknowledgement

The authors thank Dr. Véronique Meunier, Alamelu Kilambi and Raman Krishnamoorthy of the J. S. Marshall Radar Observatory of McGill University for their help in the antenna measurement. We also thank the three anonymous reviewers whose contribution considerably improved the original manuscript. This work was made possible thanks to the support from Environment and Climate Change Canada and the Natural Science and Engineering Research Council of Canada.

Appendix

Characterization of the antenna phase pattern using a far field microwave source

An experiment using a point emission source was designed to confirm the antenna phase pattern obtained from ground targets. The radar passively received the signal from this source deployed 10.92 km away at an azimuth of 318.5° and about 50 m above the antenna level. The I, Q time series data at multiple PPIs from 0.3° to 2.3° elevation angles with 0.1° interval were collected. Then, a series of range height indicators (RHIs) were performed at 317.5° azimuth ($_{aziRHI}$), which is a degree away from the direction of the source. Our radar has no azimuth positioning control and no azimuth readback when the motor is unpowered. Thus, we needed to manually move the radar for the RHI scan and missed it by 1°.

The resulting one-way relative power pattern (Fig. 3.6 -a) obtained from the emission source shows an azimuthally asymmetric pattern similar to that from the isolated ground target (Fig. 3.1). Even though the phases still vary with the power gradient at each given elevation ($\phi_{(azi,ele)}$, Fig. 3.6 -b), the relative small frequency drift between the source and the receiver caused the phase to shift significantly between successive elevations. At the remote site, a commercial signal generator (Agilent 8648c) with an oscillator stabilized by signals from Global Positioning Satellites provided the source signal. Despite this stabilization, one frequency drifted with respect to the another by ±0.2 Hz (within 4 minutes) with the attendant phase shift. Although as pointed out by an external examiner we could have slaved the radar local oscillator (LO) to the received signal, we did not have the time, equipment, and know-how at the time to do so. Phase drift was too high to allow us to directly characterize the phase pattern of the antenna at different elevations, though it should be sufficient for the close-by azimuths on the same elevation. To compensate for the large phase drift that occurred between 10 seconds PPI scans, the following phase correction procedures were used:

1) The phase measurements made with RHIs sample multiple elevations in a short time, and can be used as a reference to correct the phase of PPI scans. But before using the RHI data, we needed to deal with the slow response of our elevation angle readback for RHI scans (Figs. 3.6 -c,d) that complicated the proper estimation of elevation angles. Based on the fact that the power returns from the RHI scan should be the same as the measurements from the PPI scans at a given position, the power profile of the RHI scans is shifted in elevation to match the power of PPI scans (Fig. 3.6 -c). After the elevation reading biases are estimated, we can displace the phase of the RHI scans to the corrected position ($\phi_{RHIcor(ele)}$, Fig. 3.6 -d);

2) The relative phase of PPI scans with respect to that of the RHI scan is calculated at each elevation (i.e. $\phi_{relazi317.5^\circ(azi,ele)} = \phi_{(azi,ele)} - \phi_{(317.5^\circ,ele)}$, Fig. 3.6 -e);

3) The phases of PPI scans are corrected by forcing the relative phase profile measured at 317.5° azimuth to match the corrected phase of RHI at 317.5° azimuth (i.e. $\phi_{corrected(azi,ele)} = \phi_{relazi317.5^\circ(azi,ele)} + \phi_{RHIcor(ele)}$). To ease the comparison with other phase field, the relative corrected phase is obtained by shifting the phase of the peak power to 0° (i.e. $\phi_{relcorrected(azi,ele)} = \phi_{corrected(azi,ele)} - \phi_{corrected(azi:maxPower,ele:maxPower)}$, Fig. 3.6 -f). We finally account for the two-way path by doubling the relative corrected phase of PPI scans. Though the correction process might be not perfect, it remains the best we can do with the information available, and the resulting pattern (Fig. 3.2) is similar to that observed for a real target in Fig. 3.1.

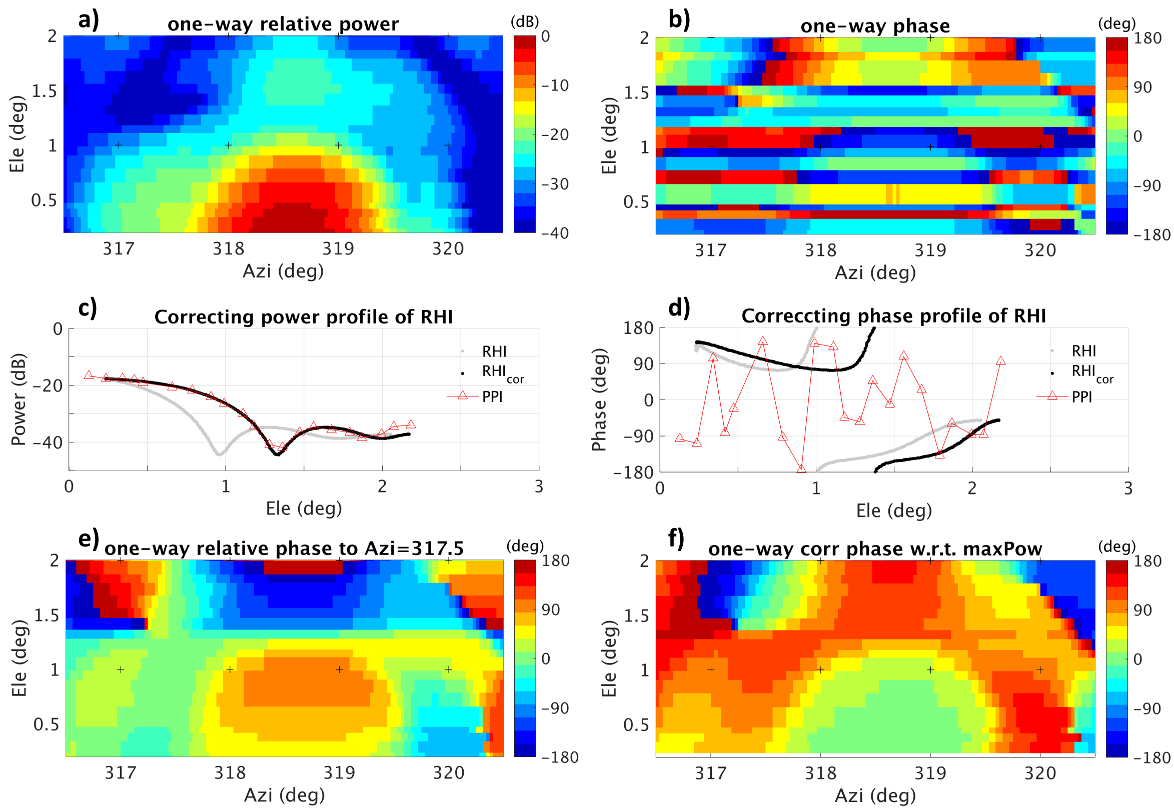

Figure 3.6 – Six-panel plot illustrating the process used to correct the phase drift between the source and receiver as well as the antenna's slow elevation response. (a) and (b): Measurements of the one-way relative power (in dB, normalized to the peak power at 0.3° elevation whose SNR is 60 dB) and phase (in degrees) from PPI scans at successive elevations. (c): Original relative power measurements with delayed elevation response on the RHI (gray line) and power shifted in elevation to the corrected position (black lines) based on the returned power of the PPI scan (red triangles) as a reference. (d): Derived elevation correction permitting us to use the phase from the RHI (gray line for the original data, black line for the elevation-shifted one) to determine what phase should have been read by successive PPIs (plotted in red) at the azimuth of the RHI. (e): Relative phase pattern with respect to the azimuth of the RHI, 317.5°, derived from the original data shown in panel b. (f): Corrected one-way relative phase pattern derived by adding the phase correction of the RHI scan in panel d to the relative phase field in panel e and then shifting these corrected phase for the phase of the peak power equal to 0°.

Chapter 4

Estimating observational errors of radar-derived refractivity by dual-polarimetric and multiple elevation data.

The biases of the radar-estimated refractivity discussed in the previous chapters are correctable given known conditions. However, there are still noises in phase measurements from many other sources that cannot be corrected. This chapter explores and estimates random errors in phase measurements from each individual ground target and their impact on the data quality of refractivity.

The manuscript which constitutes this chapter is in preparation for submission to a peer reviewed journal.

Estimating observational errors of radar-derived refractivity by dual-polarimetric and multiple elevation data.

Ya-Chien Feng and Frédéric Fabry

Department of Atmospheric and Oceanic Sciences, McGill University, Montreal, Quebec, Canada

Abstract

In order to properly use radar refractivity data quantitatively, good knowledge on its errors is required. The data quality of refractivity critically depends on the phase measurements of ground targets that are used for the refractivity estimation. In this study, the observational error structure of refractivity is estimated based on quantifying the uncertainties of phase measurements. New correlations between the time series of phase measurements at different elevation angles and between polarizations are developed to assess the bulk phase variability of individual targets. Then, the observational error of refractivity is obtained by simulating the uncertainties of phase measurements through the original refractivity estimation method. Resulting errors in refractivity are found to be smaller than 1 N-unit in areas densely populated with ground targets, but grow as target density becomes sparse.

4.1 Introduction

Convection initiation and short-term quantitative precipitation forecasting are sensitive to the moisture variability at the surface (e.g., Zawadzki et al., 1981; Crook, 1996; Weckwerth et al., 1999; Fabry, 2006). High spatial and temporal resolution near-surface moisture measurements are thus needed for improving the initial conditions in storm-scale numerical weather prediction (NWP) models (Emanuel et al., 1995; Dabberdt and Schlatter, 1996; Fabry and Sun, 2010; Hanley et al., 2011; Ha and Snyder, 2014; Madaus and Hakim, 2016). The refractivity (N) field estimated from weather radars (Fabry et al., 1997) provides a proxy for two-dimensional near-surface moisture distribution. The high spatio-temporal resolution refractivity field illustrates the horizontal humidity variations, which benefits studies on convection initiation and boundary layer evolution (Weckwerth et al., 2005; Fabry, 2006; Buban et al., 2007; Koch et al., 2008; Bodine et al., 2010).

Preliminary studies have demonstrated the positive impact of ingesting the radar refractivity fields into the NWP models to initialize the low-level moisture field (Montmerle et al., 2002; Sun, 2005; Gasperoni et al., 2013; Seko et al., 2017). The results of quantification precipitation forecasting were improved by the adjusted distribution and quantity of low-level humidity. In addition, the refractivity fields are applied to evaluate the model forecasts at different horizontal grid resolutions (Nicol et al., 2014; Besson et al., 2016). Greater differences in refractivity between radar estimates and model forecasts are particularly found in NWP models with finer horizontal resolution. This suggests the critical need for assimilating radar refractivity data into advanced high resolution NWP models. The WMO (2015) further advocates for more studies on the impact of assimilating radar-estimated refractivity for real cases to examine the value for operational high-resolution nowcasting NWP models.

In optimal interpolation (OI) based data assimilation (Daley, 1991; Kalnay, 2003), the updated analysis $\mathbf{X}_a$ can be written in matrix form as :

$$\mathbf{X}_a = \mathbf{X}_b + \mathbf{W}(\mathbf{y} - H(\mathbf{X}_b)). \tag{4.1}$$

Here, H is the linearized observation operator that transfers the background field $\mathbf{X}_b$, the unobserved state variables in the model, into simulated observations compatible with the observations $\mathbf{y}$. The optimal weight matrix $\mathbf{W}$ equals $\mathbf{BH}^T(\mathbf{HBH}^T + \mathbf{R})^{-1}$, where $\mathbf{B}$ and $\mathbf{R}$ are the background and observational error covariances respectively. The value of the increment $(\mathbf{X}_a - \mathbf{X}_b)$ of the analysis field depends on the innovation $(\mathbf{y} - H(\mathbf{X}_b))$ and the optimal weighting $\mathbf{W}$ determined by the ratio of $\mathbf{B}$ and $\mathbf{R}$. Hence, $\mathbf{B}$ and $\mathbf{R}$ need to be estimated to properly assign the weights of observations in optimal estimation methods. We will not discuss $\mathbf{B}$ in this research, since it is strongly model dependent. The observational errors $\mathbf{R}$ are conventionally assumed randomly distributed in space with a Gaussian distribution with no clear justification or basis for this choice, since $\mathbf{R}$ are not well known and quantified. Quantitative knowledge on the data quality and observational errors is an essential step toward properly using this data in NWP models. The understanding of this knowledge still remains unresolved and hinders the application of refractivity. Therefore, this study aims to investigate the quantitative characteristics of observational errors of radar refractivity.

The observational error matrix in data assimilation can generally be attributed to four sources: 1) instrument and measurement error, 2) errors due to data processing (quality control), 3) errors introduced from observation operator (forward model), and 4) representativeness errors (i.e. different representativeness of resolved spatial scales between models and observations). Obtaining observational error remains challenging, since the true value of the atmospheric state is unknown. Some methods have been proposed to estimate the magnitude and characteristics of observational errors. One is the error inventory method that analyzes all the contributions of the uncertainties to the observations. For example, Keeler and Ellis (2000) used the knowledge on data quality of radar signals to estimate the observational errors of radar reflectivity and radial wind caused by measurements and data processing. In addition, diagnostic methods are popularly applied in the model community for estimating observational errors. The errors are mainly obtained based on other collected observations or output from data assimilation systems, e.g. observation-minus-background and observation-minus-analysis (Hollingsworth and Lonnberg, 1986;

Desroziers et al., 2005; Waller et al., 2016).

The observational error of radar refractivity must be well determined in order to properly weight the observation data in approaches based on optimal estimation, such as data assimilation, data integration of a radar network and instrument synergy. Hence, the goal of this work is the estimation of the observational errors of radar refractivity through the error inventory method. In Section 4.2, all possible sources of uncertainty in the radar phase measurements and data processing based on the original radar refractivity technique (Fabry et al., 1997) are revisited and discussed. In Section 4.3, we propose a method to estimate the uncertainties of the radar phase measurements that have not been quantified before. The errors of radar refractivity associated with the instrument measurements, data processing and estimation method are estimated in Section 4.4. We summarized our findings in Section 4.5.

4.2 Sources of uncertainty in radar refractivity

In this section, we revisit the basic concept and data processing processes of radar refractivity estimation. These enable us to sort out the sources of the uncertainties in radar refractivity.

4.2.1 The basis behind radar derived refractivity

The time t_{travel} that electromagnetic waves travel between the radar and a stationary ground target depends on the refractivity of the air along its propagation path. Fabry et al. (1997) used the phase signal from a fixed ground target as a proxy for t_{travel} to estimate the air refractivity. The radar-measured phase (ϕ) of a stationary point ground target depends on the time taken by a radar pulse for a two-way path:

$$\phi(r) = 2\pi f t_{travel} = \frac{4\pi f}{10^6 c} \int_0^r [N(r', t) + 10^6] dr', \tag{4.2}$$

where f is a stable radar transmitter frequency, r is the one-way beam path range from the radar to the target and c is the speed of light in vacuum. Since r is not known with the required precision to use (4.2) and since the observed phase largely exceeds 2π, the phase difference ($\Delta\phi$) of a stationary ground target between a scan at time t and at a reference time t_{ref} can be used to relax considerably the need for precision on r and reduce the problem of the aliasing of phases:

$$\Delta\phi = \phi_t - \phi_{t_{ref}} = \frac{4\pi f}{10^6 c} \int_0^r \left[N(r', t) - N(r', t_{ref})\right] dr'. \tag{4.3}$$

To estimate N as opposed to simply ΔN between two time steps, the reference phase ($\phi_{t_{ref}}$) is determined in condition when N_{ref} is assumed to be nearly homogeneous with a known value. The temporal local small-scale variations of refractivity ΔN can be derived as the radial gradient of the phase difference between these targets. By adding ΔN to the known N_{ref} field, the refractivity value can be estimated.

There are several processing steps to get the refractivity field from the radar measurements as shown in Fig. 4.1 (Fabry and Pettet, 2002). At calibration stage, $\phi_{t_{ref}}$ from a known homogeneous refractivity field N_{ref} and the data quality of ground targets are required to be prepared. At real time stage, the $\Delta\phi$ field between the current time and the reference time is calculated. Then, the noisy $\Delta\phi$ field is processed, e.g. smoothing weighted by reliability of targets, dealiasing and interpolations, to obtain a smoother $\Delta\phi$ field for easily estimate the local ΔN from the radial slope of the processed $\Delta\phi$ field. The final N field is obtained as the sum of N_{ref} and ΔN.

The data quality of the radar refractivity is affected both by the *phase measurements of ground targets* and by the *radar refractivity estimation method*. Note that the estimation method includes the data processing procedures and the local N estimation as mentioned in the previous paragraph. Nevertheless, previous studies mainly focused on the qualitative discussions of different sources of phase measurements uncertainty (see the following section), but seldom investigated the magnitude of the uncertainties and the estimation method.

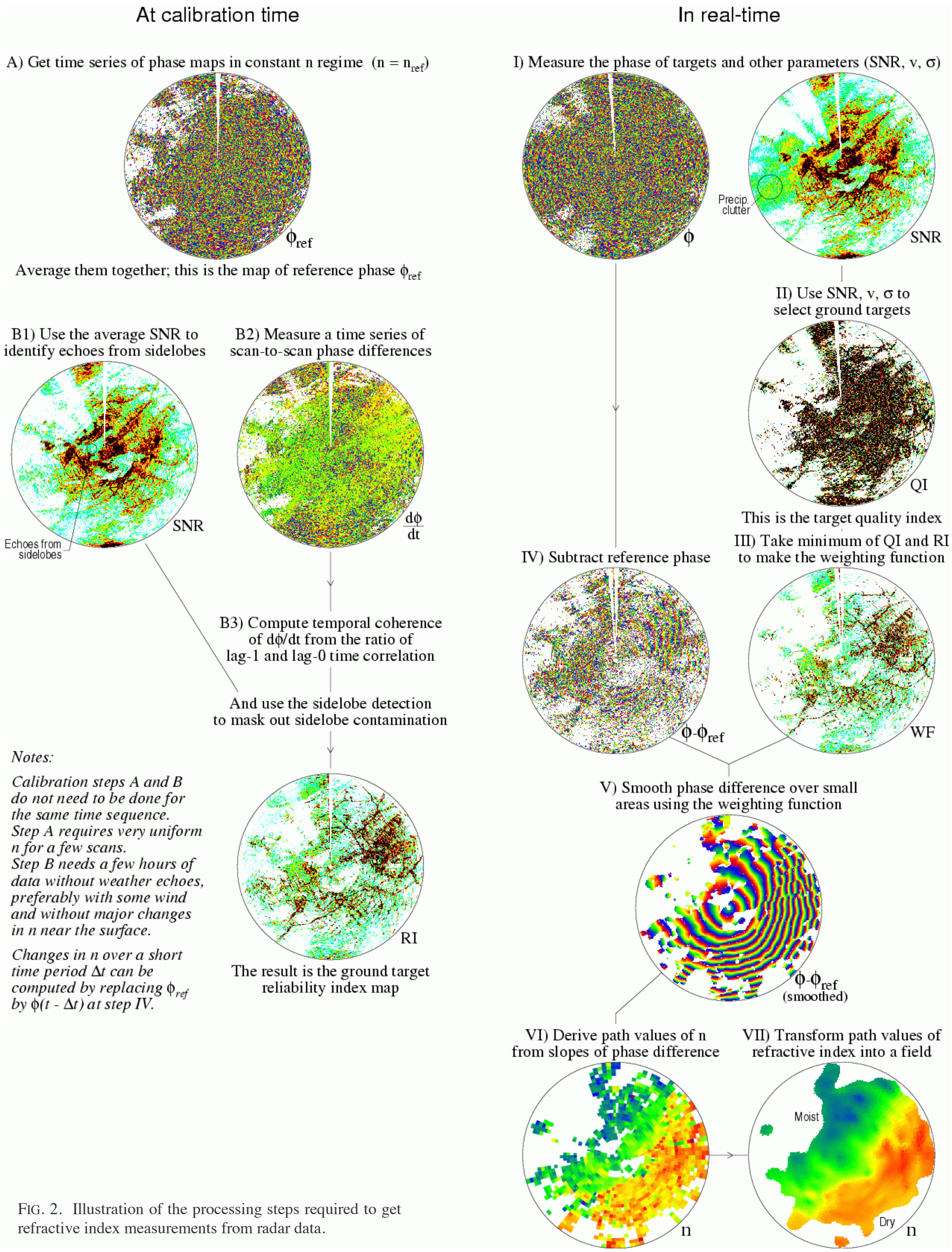

Figure 4.1 – The data processing flow chart of obtaining near-surface refractivity from radar measurements (Fabry and Pettet, 2002).

4.2.2 Uncertainties of the phase measurements of ground targets

The phase caused by the change in refractivity at given height above the terrain is the signal of interest for radar refractivity (Fabry, 2004; Feng et al., 2016). However, different reasons other than this atmospheric-driven signal also lead to uncertainties in ϕ and introduce errors in the refractivity estimations. Generally, contributions to the uncertainty in the phase measurement come from the phase variations associated with issues of radar hardware, radar wave propagation conditions, and characteristics of ground targets. The details of each category are described as follows.

- Radar hardware: Phase uncertainty associated with radar hardware issues includes the varying frequency of a magnetron-based radar (Parent du Chatelet et al., 2012; Nicol et al., 2013) and the phase pattern of the parabolic antenna (Feng and Fabry, 2016). These systematic phase shifts can be corrected individually by knowing the fluctuating local oscillator frequency and the antenna phase pattern.

- Radar wave propagation conditions: Electromagnetic wave propagation conditions associated with the vertical refractivity gradient (dN/dh) and the heights difference between the radar and ground targets have been considered the major problem in the original method (Fabry, 2004; Park and Fabry, 2010; Bodine et al., 2011). A novel method to reduce this uncertainty caused by the coupling effect of dN/dh and target heights has been proposed in Feng et al. (2016). Moreover, precipitation along the wave path also affects the phase measurements, which can be estimated by the rainfall rate (Bodine et al., 2011).

- Characteristics of ground targets: The uncertainties of the phases related to the characteristics of ground targets include the movements of targets, changes in how a complex target with multiple reflecting elements illuminated by the radar (Fabry, 2004), sidelobe contamination from strong neighboring targets (Besson et al., 2012; Nicol and Illingworth, 2012) and the unknown target locations with respect to the center of the sampled gate. The uncertainties of target locations in range, azimuths or heights affect the interpretations and representativeness of phase measurements, even for ideal stationary point-like targets. For example, the unknown ranges of targets in conjunction with transmitter frequency fluctuations result in random phase errors, which are proportional to the magnitude of the frequency changes and pulse length (Nicol et al., 2013). In addition, considering targets are not aligned in the same azimuth and local refractivity changes, some spatial noisiness of phase might also be introduced.

The uncertainties in phase measurements can be classified into *biases* and *errors*. Biases are systematic given conditions and can be corrected based on these known conditions, such as measured changes in the unstable frequency of the local oscillator, estimated dN/dh, etc. Phase uncertainties due to radar hardwares, the coupling effect of changes in dN/dh and uneven target heights, as well as precipitation are considered as *biases*. These systematic biases need to be corrected during the data processing. Then, the unbiased refractivity could be properly used in quantitative applications. On the other hand, those phase uncertainties that can not be corrected are *errors*. The phase errors include the random phase changes introduced by the unknown target characteristics, e.g. movements, complexity, and locations. Since these terms are independent, the total error variance of phase ($\sigma^2_{\phi total}$) equals the sum of individual error variances:

$$\begin{aligned} \sigma^2_{\phi total} = \sigma^2_{\phi}(\text{target movement}) + \sigma^2_{\phi}(\text{target complexity}) \\ + \sigma^2_{\phi}(\text{target location and small-scale refractivity changes}) \end{aligned} \tag{4.4}$$

4.3 Estimating phase measurement errors $\sigma^2_{\phi total}$

Estimating $\sigma^2_{\phi total}$ as a bulk error remains a challenge, not to mention each individual term in (4.4). It is an ill-posed problem to obtain the signal and noise simultaneously with limited phase measurements. Therefore, we propose a new method for qualitatively estimating $\sigma^2_{\phi total}$ through more phase measurements collected at multiple antenna elevations and from dual-polarization.

4.3.1 Correlation of two time series of radar signals

Let us conduct a simple thought experiment to help understand the correlation of the radar signal at two lower elevation angles. An ideal stationary point-like target is considered here and it is located well within the main lobe of the antenna, where the antenna phase pattern is constant (Feng and Fabry, 2016). When there is no temporal change in refractivity, the phase measurements from an ideal target at two low antenna elevations, say 0.3° and 0.5°, are constant in time. Meanwhile, the time series of phase measurements at horizontal and vertical polarizations at given elevation are also constant. In other words, the phase differences between two elevations or between two polarizations stay constant in time. Nevertheless, for non-ideal ground targets, the phase differences between two elevations vary temporally because of target movements and unknown target locations issues associated with small-scale refractivity changes as mentioned in (4.4). The phase difference between polarizations also shows temporal variability caused by the complexity of targets due to the changing illumination of the targets. Therefore, the information of phase difference between polarizations and between elevations provides both qualitative and quantitative insights on the phase errors.

We use the correlation coefficient (ρ) of two time series of phase measurements, ϕ_1 and ϕ_2, over M volume scans from a given ground target to quantify the temporal variation of phase differences. Then, ρ can be expressed as:

$$\rho = \frac{1}{M}\left|\sum_{m=1}^{m=M} exp(i(\phi_{2,m} - \phi_{1,m}))\right|. \tag{4.5}$$

When ϕ_1 and ϕ_2 are identical or with a constant phase difference in time, ρ is equal to one. For most targets, ρ decreases with increasing temporal variability of $\phi_2 - \phi_1$ due to target movements under various wind speeds, small-scale refractivity variations, and complicated wave interferences of non-ideal point targets. We learned that ρ qualitatively decreases with the temporal fluctuations of the phases, but quantifying these phase errors (σ_ϕ^2) is a problem that need to be solved in order to estimate the error of radar-estimated refractivity.

Note that we do not calculate the correlation between the original returned signal V that generally used in the radar signal processing. V is a complex number as $V = A\exp(i\phi)$, where A is the amplitude of the signal and ϕ is the phase. It is because the returned power fluctuates in time for many reasons and then affects the magnitude and the representativeness of correlation calculated from these signals. Therefore, we use the correlation of phases to determine the temporal variation of the phases difference and exclude the effects of fluctuating amplitudes.

4.3.2 Which correlation to use?

The correlation ρ of phases can be calculated between two elevations (ρ_{ele}), between two polarizations (ρ_{pol}) or from a time series of successive scans at a given polarization and elevation using lagged autocorrelation (ρ_{auto}). Here, we will discuss and compare the differences between these ρ (Fig. 4.2) calculated from three hours data of the McGill radar. The selected time period is 11-14 UTC (7-10 LST) Oct 30, 2012. The weather condition was cloudy with some showers. The average wind speed is 7 m s^{-1} and the average vertical gradient of refractivity is about -70 $\pm$15 km^{-1}.

(i) ρ_{ele} is a useful indicator to distinguish the reliability of targets, particularly under windy conditions. This correlation is calculated from time series of phases at two successive antenna scanning elevations, e.g. 0.3° and 0.5° for the McGill radar. For stationary ideal point-like targets located within the radar antenna main beam, the phase difference between nearby elevations is constant in time and only related to the antenna phase pattern (Feng and Fabry, 2016). The time interval between these two elevations is about 10 seconds and the temporal refractivity changes within this short time period can be assumed to be negligible; note that this is only true if the time interval between the two elevations is very short. Thus, the temporal variability of the phase difference between these elevation scans is mainly caused by the changes in target characteristics (i.e. movement and complexity in (4.4)). For example, a strong wind causes targets movements and shape changes even within few seconds, and leads to temporal phase difference between two elevations and reduces the magnitude of ρ_{ele}. On the other hand, a larger area of high ρ_{ele} might happen during calm nights. Figure 4.2a shows the distribution of ρ_{ele} at the horizontal polarization in a windy morning. Higher values of ρ_{ele} shown as reddish colors represent the reliable ground targets with smaller phase errors. On our radar, the number of targets (Fig. 4.2e) whose ρ_{ele} greater than 0.8 is about 15000, which is 1% of data within a 62.5 km radius. In addition, ρ_{ele} fields at horizontal and vertical polarization show very similar distribution (Figs. 4.2 a and b), the small differences are due to the antenna pattern and the target characteristics responding to the different polarizations.

(ii) ρ_{pol} is best used to distinguish point or point-like targets from complex ones. For point-like ground targets, the phase difference between the (simultaneously transmitted and received) horizontal and vertical polarizations is constant in time, since it is solely related to the discrepancy of the antenna phase patterns at each polarization. In consequence, the value of ρ_{pol} of point-like targets is expected close to one. For complicated targets, the phase difference between the two polarizations varies temporally and this results in a lower ρ_{pol}. The phase discrepancy between polarizations mostly occurs during atmospheric inversion conditions at night with strong negative dN/dh values. When the radar beam bends towards the ground, the main beam may illuminate more of the full vertical extent of targets or surrounding targets, such as the ground, shorter buildings etc., that were not seen by the main beam under normal propagation conditions. Then, the complicated shape of the targets responds differently to horizontal and vertical polarizations, and lower value of ρ_{pol} is consequently expected for the complicated targets. Though ρ_{pol} is a good indicator for the ground target properties, it cannot provide too much information on the phase error caused by target movement and small-scale refractivity changes. The values of ρ_{pol} (Fig. 4.2c) are thus mostly higher than ρ_{ele}. The histogram of ρ_{pol} (Fig. 4.2f) shows the majority of ρ_{pol} centered around 0.4, which is different from the distribution of ρ_{ele} (Fig. 4.2e) that is more skewed towards zero.

(iii) The autocorrelation ρ_{auto} of phases at a given elevation and polarization but between successive volumes scans is dominated by the temporal refractivity change between volume scans, whose time interval depends on radar scanning speed (e.g. 5 minutes for the McGill radar). The phase change due to the refractivity variation between successive volume scans is generally larger than other causes in (4.4). Thus, the values of ρ_{auto} (Figs. 4.2d and h) are smaller than the previous correlations, particularly with greater effects at further range. ρ_{auto} does not represent the variance of phases errors. Nevertheless, ρ_{auto} can be useful to determine the reliability of ground targets only under one special condition, that is the homogeneous refractivity field in time and space at the calibration stage (Fabry et al., 1997).

(iv) Discussion: Based on the different characteristics of each correlations (Table 4.1), we suggest to apply ρ_{ele} for selecting reliable ground targets and estimating the phase errors. ρ_{ele} is the most representative of the phase variability among other correlations. Even though ρ_{ele} still underestimates the effect of uncertainties of target locations, it is so far the best we can do. The causes of phase variability σ_ϕ^2 discussed in (4.4), e.g. the movements, complexities and locations of ground targets, are related with the near-surface wind condition. ρ_{ele} varies temporally and decreases with increasing wind speed. The time-dependent ρ_{ele} provides an effective way for real time ground target selection and quantification of the error of phase measurements for the radar-estimated refractivity technique.

Physical cause	ρ_{ele}	ρ_{pol}	ρ_{auto}
ΔN between volume scans			Y
- Target movement	Y		Y
- Target complexity	Y	Y	Y
- Target location and ΔN at smaller scale	P		Y

Table 4.1 – Summary of different correlation coefficients (ρ) associated with various physical effects. "Y" indicates that ρ is affected by the corresponding physical cause. "P" means that ρ is only partially affected by the physical cause.

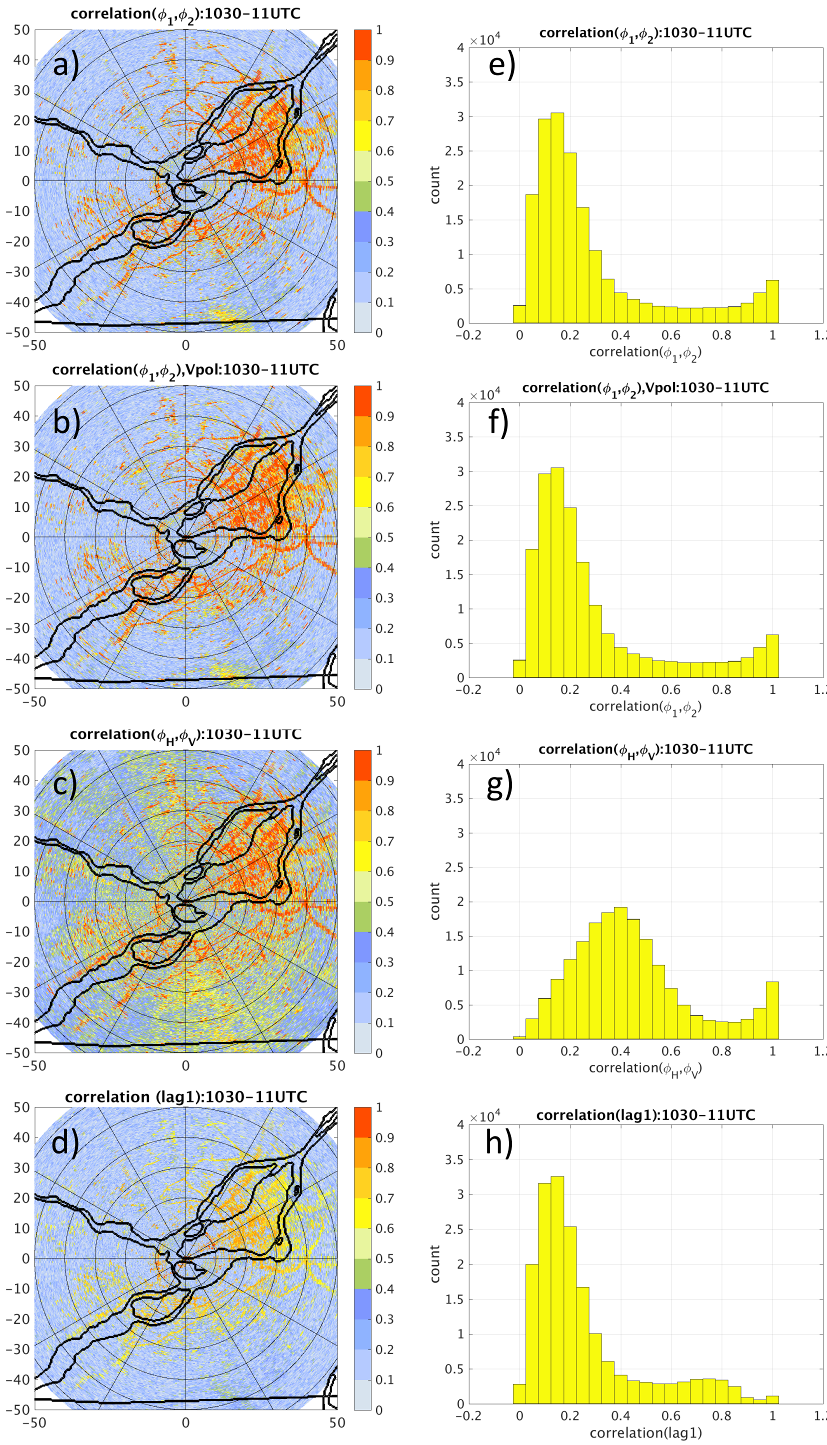

Figure 4.2 – a)-d): The distribution of correlation coefficient (ρ) of different combinations of phase series observed from the McGill radar at the origin with a 50-km radius coverage during 11-14 UTC Oct 30, 2012. a) Correlation coefficient of two antenna scanning elevations (ρ_{ele}), 0.3° and 0.5° at horizontal polarization. b) ρ_{ele} at vertical polarization. c) Correlation coefficient between the horizontal and vertical polarizations (ρ_{pol}) at 0.3° antenna elevation. d) Autocorrelation of phase series (ρ_{auto}) at the horizontal polarization and at 0.3° antenna elevation. e)-h): Histograms of each correlation coefficient shown in a)-d).

4.3.3 Link between ρ and σ_ϕ

We must now derive a relationship between the correlation of two time series of phase and the standard deviation of phase error, hereafter ρ-σ_ϕ relationship. At first, the error of the phase measurement is assumed to follow white Gaussian noise statistics with a given standard deviation, σ_ϕ. Even though the noisy phases caused by atmospheric scintillation and target movements might vary as a function of time, white noise statistics is the only assumption we can make given the limited observation samples and unknown wind conditions. To derive the ρ-σ_ϕ relationship, we performed a simulation: time series data of fluctuating phases $\phi_{1,M}$ and $\phi_{2,M}$ are generated independently as random white noise with a given σ_ϕ and zero mean. For these calculations, we chose to use $M = 36$ volume scans of time series, and the reasons will be explained in the next paragraph. Then, ρ of these simulated $\phi_{1,M}$ and $\phi_{2,M}$ is calculated for a variety of σ_ϕ, ranging from 0° to 120°, shown as blue dots in Figure 4.3. The ρ-σ_ϕ relationship is fitted with a Gaussian distribution as $\rho = exp(-(\sigma_\phi/59.2)^2)$, shown by the red line. Furthermore, the ρ-σ_ϕ relation we fitted here is very similar to the conventional equation of estimating the angular standard deviation of phase based on a wrapped normal distribution: $\sigma_\phi = 180/\pi[-ln(\rho^2)]^{1/2}$, i.e. $\rho \approx exp(-(\sigma_\phi/57.3)^2)$ (Mardia, 1972; Weber, 1997). Even though the ρ-σ_ϕ relation has existed, the simulations done here help investigate the sensitivity of sampling issues.

Since the magnitude of phase error changes with time, the length of the time series used to estimate that fluctuation must be a compromise between greater accuracy calling for longer time series and adaptability to changing conditions calling for shorter time series. The issue of sampling number in the ρ-σ_ϕ relationship is examined. The ρ-σ_ϕ fitting starts to converge around 30 samples where the relationship is $\rho = exp(-(\sigma_\phi/60)^2)$. The fit becomes stable when there are 60 samples and the relationship turns into $\rho = exp(-(\sigma_\phi/57.5)^2)$. The slight difference in the fitting coefficient between 30 and 60 samples does not affect σ_ϕ too much under a given ρ. Therefore, sample numbers greater than 30 are acceptable to apply the fitted relationship. In this work, we used 36 samples of the time series, corresponding to three hours of data for the McGill radar, to obtain the ρ and ρ-σ_ϕ relationship. In the end, σ_ϕ can be estimated based on ρ calculated from the radar

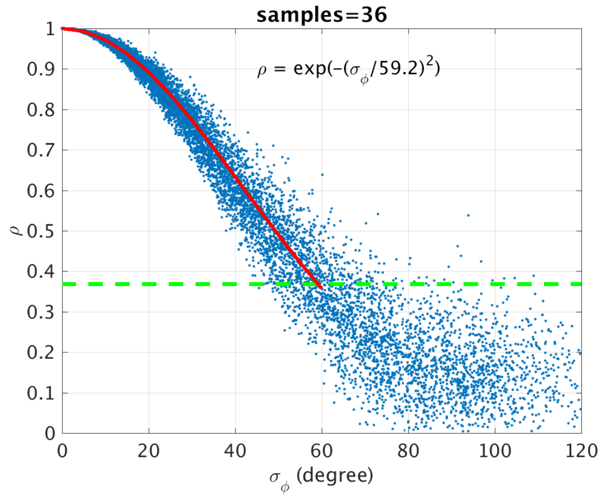

Figure 4.3 – Correlation coefficient (ρ) between two time series of phase measurements having a random noise with a standard deviation σ_ϕ. Multiple simulations have been done with varying σ_ϕ as blue dots. Then, a fitted Gaussian relation is shown in red. Note that only simulations with ρ greater than 1/e (green line) are used in the regression, because there is no clear skill in connecting ρ and σ_ϕ when ρ is less than 1/e.

observation and the newly-derived ρ-σ_ϕ relationship, at least as long as ρ is greater than 1/e.

4.4 Estimating N errors caused by the radar refractivity estimation method

The data quality of the radar refractivity depends on the *phase measurements* of ground targets and the radar refractivity *estimation method*. The method of obtaining the variance of random phase error σ_ϕ has been developed in the previous section. Here, we will estimate the N error that phase errors introduce through data processing and the radar N estimation method. The following steps show how we attempted to assess the errors in N: 1) For each individual ground target, ρ_{ele} is calculated from the observed phase measurements at two low antenna elevations. Consequently, σ_ϕ is obtained according to the calculated ρ_{ele} and the ρ-σ_ϕ relationship. 2) The noisy phase of each target is simulated randomly based on Gaussian statistics with a zero mean and the assigned σ_ϕ from the previous step. Then, a noisy phase field is obtained based on the noisy phase of each targets superposed on a known phase field for a given ΔN condition, which is set zero here. For targets whose ρ_{ele} is less than 1/e, the added phase noise is randomly assigned a value from -180° to 180°. 3) After processing the noisy field in the radar refractivity estimating method (Fabry and Pettet, 2002), the refractivity error is obtained by comparing estimated N with the the expected one.

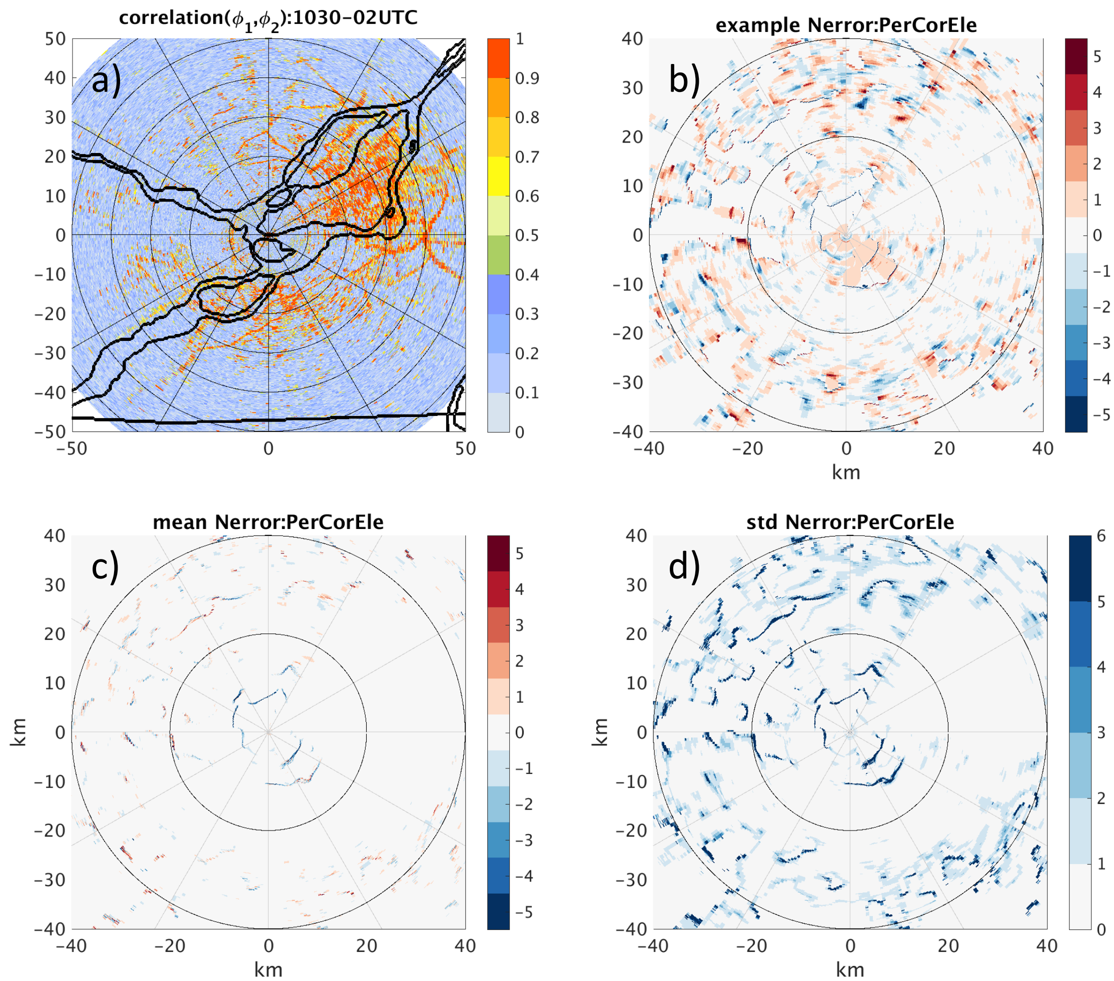

Figure 4.4 – Illustration of the results of the simulation of errors in estimated refractivity. a) Correlation coefficient of phases at two elevations (ρ_{ele}). b) Error of refractivity, N_{error}, obtained from one simulation of the noisy phases perturbed based on a). c) Mean of N_{error} based on 30 simulations. d) Standard deviation of N_{error} based on 30 simulations.

The refractivity error (Fig. 4.4b) is obtained based on the phase perturbation estimated from the ρ_{ele} field (Fig. 4.4a). The errors in refractivity are not randomly distributed as generally assumed for the observational error for data assimilation, but are associated with the density of reliable targets. In areas with dense reliable ground targets of higher ρ_{ele}, the errors of refractivity are close to zero and are smaller compared with those in the areas with less ground targets. What this experiment confirms is that we can use the radar-estimated refractivity with higher confidence in areas having a greater number of reliable targets. This process of taking a known phase field, adding a random noise based on the expected phase fluctuation for each target, estimating N, and comparing it with the truth was repeated 30 times in order to determine with more reliability the magnitude and sign of expected errors. The ensemble mean of refractivity error field, $\overline{N_{error}}$, is almost zero as shown in Fig. 4.4c. The ensemble standard deviation of the refractivity error, $\sigma_{N_{error}}$, is within $\pm$ 1 N-unit in areas with numerous reliable targets, generally in urban and suburban regions (Fig. 4.4d). Based on Fig. 4.4d, the mean $\sigma_{N_{error}}$ is inversely proportional to the areal target density fraction above a given threshold, here say $\rho_{ele} > 0.6$ (Fig. 4.5). In addition, this simulation is repeated with a higher value of average ΔN, say 30 N-unit, in order to examine the impact of the phase errors on the refractivity under the extreme condition with large phase gradient. The $\sigma_{N_{error}}$ field shows the similar pattern as it when ΔN equal to 0 N-unit in Fig. 4.4d.

It is worth noting that some artificial azimuthal wavy patterns with larger values are shown in both $\overline{N_{error}}$ and $\sigma_{N_{error}}$ fields (Figs. 4.4c and d). These wavy patterns usually occurred at locations with fewer ground targets, where the radial gradient of phases is difficult to estimate from the raw observational data. We have found that these patterns also appear in the long-term climatological refractivity mean field. This highlights the need to improve the current refractivity estimation method particularly in regions with fewer ground targets.

4.5 Summary

In this study, the refractivity errors associated with phase measurement uncertainties and the estimation method itself are examined together for the first time. We tackled this issue by relying on estimates of phase errors gained from the newly added phase

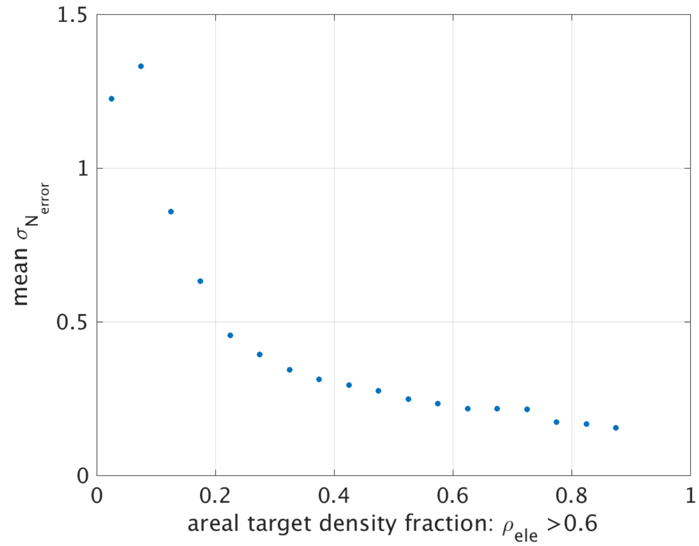

Figure 4.5 – Relationship between the mean $\sigma_{N_{error}}$ and the areal fraction of target density ($\rho_{ele} > 0.6$, i.e. σ_ϕ about 45°) within an area of 5° in azimuth by 4 km in range. The total area considered here is from 20 to 40 km in range in Fig. 4.4d.

observation at different elevations and polarizations. The variance of phase errors can be determined based on two pieces of newly learned information: the first is the phase correlation ρ from phase measurements at different elevations; the second is the derived ρ-σ_ϕ relationship between phase errors and these correlations. The phase errors we obtained here are a bulk quantity, with contributions from independent sources caused by the target characteristics, such as movement, target complexity and uncertainties in locations. The error of refractivity is then estimated using the simulated phase error and the original refractivity estimation method.

The examined refractivity error field is not randomly distributed, but is associated with the areal density of reliable ground targets. Random errors smaller than 1 N-unit are found in high density areas of reliable targets, but larger errors with radial patterns are found in areas with fewer targets. The characteristics of refractivity errors benefits the quantitative applications of radar-estimated refractvitiy, such as providing solid knowledge on observational errors for data assimilation. In addition, the quantification of the phase uncertainty for each individual ground targets offers insights on future improvement of the refractivity estimating method.

Chapter 5

Summary and future work

This thesis is dedicated to quantifying the uncertainties of the phase measurements of ground targets and the derived refractivity fields. Generally, the phase measurements from ground targets are interpreted as the sum of phase variations due to refractivity changes along the beam path and of other sources of phase variability. The noisy spatial phase measurements caused by sources other than refractivity variations have been the major problem in the radar-estimated refractivity technique. This problem causes difficulties in data processing and degrades the accuracy of refractivity estimations. In this study, the uncertainties of phase measurements and their impacts on the quality of estimated refractivity are quantified as biases and errors. Biases are correctable under given known conditions, but random errors can only be estimated rather than corrected. Two sources of bias were investigated in this study, the combined effect of changes in the refractivity profiles and varying altitudes of ground targets (Chapter 2), and the newly explored phase pattern of a parabolic antenna (Chapter 3). The random errors are estimated using a new method based on the correlations of phase data (Chapter 4).

In Chapter 2, the phase change due to refractivity profile and the varying altitudes of ground targets are analyzed and quantified to clarify the representativeness of the phase measurements and its impact on the refractivity estimation. The vertical gradient of refractivity determines the beam propagation. The trajectory between the radar and each individual target at various heights affects the phase measurements through the path range and refractivity sampled along its path. This partly gives rise to the problem of noisy phase measurements that cannot be explained by the simplistic assumption originally made by (Fabry et al., 1997). Though Park and Fabry (2010) developed a phase measurement simulator to describe the phase change considering the beam trajectory to ground targets as function of propagation conditions, we attacked the problem more systematically to detangle the complicated contributions of propagation conditions through detailed decomposition of the individual physical effects causing phase variation. It shows that the cause of phase bias due to the vertical refractivity change is mainly associated with the variability of target heights and not as much with the variation of the path range and the beam curvature. This key cause of phase noisiness in space further affects our ability to compute the radial gradient of phase difference, introducing significant local refractivity biases when the propagation condition changes, particularly at far ranges.

A practical method is then proposed to quantify these prevailing phase biases associated with the two key unknowns, target heights and refractivity profiles. The heights of most targets are difficult to obtain, but the terrain information can be used as a proxy. The assigned height above the terrain, 10 m, is reasonable for most rural and suburban areas. In addition, a novel method has been developed to estimate the temporal variation of dN/dh. Its concept is based on the fact that the returned power difference of a point-like target between two scanning elevation angles is inversely linearly related to the changes in dN/dh. An ensemble of point-like targets is used to estimate an areal average dN/dh. The obtained values show promising consistency with the in-situ observations from the BAO tower. With the known conditions of target heights and dN/dh, this bias source of phase measurements is thus quantified and corrected to better estimate the local refractivity changes at a given height above the terrain. This correction also clarified the height representation of the refractivity data for further applications.

In this study, we assume that dN/dh is homogeneously stratified parallel to the radar height in order to simplify the interpretation of the phase simulator and the dN/dh estimation method. However, spatial variability of dN/dh is expected in both horizontal and vertical directions. The changes in dN/dh are affected by the land-atmospheric interaction over heterogeneous surfaces (terrain) and the advections of the weather systems. Therefore, a more sophisticated description of the phase simulator considering the spatial variability of dN/dh requires more investigation. If there are enough point-like targets to allow for a regionally-based estimation, the current dN/dH method could be improved to obtain multiple dN/dh at different azimuthal directions as opposed to a single value for the whole radar domain as was done here. Moreover, the new estimation method considering the bias correction of dN/dH should be applied and examined in real cases.

In Chapter 3, a new source of phase bias associated with the antenna phase pattern was explored. The phase pattern of parabolic radar antenna is originally investigated to understand the phase characteristics of a point-like target at successive elevations. Since the absolute phase pattern was not easily measured and not even well known in the radar meteorology community, this is the first study to discuss the previously-ignored impact of antenna phase pattern on the quality of radar refractivity estimation. The phase pattern in azimuth and elevation is nearly constant within the antenna main beam, but changes significantly as we approach antenna nulls. This implies that, for ground target located close to the main beam axis, the phase measurement will not be affected by the antenna phase pattern. However, the antenna phase pattern adds biases to the phase measurements of targets located close to antenna nulls, especially when propagation conditions change. The ground targets located at different elevations with respect to the phase antenna pattern also lead to the spatial noisiness of phase. Moreover, the antenna phase pattern must be considered when using phases at multiple elevations, as has been suggested, to increase the temporal resolution of radar refractivity estimation to help mitigate the phase aliasing problem (Besson and Parent du Châtelet, 2013).

Errors of phase measurements include contributions from target movements, intrinsic target properties, and unknown locations with respect to the center of the volume gate (Fabry, 2004; Besson et al., 2012; Nicol and Illingworth, 2012; Nicol et al., 2013). The magnitude of phase errors cannot be calculated directly because the information required to quantify the causes is much more difficult to obtain, such as small-scale variations in wind, temperature, and humidity; accurate location or shape of ground targets; and so on. Therefore, these error sources are mainly discussed qualitatively in previous study. In Chapter 4, two new parameters, the correlation coefficients of phases at two elevations and at two polarizations, are explored to estimate the temporal phase fluctuations caused by all of these phase error sources combined. Higher phase correlation coefficients correspond to good targets with less phase errors and whose phase more accurately represent the atmospheric refractivity change. The mathematical relationship between the phase correlation coefficients and bulk phase error variance are established through empirical phase simulations. These efforts enable us to assign the variance of phase errors for individual ground targets based on the real-time phase correlation and the derived ρ-σ_ϕ relationship. More studies on how to intelligently use phases at horizontal and vertical polarization together or alternatively would be welcome.

The phase correlation coefficient is a useful index to determine the reliability of ground targets and quantify the errors. In the original method, ground targets with smaller phase errors are more qualitatively determined and selected based on conventional approaches used to identify ground clutter, e.g., strong returned echo, zero radial velocity and narrow beam width, and a temporal phase coherence calculated during a calibration stage (Fabry, 2004). However, phase errors actually depend on atmospheric conditions. The value of the time-dependent phase correlation lies in its ability to map the changing quality of targets in time and space and better quantify the spatial noisy phase pattern after the phase bias correction. Furthermore, even though the random phase errors cannot be corrected, their impact on refractivity errors can be estimated by using the dynamically-estimated phase errors in the original radar refractivity estimation method.

Using simulations of measurement errors, we finally illustrated how the error of refractivity depends on the density of reliable ground targets instead of varying randomly in space. The error variance of refractivity is within 1 N-unit in high-density reliable ground target areas, but shows higher values in the less dense areas. In areas with fewer ground targets, the estimates should be labeled as having higher uncertainty or just discarded. We also found that the evaluation of the refractivity uncertainties should be done using the complete retrieval process as suggested in Nicol and Illingworth (2012), because this way the sophisticated data processing, e.g. smoothing and phase interpolation, etc., is taken into consideration. The estimated error of refractivity is more representative than simply comparing two targets as done in previous studies (Fabry, 2004; Bodine et al., 2011; Feng et al., 2016).

In summary, the improvements of refractivity estimation are theoretically dependent on the progress on the quantification of phase uncertainties. Phase data collected at multiple low antenna scanning elevations and dual-polarizations add critical useful inputs to the estimation of the vertical gradient of refractivity and the ground target reliability. The newly gained information provides key elements to correct the biases and to assess the uncertainty of refractivity. A refractivity field with better quality, known data representativeness and error structures set the stage for further quantitative applications, such as data assimilation, radar network implementation, and data synergy with other boundary layer instruments. Data collections from extra elevations and polarization are thus suggested for future operational radar networks to extract the desired near-surface thermodynamic conditions.

A remaining challenge facing the refractivity estimation method is how to estimate the refractivity field within areas of large uncertainties of phase measurements, particularly those caused by phase aliasing in conditions of rapid refractivity change, steep topography, or sparse ground target density. Current estimation methods, such as the regression method with a pyramidal weighting function (Fabry, 2004; Hao et al., 2006) or least square fitting method (Nicol and Illingworth, 2012), do not deal with these problems well. Since the error quantification of each target is now better understood, novel methods should be sought in the future. The new question is, "*What is the most intelligent way to extract the useful information from noisy phase measurements with quantified uncertainty?*" The variational method could be one of the attempts to better solve this difficult problem. In addition, the phases of reliable targets along sloping terrain, that have been largely ignored until now, might be used to extract new information on refractivity.

5.1 The road ahead: future applications

As the data quality of radar-estimated refractivity gradually improved, more refractvitiy data could offer a wealth of new research applications. As part of the thinking that shaped this thesis, two new possible applications outside of the previous scope of limited storm related issues were considered, even if they have not yet been thoroughly explored.

5.1.1 Ingesting continental-scale radar refractivity data into regional models

Near-surface thermodynamic observations remain insufficient for the initialization of numerical weather prediction models. Considering the high temporal-spatial resolution of radar refractivity data, previous studies focused on ingesting it into models in order to improve the initial conditions of low-level thermodynamic conditions in storm scale NWP models (Montmerle et al., 2002; Sun, 2005; Gasperoni et al., 2013).

However, we wonder if the radar refractivity from an operational radar network could contribute upscale to regional NWP models. Regional models have larger grid spacing, and it is not immediately clear how representative other point observations from sensors such as surface stations might be on the average condition of the whole model grid box of such larger-scale models. In contrast, the average of few pixels of radar refractivity fields might better describe that state because radar-estimated refractivity makes areal measurements.

The purpose of data assimilation is to find optimal initial conditions, known as analysis, for model integration forward in time. Data assimilation systems statistically combine observations and short-range forecasts by weighting them based on their error information (Kalnay, 2003). The observational and model background error covariance statistics play key roles in the weighting process for successful data assimilation as mentioned in Chapter 4. The knowledge of the background error statistics provides an estimate of forecast uncertainty and quantifies linear multivariate relationships within the model state. The model background error covariance is critical to spread out the information added by observations, or increment, in space as well as between observed and unobserved variables.

The background error covariance matrix describes the magnitude and spatial correlation of expected forecast errors. Currently, there are three common ways to diagnose background error statistics: the innovation method using the difference between observations and background (Hollingsworth and Lonnberg, 1986), the National Meteorological Center (NMC) method using the difference fields between two forecasting time (Parrish and Derber, 1992) and the ensemble method using the ensemble distribution as estimate of error statistics (Fisher, 2003).

Here, we examine the background error covariance based on ensemble model outputs from the Regional Ensemble Prediction System (REPS) version 2.2.0 of Environment and Climate Change Canada (ECCC). This model covers North America and adjacent oceans. The horizontal grid is 600 x 635 latitude-longitude with a 0.1375 degree resolution (about 15 km), and there are 48 vertical levels. A 20-member forecast is produced. We used 12-hr forecasting for all calculations to avoid the correlations coming from the global system and correlated noises used for model initial perturbations. The prognostic variables are winds, temperature, specific humidity, pressure, liquid water content, and turbulent kinetic energy. The detailed model description can be found on the ECCC website: http://collaboration.cmc.ec.gc.ca/cmc/CMOI/product_uide/docs/tech_specifications/tech_specifications_REPS_e.pdf.

First, we analyze the background error correlation for the refractivity field at the lowest model level to examine how far the observation could propagate in space. Figure 5.1a is a monthly average (July 2016) of autocorrelation of the refractivity field between the point closest to the McGill radar and other model grid points. The correlation pattern shows anisotropy with elliptical contours whose major axis tilts to the east-west direction. The autocorrelation length of refractivity is about 300 km in radius, which implies that the information of the point observation is spread over a substantial area. The average refractivity over a small region ($\sim$ 30 km radius) is expected to be more precise and more representative than point observations, making it potentially useful for assimilation.

Refractivity is a function of water vapour pressure, temperature and pressure. The

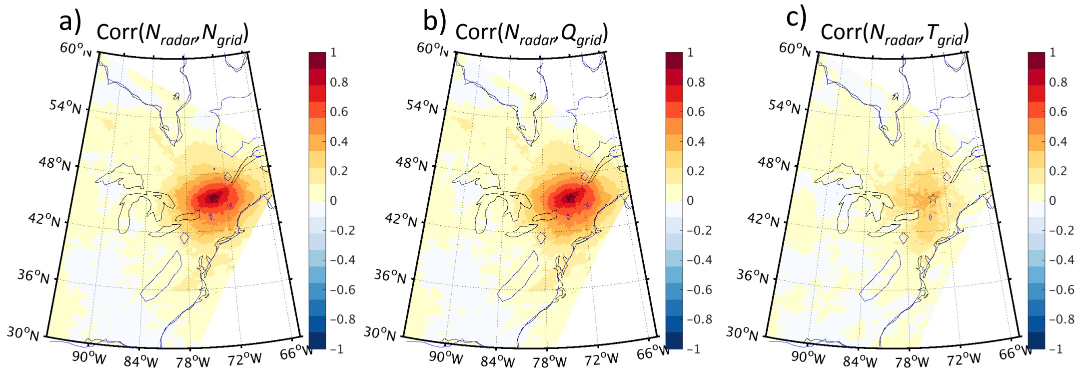

Figure 5.1 – Horizontal correlation of the error in refractivity over the McGill Radar site and that of a) refractivity, b) specific humidity and c) temperature.

background error correlations of refractivity from the McGill radar location and state variables over the whole spatial grid are also examined. The correlation pattern of refractivity and specific humidity (Fig. 5.1b) shows a pattern similar to the autocorrelation of the refractivity field. In contrast, the correlation has much smaller magnitude for the temperature fields (Fig. 5.1c). This can be explained from the fact that refractivity in summer in the surface layer depends much more on the specific humidity variations than on temperature variations.

Would the impact of assimilating refractivity from the operational radar network be the same throughout the large domain? We performed a simple examination of the autocorrelations corresponding to various geographic conditions and for two different forecasting times at 00 and 12 UTC. Fig. 5.2 shows the correlation of the background error in refractivity with that at the center of each subdomain. The correlation length is generally shorter and anisotropic in complex topography but is longer over the Midwest plains and ocean areas. With the shorter background error correlation length, a higher density of observations is needed to reduce the forecasting uncertainties. Furthermore, the error correlation length also shows diurnal variations.

This preliminary result suggests that assimilating near-surface refractivity in larger-scale regional models could have a significant value for some areas with longer correlation length of the background errors. Nevertheless, model background error statistics depend on the numerical model, the evolving atmospheric states and stages of the storms. A

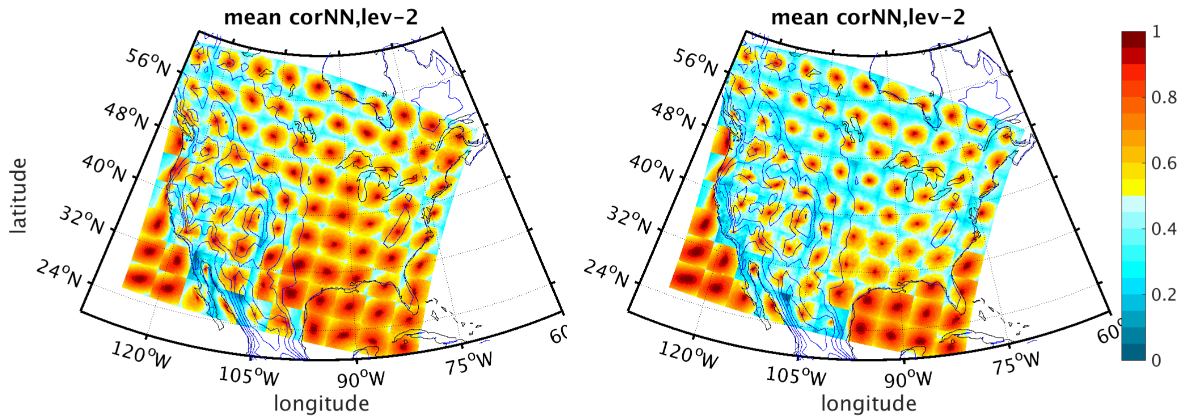

Figure 5.2 – Autocorrelation of refractivity at the second level of the model for two times: 00 UTC on the left panel and 12 UTC on the right. Each small grid is 4 degrees of latitude and longitude.

more detailed analysis of model background error is thus required. For example, more ensembles are needed to ensure the reliability and accuracy of the correlations (Stuart and Ord, 1986). In addition, the final increment of the analysis field also depends on the innovation term. Further works on evaluating the impact of assimilating the refractivity data from the radar network on the thermodynamic fields and forecasting through an assimilation system are strongly encouraged.

5.1.2 Land-surface and atmosphere interaction over heterogeneous surface

In the Montreal metropolitan area, under clear weather conditions, the downtown air is warmer and drier than that of the surrounding suburban and rural areas. A lower refractivity value is then expected at an urban (McTavish) surface weather station than at a suburban location (Montreal airport) during clear summer days (Fig. 5.3). The refractivity differences between urban and rural areas could be used to characterize the effect of urban heat islands.

Figure 5.3 shows the refractivity obtained from the radar estimates and surface observation at the McTavish and Montreal airport stations. The radar-estimated refractivity

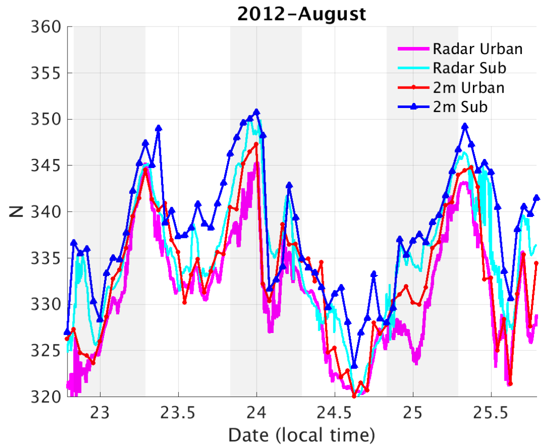

Figure 5.3 – Three days of refractivity observed from surface stations and radar refractivity in the urban (McTavish) and suburban (Montreal airport) areas. The data is collected from Aug 23 to 26, 2012.

has consistent trends with it observed from the surface stations. Differences in refractivity between the radar and the surface station can be explained by the different representative height of the data and the varying refractivity profiles. The operational surface station is located at 2 m above the ground level while the radar-estimated refractivity depending on the ground target is at 10-20 m height, as mentioned in Chapter 2.

The three-days average radar refractivity field (Fig. 5.4a) presents the horizontal low-level thermodynamic contrast distribution between the urban and suburban areas. The average refractivity pattern is correlated with the climatological summer volumetric soil moisture pattern (Fig. 5.4b). The local variation of water vapor at low levels is affected both by horizontal moisture advection and by evaporation from the land surface. The lower refractivity field in downtown might be caused by the less evaporation associated with drier soil moisture and more impervious surface in urban land areas.

This preliminary result indicates the potential meteorological value of radar refractivity for studying the near-surface thermodynamic conditions associated with heterogeneous land surface. Characterizing the spatial distribution of refractivity patterns will enhance our understanding of the diurnal, seasonal and even annual evolution of the horizontal thermodynamic distribution above different land uses. Radar refractvitiy fields will provide an evolving two-dimensional field to bridge the data gap between limited point

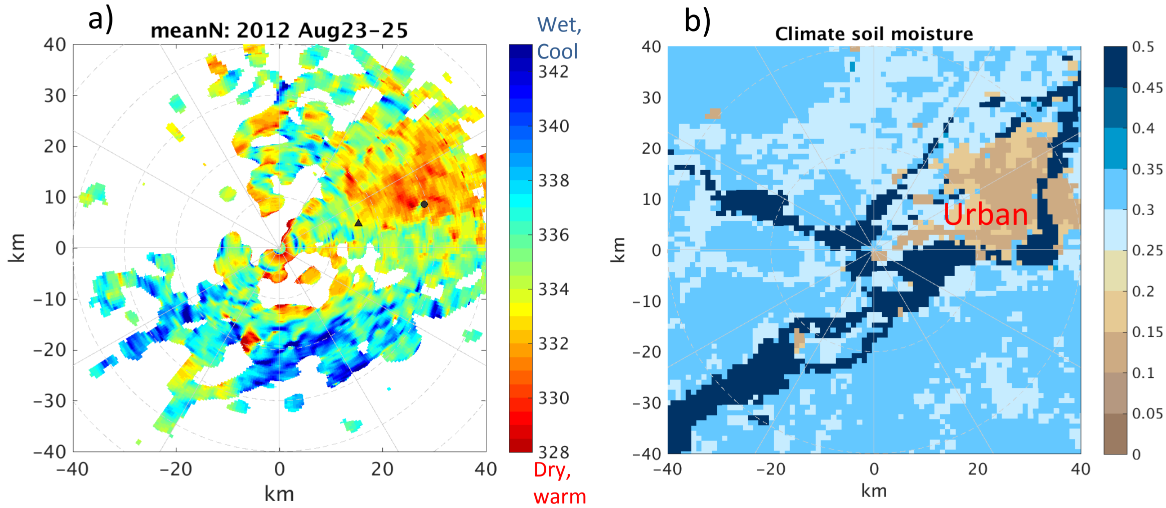

Figure 5.4 – (a) Three clear days (Aug 23 to 26, 2012) average radar-derived refractivity field in Montreal area. (b) Climatology summer volumetric soil moisture (m^3m^{-3}) from U.S. Geological Survey land-use database; the data were provided by Prof. Daniel Kirshbaum. Note that the wind speeds of the surface stations are less than 10 m s^{-1}, with temperature and humidity increasing as a low pressure system is approaching while a high pressure system moving offshore.

observation in previous studies. In addition, the elevated refractivity observations ($\sim$ 10 m above ground level) are better suited for NWP model evaluation than the surface observations (at 2 m) as they are more representative of the thermodynamic properties of the air at the lowest few levels of NWP models. Thus, radar-estimated refractivity represents a valuable dataset for NWP model evaluation, and for studying the sensitivity to model initialization and land-surface parameterizations, such as the high-resolution urban GEM-SRUF model (Leroyer et al., 2011; Milbrandt et al., 2016).

5.2 Gaining more information from ultimately recycling of ground targets

For most radar meteorologists, ground clutter has been mostly considered as an annoyance that contaminates the radar data at low elevation antenna scans. Methods of ground clutter identification and mitigation have been improved to obtain cleaner data (Hubbert et al., 2010a,b). However, for some given ground targets, the ground echoes contain implicitly useful information for radar meteorology. Zawadzki et al. (1983) summarized some early works using isolated communication towers for data quality check in four aspects: determining antenna power beam patterns (Rinehart and Frush, 1983), monitoring and calibrating the receiver stability (Rinehart and Garvey, 1978; Rinehart, 1978), and determining the antenna pointing and range errors (Rinehart and Tuttle, 1981, 1982). These methods are still applied in radars nowadays for monitoring the data quality, such as the German operational radar network and at McGill. Fabry et al. (1997) further extracted the near-surface horizontal thermodynamic distribution, the refractivity of the air, from the phase changes of ground targets. Park and Fabry (2011) attempted to determine the propagation condition through the coverage of ground echoes. In Chapter 2, we estimated the vertical refractivity gradient by the power difference between two elevations from given point-like ground targets. Besides for refractivity estimation, the propagation condition is critical to the quantitative precipitation estimation, ground clutter blockage detection, and the height representativeness of the radar data at far range. In addition, in Chapter 3, we studied the phase pattern of a parabolic antenna from scanning a tower as well as a microwave source with high-resolution scans at successive elevations. The ground clutter mitigation method can be further improved from better knowledge of the antenna phase pattern. For narrow meteorological targets comparable with the radar beam width, the antenna phase pattern will introduce biases in the radial velocity. Who knows what the ground targets will teach us next time?

Bibliography

Besson, L., C. Boudjabi, O. Caumont, and J. Parent du Chatelet, 2012: Links between weather phenomena and characteristics of refractivity measured by precipitation radar. *Bound.-Layer Meteor.*, **143 (1)**, 77–95, doi:10.1007/s10546-011-9656-7.

Besson, L. and J. Parent du Châtelet, 2013: Solutions for improving the radar refractivity measurement by taking operational constraints into account. *J. Atmos. Oceanic Technol.*, **30 (8)**, 1730–1742, doi:10.1175/JTECH-D-12-00167.1.

Besson, L., et al., 2016: Comparison of real-time refractivity measurements by radar with automatic weather stations, AROME-WMED and WRF forecast simulations during SOP1 of the HyMeX campaign. *Q.J.R. Meteorol. Soc.*, **142**, 138–152, doi:10.1002/qj.2799.

Bodine, D., P. L. Heinselman, B. L. Cheong, R. D. Palmer, and D. Michaud, 2010: A case study on the impact of moisture variability on convection initiation using radar refractivity retrievals. *J. Appl. Meteor. Climatol.*, **49 (8)**, 1766–1778, doi:10.1175/2010JAMC2360.1.

Bodine, D., et al., 2011: Understanding radar refractivity: Sources of uncertainty. *J. Appl. Meteor. Climatol.*, **50 (12)**, 2543–2560, doi:10.1175/2011JAMC2648.1.

Buban, M. S., C. L. Ziegler, E. N. Rasmussen, and Y. P. Richardson, 2007: The dryline on 22 May 2002 during IHOP: Ground-radar and in situ data analyses of the dryline and boundary layer evolution. *Mon. Wea. Rev.*, **135 (7)**, 2473–2505, doi:10.1175/MWR3453.1.

Carbone, R., et al., 2012: Thermodynamic profiling technologies workshop report to the national science foundation and the national weather service. Tech. rep., NCAR Technical Note NCAR/TN-488+STR, 80 pp.

Caumont, O., A. Foray, L. Besson, and J. Parent du Châtelet, 2013: An observation operator for radar refractivity change: Comparison of observations and convective-scale simulations. *Bound.-Layer Meteor.*, **148 (2)**, 379–397, doi:10.1007/s10546-013-9820-3.

Chandrasekar, V. and R. J. Keeler, 1993: Antenna pattern analysis and measurements for multiparameter radars. *J. Atmos. Oceanic Technol.*, **10 (5)**, 674–683, doi:10.1175/1520-0426(1993)010<0674:APAAMF>2.0.CO;2.

Chen, F., et al., 2007: Description and evaluation of the characteristics of the NCAR high-resolution land data assimilation system. *J. Appl. Meteor. Climatol.*, **46 (6)**, 694–713, doi:10.1175/JAM2463.1.

Crook, N. A., 1996: Sensitivity of moist convection forced by boundary layer processes to low-level thermodynamic fields. *Mon. Wea. Rev.*, **124 (8)**, 1767–1785, doi:0.1175/1520-0493(1996)124<1767:SOMCFB>2.0.CO;2.

Dabberdt, W. F. and T. W. Schlatter, 1996: Research opportunities from emerging atmospheric observing and modeling capabilities. *Bull. Amer. Meteor. Soc.*, **77 (2)**, 305–323, doi:10.1175/1520-0477(1996)077<0305:ROFEAO>2.0.CO;2.

Daley, R., 1991: *Atmospheric Data Analysis.* Cambridge University Press, 471 pp.

Desroziers, G., L. Berre, B. Chapnik, and P. Poli, 2005: Diagnosis of observation, background and analysis-error statistics in observation space. *Q.J.R. Meteorol. Soc.*, **131 (613)**, 3385–3396, doi:10.1256/qj.05.108.

Done, J. M., G. C. Craig, S. L. Gray, and P. A. Clark, 2012: Case-to-case variability of predictability of deep convection in a mesoscale model. *Q. J. R. Meteorol. Soc.*, **138 (664)**, 638–648, doi:10.1002/qj.943.

Doviak, R. J. and D. S. Zrnic, 1993: *Doppler Radar and Weather Observations.* 2d ed., Dover Publications, San Diego, 562 pp., doi:10.1016/B978-0-12-221422-6.50007-3.

Emanuel, K., et al., 1995: Report of the first prospectus development team of the U.S. weather research program to NOAA and the NSF. *Bull. Amer. Meteor. Soc.*, **76**, 1194–1208.

Fabry, F., 2004: Meteorological value of ground target measurements by radar. *J. Atmos. Oceanic Technol.*, **21 (4)**, 560–573, doi:10.1175/1520-0426(2004)021<0560:MVOGTM>2.0.CO;2.

Fabry, F., 2006: The spatial variability of moisture in the boundary layer and its effect on convection initiation: Project-long characterization. *Mon. Wea. Rev.*, **134 (1)**, 79–91, doi:10.1175/MWR3055.1.

Fabry, F. and C. Creese, 1999: If fine lines fail, try ground targets. *29th Int. Conf. on Radar Meteorology*, Montreal, QC, Canada, Amer. Meteor. Soc., 21–23.

Fabry, F., C. Frush, I. Zawadzki, and A. Kilambi, 1997: On the extraction of near-surface index of refraction using radar phase measurements from ground targets. *J. Atmos. Oceanic Technol.*, **14 (4)**, 978–987, doi:10.1175/1520-0426(1997)014<0978:OTEONS>2.0.CO;2.

Fabry, F. and C. Pettet, 2002: A primer to the interpretation of refractivity imagery during IHOP 2002, IHOP 2002 Refractivity Manual. Tech. rep., `https://www.eol.ucar.edu/isf/projects/ihop_2002/spol/summary/info/IHOP_N_Manual.pdf`.

Fabry, F. and J. Sun, 2010: For how long should what data be assimilated for the mesoscale forecasting of convection and why? Part I: On the propagation of initial condition errors and their implications for data assimilation. *Mon. Wea. Rev.*, **138 (1)**, 242–255, doi:10.1175/2009MWR2883.1.

Feng, Y.-C. and F. Fabry, 2016: The imperfect phase pattern of real parabolic radar antenna and data quality. *J. Atmos. Oceanic Technol.*, **33 (12)**, 2655–2661, doi:10.1175/JTECH-D-16-0143.1.

Feng, Y.-C., F. Fabry, and T. M. Weckwerth, 2016: Improving radar refractivity retrieval by considering the change in the refractivity profile and the varying altitudes of ground targets. *J. Atmos. Oceanic Technol.*, **33 (5)**, 989–1004, doi:10.1175/JTECH-D-15-0224.1.

Fisher, M., 2003: Background error covariance modelling. *Seminar on Recent developments in data assimilation for atmosphere and ocean, 8-12 September 2003*, ECMWF, Shinfield Park, Reading, ECMWF, 45–64.

Friedrich, K., U. Germann, and P. Tabary, 2009: Influence of ground clutter contamination on polarimetric radar parameters. *J. Atmos. Oceanic Technol.*, **26 (2)**, 251–269, doi:10.1175/2008JTECHA1092.1.

Fritz, J. and V. Chandrasekar, 2009: Implementation and analysis of networked radar refractivity retrieval. *J. Atmos. Oceanic Technol.*, **26 (10)**, 2123–2135, doi:10.1175/2009JTECHA1182.1.

Gasperoni, N. A., M. Xue, R. D. Palmer, and J. Gao, 2013: Sensitivity of convective initiation prediction to near-surface moisture when assimilating radar refractivity: Impact tests using OSSEs. *J. Atmos. Oceanic Technol.*, **30 (10)**, 2281–2302, doi:10.1175/JTECH-D-12-00038.1.

Ha, S.-Y. and C. Snyder, 2014: Influence of surface observations in mesoscale data assimilation using an ensemble Kalman filter. *Mon. Wea. Rev.*, **142 (4)**, 1489–1508, doi:10.1175/MWR-D-13-00108.1.

Hanley, K. E., D. J. Kirshbaum, S. E. Belcher, N. M. Roberts, and G. Leoncini, 2011: Ensemble predictability of an isolated mountain thunderstorm in a high-resolution model. *Q. J. R. Meteorol. Soc.*, **137 (661)**, 2124–2137, doi:10.1002/qj.877.

Hao, Y., D. Goeckel, R. Janaswamy, and S. Frasier, 2006: Surface refractive index field estimation from multiple radars. *Radio Sci.*, **41 (3)**, RS3002, doi:10.1029/2005RS003288.

Heinselman, P. L., B. L. Cheong, R. D. Palmer, D. Bodine, and K. Hondl, 2009: Radar refractivity retrievals in Oklahoma: Insights into operational benefits and limitations. *Wea. Forecasting,*, **24 (5)**, 1345–1361, doi:10.1175/2009WAF2222256.1.

Hollingsworth, A. and P. Lonnberg, 1986: The statistical structure of short-range forecast errors as determined from radiosonde data. part I: The wind field. *Tellus A*, **38A (2)**, 111–136, doi:10.1111/j.1600-0870.1986.tb00460.x.

Hubbert, J. C., M. Dixon, S. M. Ellis, and G. Meymaris, 2009: Weather radar ground clutter. Part I: Identification, modeling, and simulation. *J. Atmos. Oceanic Technol.*, **26 (7)**, 1165–1180, doi:10.1175/2009JTECHA1159.1.

Hubbert, J. C., S. M. Ellis, M. Dixon, and G. Meymaris, 2010a: Modeling, error analysis, and evaluation of dual-polarization variables obtained from simultaneous horizontal and vertical polarization transmit radar. Part I: Modeling and antenna errors. *J. Atmos. Oceanic Technol.*, **27 (10)**, 1583–1598, doi:10.1175/2010JTECHA1336.1.

Hubbert, J. C., S. M. Ellis, M. Dixon, and G. Meymaris, 2010b: Modeling, error analysis, and evaluation of dual-polarization variables obtained from simultaneous horizontal and vertical polarization transmit radar. Part II: Experimental data. *J. Atmos. Oceanic Technol.*, **27 (10)**, 1599–1607, doi:10.1175/2010JTECHA1337.1.

Jacques, D., W. Chang, S.-J. Baek, T. Milewski, L. Fillion, K.-S. Chung, and H. Ritchie, 2017: Developing a convective-scale EnKF data assimilation system for the Canadian MEOPAR project. *Mon. Wea. Rev.*, **145 (4)**, 1473–1494, doi:10.1175/MWR-D-16-0135.1.

Kalnay, E., 2003: *Atmospheric Modeling, Data Assimilation and Predictability.* Cambridge University Press, 368 pp.

Keeler, R. and S. Ellis, 2000: Observational error covariance matrices for radar data assimilation. *Phys. Chem. Earth, Part B: Hydrol. Oceans Atmos*, **25 (10)**, 1277–1280, doi:http://dx.doi.org/10.1016/S1464-1909(00)00193-3.

Koch, S. E., W. Feltz, F. Fabry, M. Pagowski, B. Geerts, K. M. Bedka, D. O. Miller, and J. W. Wilson, 2008: Turbulent mixing processes in atmospheric bores and solitary waves deduced from profiling systems and numerical simulation. *Mon. Wea. Rev.*, **136 (4)**, 1373–1400, doi:10.1175/2007MWR2252.1.

Leroyer, S., S. Bélair, J. Mailhot, and I. B. Strachan, 2011: Microscale numerical prediction over Montreal with the Canadian external urban modeling system. *J. Appl. Meteor. Climatol.*, **50 (12)**, 2410–2428, doi:10.1175/JAMC-D-11-013.1.

Madaus, L. E. and G. J. Hakim, 2016: Observable surface anomalies preceding simulated isolated convective initiation. *Mon. Wea. Rev.*, **144 (6)**, 2265–2284, doi: 10.1175/MWR-D-15-0332.1.

Mardia, K. V., 1972: *Statistics of Directional Data.* Academic Press.

Milbrandt, J. A., S. Bélair, M. Faucher, M. Vallée, M. L. Carrera, and A. Glazer, 2016: The Pan-Canadian high resolution (2.5 km) deterministic prediction system. *Wea. Forecasting*, **31 (6)**, 1791–1816, doi:10.1175/WAF-D-16-0035.1.

Moisseev, D., R. Keränen, P. Puhakka, J. Salmivaara, and M. Leskinen, 2010: Analysis of dual-polarization antenna performance and its effect on QPE. *6th European Conference on Radar Meteorology*, Sibiu, Romania.

Montmerle, T., A. Caya, and I. Zawadzki, 2002: Short-term numerical forecasting of a shallow storms complex using bistatic and single-Doppler radar data. *Wea. Forecasting,*, **17 (6)**, 1211–1225, doi:10.1175/1520-0434(2002)017<1211:STNFOA>2.0.CO;2.

Mudukutore, A., V. Chandrasekar, and E. A. Mueller, 1995: The differential phase pattern of the CSU CHILL radar antenna. *J. Atmos. Oceanic Technol.*, **12 (5)**, 1120–1123, doi: 10.1175/1520-0426(1995)012<1120:TDPPOT>2.0.CO;2.

Myagkov, A., P. Seifert, U. Wandinger, M. Bauer-Pfundstein, and S. Y. Matrosov, 2015: Effects of antenna patterns on cloud radar polarimetric measurements. *J. Atmos. Oceanic Technol.*, **32 (10)**, 1813–1828, doi:10.1175/JTECH-D-15-0045.1.

Nicol, J. C. and A. J. Illingworth, 2012: The effect of phase-correlated returns and spatial smoothing on the accuracy of radar refractivity retrievals. *J. Atmos. Oceanic Technol.*, **30 (1)**, 22–39, doi:10.1175/JTECH-D-12-00077.1.

Nicol, J. C., A. J. Illingworth, and K. Bartholomew, 2014: The potential of 1 h refractivity changes from an operational C-band magnetron-based radar for numerical weather prediction validation and data assimilation. *Q. J. R. Meteorol. Soc.*, **140 (681)**, 1209–1218, doi:10.1002/qj.2223.

Nicol, J. C., A. J. Illingworth, T. Darlington, and M. Kitchen, 2013: Quantifying errors due to frequency changes and target location uncertainty for radar refractivity retrievals. *J. Atmos. Oceanic Technol.*, **30 (9)**, 2006–2024, doi:10.1175/JTECH-D-12-00118.1.

Parent du Chatelet, J., C. Boudjabi, L. Besson, and O. Caumont, 2012: Errors caused by long-term drifts of magnetron frequencies for refractivity measurement with a radar: Theoretical formulation and initial validation. *J. Atmos. Oceanic Technol.*, **29 (10)**, 1428–1434, doi:10.1175/JTECH-D-12-00070.1.

Park, S. and F. Fabry, 2010: Simulation and interpretation of the phase data used by the radar refractivity retrieval algorithm. *J. Atmos. Oceanic Technol.*, **27 (8)**, 1286–1301, doi:10.1175/2010JTECHA1393.1.

Park, S. and F. Fabry, 2011: Estimation of near-ground propagation conditions using radar ground echo coverage. *J. Atmos. Oceanic Technol.*, **28 (2)**, 165–180, doi:10.1175/2010JTECHA1500.1.

Parrish, D. F. and J. C. Derber, 1992: The national meteorological center's spectral statistical-interpolation analysis system. *Mon. Wea. Rev.*, **120 (8)**, 1747–1763, doi:10.1175/1520-0493(1992)120<1747:TNMCSS>2.0.CO;2.

Pielke, R. A., 2001: Influence of the spatial distribution of vegetation and soils on the prediction of cumulus convective rainfall. *Rev. Geophys.*, **39 (2)**, 151–177, doi:10.1029/1999RG000072.

Probert-Jones, J. R., 1962: The radar equation in meteorology. *Q. J. R. Meteorol. Soc.*, **88 (378)**, 485–495, doi:10.1002/qj.49708837810.

Rinehart, R. E., 1978: On the use of ground return targets for radar reflectivity factor calibration checks. *J. Appl. Meteor.*, **17 (9)**, 1342–1350, doi:10.1175/1520-0450(1978)017<1342:OTUOGR>2.0.CO;2.

Rinehart, R. E., 1991: Spurious velocities in Doppler radar data caused by a moving antenna feedhorn. *J. Atmos. Oceanic Technol.*, **8 (6)**, 733–745, doi:10.1175/1520-0426(1991)008<0733:SVIDRD>2.0.CO;2.

Rinehart, R. E. and C. L. Frush, 1983: Comparison of antenna beam patterns obtained from near-field test measurements and ground target scans comparison of antenna beam patterns obtained from near-field test measurements and ground target scans. *21st Conference on Radar Meteorology*, Edmonton, Alberta, Canada, 291–295.

Rinehart, R. E. and E. T. Garvey, 1978: Radar reflectivity calibration checks using ground targets. *18th Conference on Radar Meteorology*, Atlanta, Georgia, 266–270.

Rinehart, R. E. and J. D. Tuttle, 1981: A technique for determining antenna beam patterns using a ground target. *Preprints, 20th Conference on Radar Meteorology*, Amer. Meteor. Soc., Boston MA, 672–675.

Rinehart, R. E. and J. D. Tuttle, 1982: Antenna beam patterns and dual-wavelength processing. *J. Appl. Meteor.*, **21 (12)**, 1865–1880, doi:10.1175/1520-0450(1982)021<1865:ABPADW>2.0.CO;2.

Roberts, R. D., et al., 2008: REFRACTT 2006: Real-time retrieval of high-resolution, low-level moisture fields from operational NEXRAD and research radars. *Bull. Amer. Meteor. Soc.*, **89 (10)**, 1535–1548, doi:10.1175/2008BAMS2412.1.

Seko, H., E.-I. Sato, H. Yamauchi, and T. Tsuda, 2017: *Data Assimilation Experiments of Refractivity Observed by JMA Operational Radar*. Springer International Publishing, Cham, 327–336 pp., doi:10.1007/978-3-319-43415-5-14.

Sherwood, S. C., R. Roca, T. Weckwerth, and N. Andronova, 2010: Tropospheric water vapor, convection, and climate. *Rev. Geophys.*, **48 (2)**, doi:10.1029/2009RG000301.

Smith, E. and S. Weintraub, 1953: The constants in the equation for atmospheric refractive index at radio frequencies. *Proceedings of the IRE*, **41 (8)**, 1035–1037, doi:10.1109/JRPROC.1953.274297.

Späth, F., A. Behrendt, S. K. Muppa, S. Metzendorf, A. Riede, and V. Wulfmeyer, 2016: 3-D water vapor field in the atmospheric boundary layer observed with scanning differential absorption lidar. *Atmos. Meas. Tech.*, **9 (4)**, 1701–1720, doi:10.5194/amt-9-1701-2016.

Stuart, A. and K. Ord, 1986: *Kendall's Advanced Theory of Statistics.*, Vol. 1, Distribution Theory. 5th ed., Charles Griffin and Company Limited, 604 pp.

Sun, J., 2005: Convective-scale assimilation of radar data: progress and challenges. *Q. J. R. Meteorol. Soc.*, **131 (613)**, 3439–3463, doi:10.1256/qj.05.149.

Sun, J., et al., 2013: Use of NWP for nowcasting convective precipitation: Recent progress and challenges. *Bull. Amer. Meteor. Soc.*, **95 (3)**, 409–426, doi:10.1175/BAMS-D-11-00263.1.

Wakimoto, R. M. and H. V. Murphey, 2010: Frontal and radar refractivity analyses of the dryline on 11 June 2002 during IHOP. *Mon. Wea. Rev.*, **138 (1)**, 228–241, doi:10.1175/2009MWR2991.1.

Waller, J. A., D. Simonin, S. L. Dance, N. K. Nichols, and S. P. Ballard, 2016: Diagnosing observation error correlations for Doppler radar radial winds in the Met Office UKV model using observation-minus-background and observation-minus-analysis statistics. *Mon. Wea. Rev.*, **144 (10)**, 3533–3551, doi:10.1175/MWR-D-15-0340.1.

Weber, R. O., 1997: Estimators for the standard deviation of horizontal wind direction. *Journal of Applied Meteorology*, **36 (10)**, 1403–1415, doi:10.1175/1520-0450(1997)036<1403:EFTSDO>2.0.CO;2.

Weckwerth, T. M., 2000: The effect of small-scale moisture variability on thunderstorm initiation. *Mon. Wea. Rev.*, **128 (12)**, 4017–4030, doi:10.1175/1520-0493(2000)129<4017:TEOSSM>2.0.CO;2.

Weckwerth, T. M., L. J. Bennett, L. J. Miller, J. V. Baelen, P. D. Girolamo, A. M. Blyth, and T. J. Hertneky, 2014: An observational and modeling study of the processes leading to deep, moist convection in complex terrain. *Mon. Wea. Rev.*, **142 (8)**, 2687–2708, doi:10.1175/MWR-D-13-00216.1.

Weckwerth, T. M., T. W. Horst, and J. W. Wilson, 1999: An observational study of the evolution of horizontal convective rolls. *Mon. Wea. Rev.*, **127 (9)**, 2160–2179, doi:10.1175/1520-0493(1999)127<2160:AOSOTE>2.0.CO;2.

Weckwerth, T. M. and D. B. Parsons, 2006: A review of convection initiation and motivation for IHOP_2002. *Mon. Wea. Rev.*, **134 (1)**, 5–22, doi:10.1175/MWR3067.1.

Weckwerth, T. M., C. R. Pettet, F. Fabry, S. J. Park, M. A. LeMone, and J. W. Wilson, 2005: Radar refractivity retrieval: Validation and application to short-term forecasting. *J. Appl. Meteor.*, **44 (3)**, 285–300, doi:10.1175/JAM-2204.1.

Wilson, J. W., N. A. Crook, C. K. Mueller, J. Sun, and M. Dixon, 1998: Nowcasting thunderstorms: A status report. *Bull. Amer. Meteor. Soc.*, **79 (10)**, 2079–2099.

Wilson, J. W. and R. D. Roberts, 2006: Summary of convective storm initiation and evolution during IHOP: Observational and modeling perspective. *Mon. Wea. Rev.*, **134 (1)**, 23–47, doi:10.1175/MWR3069.1.

WMO, 2015: Statemetn of guidance for nowcasting and very short range forecasting (VSRF). Tech. rep., https://www.wmo.int/pages/prog/www/OSY/SOG/SoG-Nowcasting-VSRF.pdf.

Wulfmeyer, V., et al., 2015: A review of the remote sensing of lower tropospheric thermodynamic profiles and its indispensable role for the understanding and the simulation of water and energy cycles. *Rev. Geophys*, **53 (3)**, 819–895, doi:10.1002/2014RG000476.

Zawadzki, I., E. Torlaschi, and R. Sauvageau, 1981: The relationship between mesoscale thermodynamic variables and convective precipitation. *J. Atmos. Sci.*, **38 (8)**, 1535–1540, doi:10.1175/1520-0469(1981)038<1535:TRBMTV>2.0.CO;2.

Zawadzki, I., A. Waldvogel, R. Rinehart, and R. Ray, 1983: Gound detection radarmeteorology GDR. *21st Conference on Radar Meteorology*, Edmonton, Alberta, Canada, 186–191.